Time-of-Flight PET with SiPM sensors on monolithic scintillation crystals

Printed by: Gildeprint Drukkerijen B.V., Enschede

RIJKSUNIVERSITEIT GRONINGEN

Time-of-Flight PET with SiPM sensors on monolithic scintillation crystals

Proefschrift

ter verkrijging van het doctoraat in de
Wiskunde en Natuurwetenschappen
aan de Rijksuniversiteit Groningen
op gezag van de
Rector Magnificus, dr. F. Zwarts,
in het openbaar te verdedigen op
vrijdag 28 januari 2011
om 13.15 uur

door

Ruud Vinke

geboren op 20 maart 1981
te Lichtenvoorde

Promotor:	Prof. dr. H. Löhner
Copromotor:	Dr. P. Dendooven
Beoordelingscommissie:	Prof. dr. C.W.E. van Eijk Prof. dr. W. Enghardt Prof. dr. A.M.J. Paans

ISBN (printed version): 978-90-367-4737-0

ISBN (electronic version): 978-90-367-4738-7

Contents

1 Introduction

Nuclear medicine is the branch of medicine that uses radioactive substances in the diagnosis and treatment of disease. These radioactive substances consist of a radionuclide (tracer), chemically bound to a biologically active molecule. Once administered to the patient, the molecule concentrates at specific organs or cellular receptors with a certain biological function. This allows nuclear medicine to image the location and extent of a disease process in the body, based on the cellular and physiologic function. The ability to visualize physiological function separates nuclear medicine imaging techniques from traditional anatomic imaging techniques, such as Computed Tomography (CT). Nuclear medicine imaging techniques include scintigraphy, Single Photon Emission Computed Tomography (SPECT) and Positron Emission Tomography (PET). Of these techniques, PET has the highest sensitivity [1, 2] and is the diagnostic imaging technique of choice for many diseases. It is used predominantly in determining the presence and severity of cancers, neurological disorders and cardio-vascular diseases (CVD). When combined with anatomic imaging, such as CT, PET provides the best available information on tumor extent for many common cancers [3]. It is considered essential in the management of many human cancers [4]. The role of PET in cancer diagnosis includes the initial staging, early and late assessment of the therapeutic response, follow-up and diagnosis of recurrence. PET is further increasingly being used in radiotherapy planning and follow-up and in drug development in pre-clinical trials in pharmacology. Finally, it is expected that PET will play a key role in the clinical translation of novel concepts of molecular medicine, such as in cardiology for monitoring of new therapies and identification of individuals at elevated risk for development of heart failure or arrhythmia/sudden death [5].

For efficient therapy, it is essential that cancer is diagnosed at the earliest possible stage, thereby increasing the chance of patient recovery. The ability of the physician to diagnose disease at an early stage depends crucially on the quality and accuracy of the PET image. The image quality is primarily determined by the PET detector performance. Significant advances in PET detector performance have recently been possible due to the introduction of fast and bright inorganic scintillators for radiation detection (LYSO and $LaBr_3$:Ce); the development of compact, fast and high-gain solid-state photosensors for detecting the scintillation light (silicon photomultipliers, SiPMs) and the ever-increasing computing power at affordable cost, allowing advanced signal processing in reasonable time.

PET detectors require high detection efficiency, high count rate performance and high spatial, energy and timing resolution. If the detection of a 511 keV gamma photon can be timed with an accuracy well below 1 ns, time-of-flight (TOF) infor-

mation (the difference of the arrival times of two 511 keV gamma photons from the annihilation process) can be used during image reconstruction (a technique called TOF-PET) to significantly increase the image quality in terms of signal-to-noise ratio (SNR) [6–8]. In addition, it is desirable that the full 3D position-of-interaction of the impinging 511 keV gamma photon is reconstructed, thus including information about the *depth-of-interaction* (DOI) of the gamma photon in the PET detector. This should all be achieved, while maintaining affordable detector costs. Unfortunately, these performance parameters often impose conflicting design requirements. For example, when increasing the detection efficiency by selecting a larger sensitive detector volume, the spatial resolution will generally deteriorate due to increased scattering of the gamma photons inside the detector material. When optimizing the detector performance, this necessarily means that a trade-off has to be made between the different performance parameters. This is especially true for the requirement of affordable detector costs.

This work concentrates on the use of large continuous (*monolithic*) scintillation crystals coupled to fast photosensor arrays for TOF-PET. For optimal spatial, energy and timing resolution, we use bright and fast scintillation crystals, namely LYSO and $LaBr_3$:Ce. As photosensor arrays, a fast multianode PMT (MAPMT) and a SiPM array are used. SiPMs are a new interesting class of semiconductor photosensors that have a high gain (similar to PMTs) and are very fast. Compared to PMTs, these devices are much more compact and essentially transparent to 511 keV gamma rays, allowing flexible readout geometries. Furthermore, they are compatible with magnetic fields, which makes them possible candidates for PET-MRI integrated systems.

Chapter 2 describes system aspects of PET and explains the requirements on the detectors, mentioned above. Chapter 3 gives a detailed overview of PET detector components and introduces the aforementioned monolithic scintillation detector concept. In chapter 4, a statistical estimation method is presented to determine the 3D position-of-interaction of gamma photons inside a monolithic scintillation crystal coupled to a MAPMT. In addition, a method to calibrate and correct for the arrival time variation with the position-of-interaction is introduced. In chapter 5, the position estimation method of chapter 4 is used on thick (efficient) crystals coupled to a MAPMT. The positioning performance is tested for varying crystal thickness and at various excitation depths. The timing performance of small 1×1 mm^2 SiPM sensors is characterized in chapter 6, using a picosecond laser pulser. The timing performance of 3×3 mm^2 SiPM sensors coupled to fast $LaBr_3$:Ce crystals is presented in chapter 7. Chapter 8 contains positioning and timing results of a monolithic $LaBr_3$:Ce crystal coupled to a SiPM array.

2 Nuclear Medicine Imaging Modalities

As mentioned in chapter 1, radionuclides are used in nuclear medicine to image and localize disease processes. Techniques of diagnostic nuclear medicine include scintigraphy, Single Photon Emission Computed Tomography (SPECT) and Positron Emission Tomography (PET). In scintigraphy, 2D images are generated from the tracer (radionuclide) distribution in the body. In contrast, SPECT and PET generate 3D images of the tracer distribution. SPECT and PET are the major imaging modalities in nuclear medicine.

2.1 Single Photon Emission Computed Tomography (SPECT)

SPECT is based on the detection of gamma-ray emitting radionuclides. Gamma cameras acquire 2D (planar) projection images of the tracer distribution from multiple angles. A 3D image is generated from these planar images using a tomographic reconstruction algorithm. The gamma camera contains collimators to reject gamma photons that are not within a small angular range. This is required, because otherwise the angle of incidence would not be known and projections from several angles would overlap at the gamma camera. The most often used radionuclide for SPECT is technetium-99m (^{99m}Tc), which emits gamma-rays of 140.5 keV energy. Besides ^{99m}Tc, a wide variety of radionuclides are used with a gamma-ray energy range between about 100 and 500 keV.

2.2 Positron Emission Tomography (PET)

PET is an imaging technique that is based on the decay of a positron (β^+) emitting radionuclide, chemically bound to a biologically active molecule (see Fig. 2.1). After its release, the positron quickly annihilates with an electron and, preferentially, two 511 keV gamma photons are produced in nearly opposite directions[1]. The pair of gamma photons is detected in coincidence by radiation detectors in a cylindrical configuration (see Fig. 2.2). This coincident detection defines a line, the *line of response* (LOR), along which the annihilation took place. From many

[1] It is also possible that three or more gamma photons are created, but the probability becomes lower with each additional photon. The ratio of annihilation into three photons vs. annihilation into two photons is predicted to be about 1/378 [9].

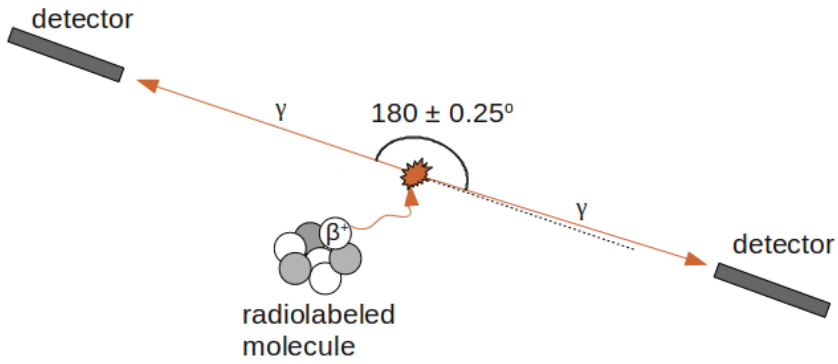

Figure 2.1: Positron emission and annihilation. Two 511 keV gamma (γ) photons are generated in nearly opposite directions and detected in coincidence.

LORs, a map of the concentration of the radionuclides can be generated using a tomographic reconstruction algorithm.

Since the direction of both gamma photons is known from the LOR, there is no need to use a mechanical collimator to define (and thus restrict) the acceptance angle, as in SPECT. The acceptance angle in PET is thus wider and this translates into a sensitivity for PET that is two to three orders of magnitude higher than for SPECT [2].

2.2.1 Spatial resolution

The obtainable spatial resolution is limited by the physics of positron emission and annihilation.

After the radionuclide decays and emits a positron, the positron loses its energy by multiple collisions with surrounding molecules. Annihilation preferentially occurs after thermalization with the environment[2]. This means that the positron travels some distance (the *positron range*) before the gamma photons are produced. The position uncertainty arising from this process limits the obtainable spatial resolution. The resulting blurring of the tomographic picture due to the positron range strongly depends on the energy distribution of the positron and, thus, on the radionuclides used. Fig. 2.3 shows positron range profiles for two common radionuclides (^{18}F and ^{15}O). The FWHM resolutions are 0.10 mm and 0.50 mm for ^{18}F and ^{15}O, respectively. However, the profiles can not be described by Gaussians since they have long exponential tails, giving FWTM resolutions of

[2]Although positron annihilation in-flight can reach a substantial fraction of up to about 20 % of fully absorbed positrons [11].

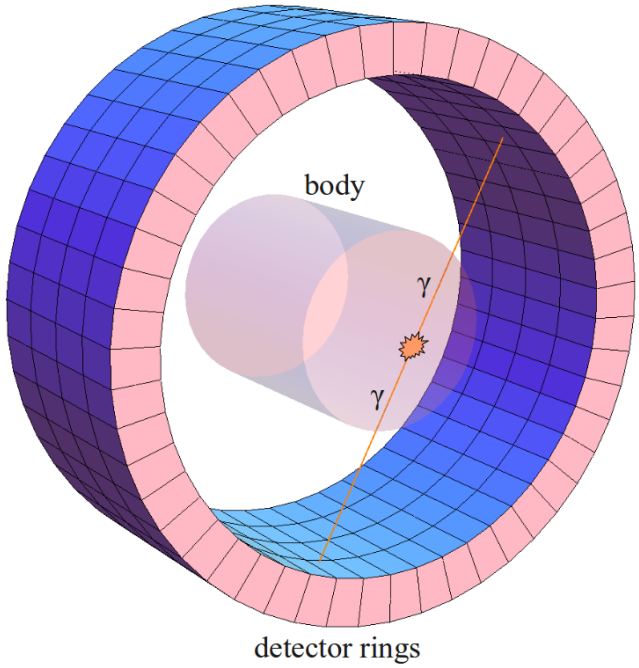

Figure 2.2: Schematic view of a PET scanner, consisting of rings of radiation detectors. The coincident detection of the produced gamma photons defines a line, the line of response (LOR), along which the annihilation took place.

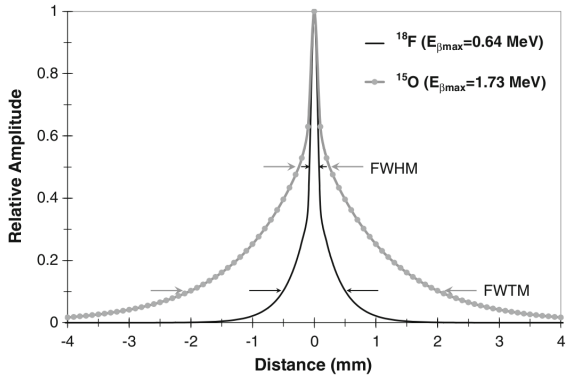

Figure 2.3: Positron range profiles for ^{18}F and ^{15}O in water. From [10].

1.0 mm and 4.1 mm for ^{18}F and ^{15}O, respectively.

Another limiting effect is called the *acollinearity*. After thermalization, both

the annihilating positron and electron have a residual momentum. Due to momentum conservation, the emission angle between the two emitted 511 keV gamma photons is not exactly 180° in the detector frame[3]. The angular distribution is approximately Gaussian with a FWHM of ∼0.5° [12]. The effect on the FWHM spatial resolution R_{acol} depends on the separation D of the coincidence detectors:

$$R_{acol} = 0.5 \cdot D \cdot \tan(0.25°) = 0.0022 \cdot D \tag{2.1}$$

For a whole-body PET scanner the ring diameter is typically 80 cm, corresponding to an R_{acol} of 1.8 mm FWHM at the geometric center of the ring.

Apart from the positron range and acollinearity effect, the spatial resolution further depends on the detector resolution R_{det}, but in a non-trivial way[4]. If not corrected for, the parallax effect degrades the spatial resolution in the radial direction (see section 2.2.3). In the tomographic reconstruction algorithm, spatial filters are often used to suppress noise. These filters further lead to some degradation of the spatial resolution, as the high-frequency information is removed.

2.2.2 Sensitivity

Sensitivity is quantified as the number of detected events per unit of activity in the examined object. Sensitivity is considered as the most important system parameter, since it determines the image quality per unit scan time [13]. Today, human whole-body PET is limited by sensitivity, rather than spatial resolution. Clinical systems often have, on purpose, a reconstructed spatial resolution that is worse than the spatial resolution potential of the system, to achieve sufficient acquired counts per image pixel[5]. This keeps the statistical fluctuations in the number of counts per image pixel low, and thus provides an image signal-to-noise ratio (SNR) acceptable for diagnostic interpretation. Breakthroughs in whole-body imaging will require significant increases in system sensitivity [14].

As discussed before, due to the larger acceptance angle, the sensitivity for PET is two to three orders of magnitude higher than for SPECT. The higher gamma photon energy of 511 keV (as compared to a typical gamma energy of 140 keV for SPECT) results in a higher penetrating power into material. This means that a higher fraction of gamma photons escapes the examined body, but also that (thick) detectors with high stopping power are needed to efficiently detect the incident

[3] Obviously, in the center-of-mass frame this angle is exactly 180°.

[4] The position response profile of both coincidence detectors has to be projected and convoluted on the plane centered at the annihilation event. The spatial resolution varies by about 40 % in the space between the detectors, with a maximum value of R_{det} at the face of either detector, see [12] for the mathematics.

[5] If the spatial resolution is improved by a factor of 2, the total number of counts needs to be increased by a factor of $2^3 = 8$ (for 3D-mode PET) to keep the number of counts per image pixel the same.

radiation. The sensitivity is primarily determined by detector efficiency ϵ (fraction of incident photons that are detected) and fraction of the solid angle 4π covered by the detectors (the geometric efficiency, g). The true coincidence event rate[6] f_{true} for a positron-emitting source located in a homogeneous absorbing medium between a pair of coincidence detectors is given by [12]:

$$f_{true} = E\epsilon^2 g e^{-\mu_o T_o} \tag{2.2}$$

where E is the source emission rate (positrons/s), μ_o the linear attenuation coefficient of the object and T_o the thickness of the object. The detector efficiency contribution ϵ is squared, since both gamma photons need to be detected in coincidence. ϵ is determined by the linear attenuation coefficient of the detector material μ_d and the thickness of the detector T_d. For a point source located on the central axis of the detector, it is given by:

$$\epsilon = 1 - e^{-\mu_d T_d} \tag{2.3}$$

For high sensitivity, thick detectors with large attenuation coefficients that cover a considerable fraction of the solid angle 4π, are thus required. The attenuation coefficient is commonly parametrized as the attenuation length $1/\mu_d$. Values for the attenuation lengths for different inorganic scintillation materials are given in Table 3.1.

2.2.3 Image degrading factors

As discussed in section 2.2.1, the physics of positron emission and annihilation principally limits the obtainable spatial resolution in PET. This section discusses additional degrading factors for PET that can limit the obtainable spatial resolution and the signal-to-noise ratio (SNR), but for these effects (partial) correction or reduction techniques can be applied.

Parallax effect

Parallax is the apparent difference in observed position of an object, viewed from different lines of sight (Fig. 2.4). In PET imaging, this effect shows up whenever a gamma ray enters the detector from an oblique angle, while the detector does not give information about the depth-of-interaction (DOI) of the gamma ray in the detector. The absence of information about the DOI leads to a parallax error in the determination of the position in the other spatial directions. The apparent width of the detector elements is wider at the edges of the transaxial field-of-view

[6] *True* coincidence events arise from gamma photons that originate from the same annihilation event and did not undergo Compton scattering within the examined body, as opposed to scattered and random coincidences (see Fig. 2.6 and section 2.2.3).

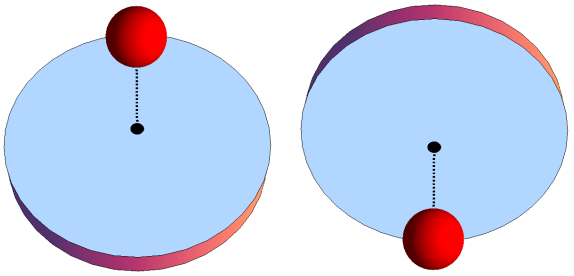

(a) Perspective 1 (b) Perspective 2

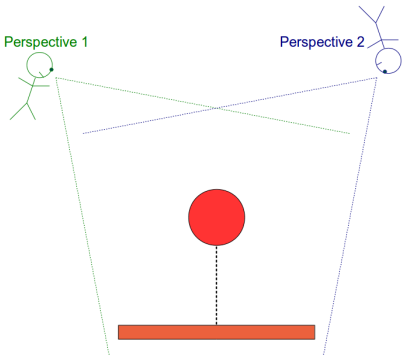

(c) Overview of 3D scene and location of observers. The view of the observers is shown in (a) and (b).

Figure 2.4: Illustration of the parallax effect. 3D scene viewed from two different perspectives. The observed (2D) position of the sphere is different for both views, since sight involves planar (2D) projections of objects located in 3D space. The sphere is actually located on the surface normal extending from the center of the background plane, indicated by the black dashed line in (a) and (b). Knowledge about the height of the sphere above the plane would allow to derive the true position of the sphere from the 2D image.

(FOV), compared to the center of the FOV (see Fig. 2.5). This effect thus causes a position blurring at the edges of the FOV. At the axis of the detector ring (i.e. center of the transaxial FOV) there is no parallax effect, since the gamma rays enter the detectors with perpendicular incidence on the detector front surface. The parallax effect is one of the most important degrading factors in PET. Commercial PET scanners often have detector arrays arranged on rings of larger diameter than would be necessary to fit the patient, even though this significantly increases

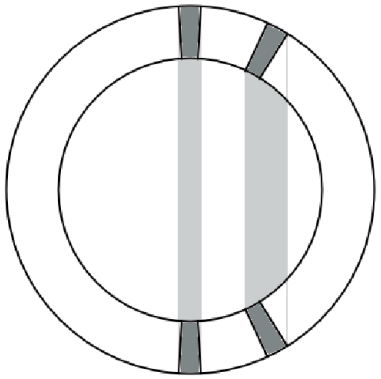

Figure 2.5: Transaxial view of one ring of a PET scanner. The apparent width of the detector elements (indicated by the shaded areas) increases towards the edges of the FOV. If the detector is not able to give DOI information, this effect introduces position blurring.

the detector costs (because more detectors are needed) and reduces the system sensitivity (since there is less solid angle coverage). For a typical whole-body PET scanner with 4 mm wide detector elements and 80 cm ring diameter, the spatial resolution is degraded by 40 % at 10 cm distance from the center of the FOV [12].

The effect can be corrected for by detecting the full 3D interaction position (thus including DOI) inside the detector element. This allows for detector rings with a diameter comparable to the transaxial FOV, thereby reducing detector costs, increasing the system sensitivity and reducing the position blurring associated with the acollinearity (Eq. 2.1). Enabling DOI detection in PET detectors has been one of the most active fields of research in PET imaging.

Recently, an alternative procedure has been developed to address the parallax effect. By empirically measuring the spatially variant system response, or 'global' *point spread function* (PSF), and use the PSF during the image reconstruction, improved and near-uniform spatial resolution can be achieved throughout the FOV [15]. This approach requires the knowledge of the PSF in each point of the FOV, which can be obtained by moving an uncollimated point source throughout the FOV. This feature has already been included in a commercial whole-body PET scanner (Siemens Biograph TruePoint PET/CT [16]). Impressive results can be achieved, although it is mentioned in [17] that the PSF-enabled reconstruction also leads to nonuniform noise correlations and that the system modelling affects the required computing power needed. The best procedure to correct for the parallax effect is to use DOI-enabled detectors in combination with a PSF model during the reconstruction (after the DOI information has been included) [17].

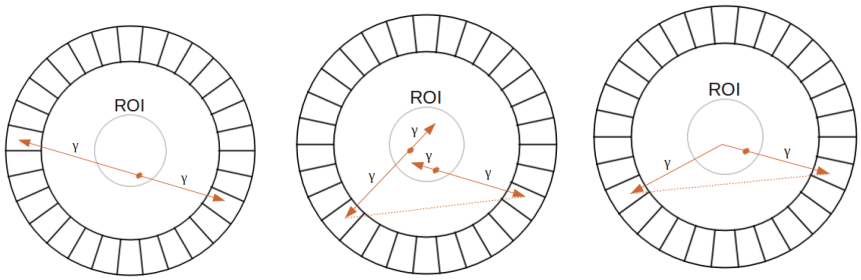

(a) True coincidence (b) Random coincidence (c) Scattered coincidence

Figure 2.6: Types of coincidence events for PET. For random and scattered events, LORs can be assigned outside the region of the emission source (indicated by the region-of-interest, ROI).

Section 3.3.3 gives an overview of some proposed scintillation detector designs with DOI detection capability. In the current work, a 3D position reconstruction algorithm for continuous scintillation crystals has been developed and is presented in chapter 4.

Random coincidences and Compton scattering

Of the various ways gamma photons of 511 keV interact with matter, only two interaction mechanisms have any real significance for gamma photon detection: photoelectric absorption and Compton scattering [18]. These interactions produce detectable electrical signals at the detector level, as discussed in detail in chapter 3. A considerable fraction of the emitted gamma photons also interacts within the examined body. At 511 keV, the attenuation length $1/\mu_o$ is about 10.5 cm in human tissue [19]. The absorption of gamma photons within the examined body leads to a reduction of the coincidence event rate (Eq. 2.2), and in addition to a larger amount of *random coincidences*. Since for coincidence detection two gamma photons need to be detected within a predefined time window, random coincidences can occur when two annihilation events occur right after each other, and for both events only one gamma photon is detected. The system has no means to recognize that the detected gamma photons came from different annihilation events, and an LOR is incorrectly assigned, see Fig. 2.6(b). The random coincidence event rate f_{random} can be determined from the singles event rates of detectors a and b from the coincident detector pair ($f_{singles,a}$ and $f_{singles,b}$).

$$f_{random} = 2\tau \cdot f_{singles,a} \cdot f_{singles,b} \tag{2.4}$$

where 2τ is the predefined time window for coincidence events. The random event rate can thus be reduced by employing a small coincidence time window. This requires fast detectors with a good timing resolution. This degrading factor does not exist for SPECT, since it is based on singles detection.

Compton scattering is the inelastic scattering of gamma photons (or X-rays) with weakly bound atomic and molecular electrons in matter. When one or both of the detected gamma photons of an annihilation pair underwent Compton scattering within the examined body, the information about the origin of the positron emission is lost and the LOR is incorrectly assigned, see Fig. 2.6(c). Since a considerable fraction of the energy of the gamma photon is absorbed during Compton scattering (see Fig. 3.7(b)), these events can partly be filtered out by detecting the energy of the impinging gamma photons at the detector and applying energy thresholding. This requires radiation detectors with a good energy resolution. For standard energy windows, the fraction of Compton scattered events approaches 50 % of the total detected events [20].

The mis-positioned LORs from scattered and random events are distributed uniformly across the FOV and are effectively manifested as background noise in the reconstructed image, reducing the image contrast. The image SNR is affected by the sensitivity to true coincidence events (Eq. 2.2) and the background contributions from scattered and random events. In PET, the *noise equivalent count rate* (NEC) parameter is commonly used to compare the tomograph performance [21]:

$$NEC = \frac{f_{true}^2}{f_{true} + f_{random} + f_{scatter}} \tag{2.5}$$

where $f_{scatter}$ is the scatter coincidence event rate; the true coincidence event rate f_{true} and the random coincidence event rate f_{random} are introduced in Eqs. 2.2 and 2.4, respectively. NEC can be seen as the reduced true coincidence event rate that without random and scatter components ($f_{random} = f_{scatter} = 0$), produces the same image SNR as the true coincidence event rate obtained by subtracting the random and scatter coincidence event rates from the total coincidence event rate ($f_{true} + f_{random} + f_{scatter}$) [22]. It provides a direct link between the image SNR and the true, random and scatter coincidence event rates. NEC depends in a complex manner on the scanner and detector geometry, the examined body (a larger body induces more Compton scattering) and the radiotracer activity (f_{true} and f_{random} have a linear and squared dependence on activity, respectively, see Eqs. 2.2 and 2.4). For PET scanners, NEC is often plotted as a function of radiotracer activity. This gives a characteristic curve that exhibits a maximum at a certain activity. This is the tracer activity for which the NEC, and thus the image SNR, is expected to be at its optimum value.

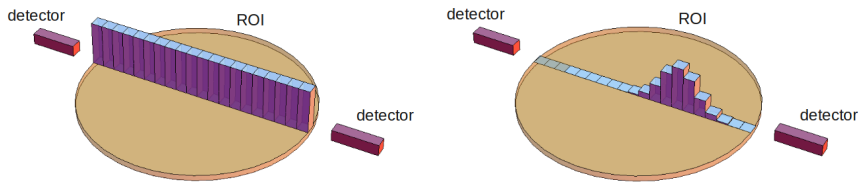

(a) Conventional reconstruction (b) Time-of-flight reconstruction

Figure 2.7: Conventional and TOF reconstruction. The conventional reconstruction does not provide any information about the origin of the annihilation event along the LOR in the region-of-interest (ROI). With TOF reconstruction, the measured difference in arrival times gives a probability distribution of this location.

2.2.4 Time-Of-Flight PET

In the previous section it was discussed that the background noise from random events could be reduced by using detectors with a good timing resolution, such that a small coincidence time window could be employed (see Eq. 2.4). This time window can not be made as small as possible, since there is a finite time-of-flight (TOF) difference between the gamma photons of an annihilation pair to reach the detectors. Reducing the time window too much would effectively decrease the FOV of the system. The detector ring diameter is typically 80 cm, and this distance is traveled by a gamma photon in about 2.7 ns at the speed of light.

The position of the positron annihilation along the LOR could directly be determined by accurately measuring the TOF difference of the two gamma photons. In this way, an image of the radionuclide concentration could directly be generated without the use of a tomographic reconstruction algorithm. The accuracy of the determined position along the LOR depends on the accuracy of the timing measurement:

$$\Delta x = \frac{c}{2}\Delta t \tag{2.6}$$

where Δx is the position resolution, c the speed of light and Δt the coincidence timing resolution. The coincidence timing resolution is the resolution with which the TOF difference between the two gamma photons of an annihilation pair is measured by two PET detectors. To achieve a position resolution of 4 mm along the LOR, a coincidence timing resolution of 27 ps would be required. At this moment, such a resolution is impossible to obtain. A coincidence timing resolution of a few hundred ps is possible, confining the positron position along the LOR to a line segment (7.5 cm long for 500 ps coincidence timing resolution). It is at present thus not possible to improve the spatial resolution by taking TOF information

into account. However, the confinement of the positron position along the LOR is effective to reduce the statistical noise in the reconstructed image if the line segment is shorter than the size of the emission source. This can be explained as follows [6]: With non-TOF reconstruction, the image pixels along the LOR are all incremented by the same amount, since there is no knowledge about the position of the positron source along the LOR, see Fig. 2.7(a). During tomographic reconstruction, the mean contribution to the pixels that do not correspond to the positron position is removed[7]. However, the statistical fluctuations in the measurement data can not be removed and add to the background noise in the reconstructed image. With TOF reconstruction, only the image pixels close to the positron event are incremented, see Fig. 2.7(b). The statistical fluctuations are thus only introduced around the positron location.

The reduction in statistical noise leads to an improvement in image SNR. The gain in SNR depends on the size of the emission source, and thus on the size of the examined body D_{body} [10]:

$$\frac{SNR_{TOF}}{SNR_{non-TOF}} \approx \sqrt{\frac{D_{body}}{\Delta x}} = \sqrt{\frac{2D_{body}}{c\Delta t}} \tag{2.7}$$

For whole-body imaging ($D_{body} \approx 40$ cm) and a coincidence timing resolution of 500 ps, this corresponds to a SNR gain of 2.3.

As pointed out in [6], the reduction in noise not only applies to true coincidence events, but also to random and scattered coincidence events. For random and scattered events, the effective size of the emission source (i.e., the size of the examined body that would be reconstructed using just the random or scattered events) is larger than for true events. This is shown in Figs. 2.6(b) and 2.6(c), where the mis-positioned LORs from the scattered and random events can be outside the region of the emission source. The reduction in noise will thus even be larger for random and scattered events, according to Eq. 2.7.

Since system sensitivity also influences the image quality in terms of image SNR, the inclusion of TOF information in the reconstruction can be considered as an effective sensitivity gain. An increase in the coincidence timing resolution for whole-body imaging thus improves the system performance in the same way as an increase in detector efficiency or detector solid angle coverage would achieve (Eq. 2.2). It was already discussed that system sensitivity was the most important performance parameter for PET (section 2.2.2). This explains the very active field of research into TOF-PET detectors for whole-body PET imaging.

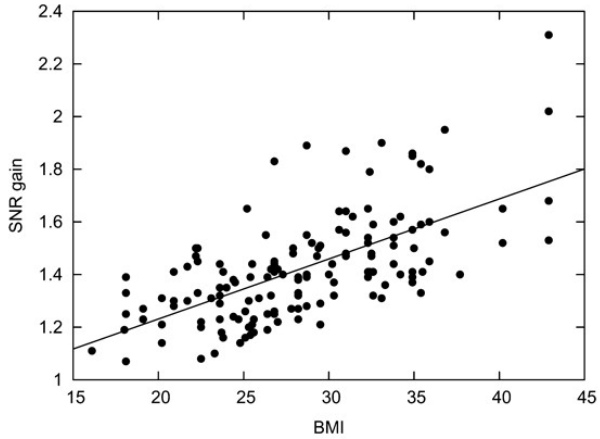

Figure 2.8: Measured SNR gain vs. BMI for small lesions (<2 cm) located in the abdomen for a group of 100 patients. From [7].

Clinical effectiveness

While an easy estimation of the gain in SNR due to TOF information can be made for a cylindrical water phantom with a uniform activity distribution (Eq. 2.7), this is much more difficult to predict for a patient. The improvement in SNR gain depends on the extent and distribution of positron activity in the patient body. In [7], patient studies were performed to assess the effect of TOF reconstruction on image quality, using a TOF-PET scanner with 590 ps FWHM coincidence timing resolution (Siemens Biograph TruePoint PET/CT). A quantitative analysis of the gain in SNR, as well as a subjective assessment of the image quality by nuclear medicine physicians was performed. Fig. 2.8 shows the achieved gain in SNR as function of patient body mass index (BMI) for tumors in the abdomen. The SNR gain in the range of 1.1 to 1.8 and the variation with BMI are consistent with the prediction according to Eq. 2.7. The improvement in image quality was qualitatively confirmed by the physicians, who saw an improvement in resolution of image detail, in the definition of small lesions and in image uniformity.

In [8], a 3D-mode TOF-PET scanner with 600 ps FWHM coincidence timing resolution was used (Philips Gemini TF) to determine the improvement in image quality in patient imaging. It was concluded that TOF information not only leads to an improvement in effective sensitivity, but also to a higher contrast recovery at matched noise level with faster and more uniform convergence of the tomographic reconstruction algorithm. From this work, clinical images with TOF and non-TOF

[7] In the conventional filtered backprojection algorithm this is done by applying a filtering procedure in the spatial frequency domain.

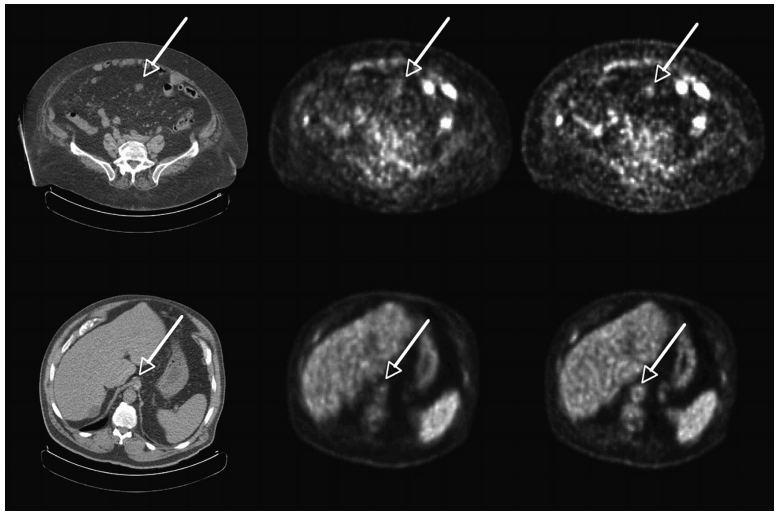

Figure 2.9: Representative transverse sections of 2 different patients: low dose CT (left), non-TOF PET (middle), and TOF PET (right). (Top) Patient 1 with colon cancer (119 kg, BMI = 46.5) shows a lesion in the abdomen much more clearly in the TOF image than in the non-TOF image. (Bottom) Patient 2 with abdominal cancer (115 kg, BMI = 38) shows structure in the aorta much more clearly in the TOF image than in the non-TOF image. From [8].

reconstruction of two heavy patients with cancer are shown in Fig. 2.9. Improved structural detail can be observed in the TOF reconstructions for both cases.

2.2.5 Multi-modality imaging

Recently, the majority of new clinical PET scanners have been associated with a CT scanner. The combination of both complementary techniques allows to coregister molecular information from the PET data with anatomic information from the CT data, thereby improving the sensitivity and specificity of PET for lesion detection. In addition, the CT scan can be used to correct for the gamma photon attenuation in PET (*attenuation correction*), eliminating the need for time consuming PET transmission scans.

The combination of PET and MRI is also interesting for clinical applications. The excellent soft-tissue contrast of MRI and the multifunctional imaging options, such as spectroscopy, functional MRI (fMRI) and arterial spin labeling, complement the molecular information of PET [23]. However, the integration of PET and MRI for simultaneous imaging is technologically much more challenging than PET-CT. The PET detector needs to be compact and insensitive to magnetic

fields, while it should not interfere with the magnetic field gradients and radiofrequency pulses of the MRI system. Nevertheless, MRI-compatible PET inserts have already been constructed and are applied in brain imaging, such as in [24].

3 PET Detector Components

Scintillation detectors are the most widely used radiation detectors in PET imaging. They are very fast, can have high stopping power and exhibit low electronic noise. A scintillation detector primarily consists of a scintillator, that produces scintillation light after interaction with radiation, and a photodetector that converts the scintillation light into an electrical signal. This chapter primarily discusses the scintillation detector components and design considerations. Section 3.1 discusses the scintillation mechanism and gives an overview of the common scintillators that are used for PET. Section 3.2 discusses the photodetectors for collecting the scintillation light. In section 3.3, an overview of various scintillation detector designs is given. Alternative radiation detectors for PET imaging are discussed in section 3.4. Section 3.5 introduces the detector concept used in this work.

3.1 Scintillators

Gamma photons can be detected with scintillators, which produce scintillation photons in the visible and ultraviolet range of wavelengths. Only photoelectric absorption and Compton scattering are important interaction mechanisms for detecting 511 keV gamma photons [18]. During a photoelectric effect, the entire energy of the gamma photon is converted to the release of a photoelectron, a *knock-on* electron. This electron then excites higher energy states of the crystal lattice, which decay by emitting lower energy scintillation photons. During Compton scatter, only part of the energy of the gamma photon is converted to the knock-on electron. The rest of the energy is taken by the scattered, "degraded" photon. This scattered photon in turn can produce additional scintillation centers by the Compton and photoelectric effect. Compton scattering inside the scintillation crystal can thus produce various scintillation centers. This *position blurring* affects the position determination. Unlike Compton scatter, the photoelectric effect produces a single scintillation center and is the preferred interaction process. The photoelectric cross section σ_p is a function of the density ρ and of the effective atomic number[1] Z_{eff} of the crystal. The photoelectric cross section is proportional to ρZ_{eff}^x, with the power x varying with gamma energy between 3 and 4, typically. In contrast, the Compton cross section is linearly related to the electron

[1] Z_{eff} is the atomic number that represents the attenuation properties of a mixture of atoms in a molecule. It is defined as $Z_{eff} = \sqrt[x]{\sum_{i=1}^{n} \omega_i Z_i^x}$, where the mass weighting factor ω_i is defined as $\omega_i = \frac{m_i Z_i}{\sum_{j=1}^{n} m_j Z_j}$, where m_i is the number of atoms of element i in the molecule. The power x is dependent on the energy of the gamma rays, and typically varies between 3 and 4.

density, and thus proportional to ρ [25]. A scintillator should thus have a high density for a high absorption probability and a high atomic number for a large fraction of events undergoing photoelectric absorption. These two requirements are commonly parametrized as the attenuation length $1/\mu$ (the distance into a material where the probability has dropped to $1/e$ that a particle has *not* been absorbed) and photoelectric absorption probability PE or photofraction (defined as the probability that a gamma photon interacts by the photoelectric effect instead of the Compton effect: $PE = 100 \cdot \frac{\sigma_p}{\sigma_p + \sigma_c}$).

High light yield (number of emitted scintillation photons per MeV absorbed energy) is another important requirement for PET. A large number of detected scintillation photons N_{ph} implies a high energy, timing and position resolution. This is because photon counting is dominated by Poisson statistics, such that the relative statistical spread is proportional to $1/\sqrt{N_{ph}}$. Associated with the light yield requirement is a high light collection efficiency of the crystal, such that a large fraction of the emitted scintillation photons are detected. Optical self-absorption of the scintillation photons should therefore be minimal. Furthermore, the scintillator can be surrounded by a reflector at all surfaces except that at which the photosensor is located, to recapture the light that would otherwise escape from the crystal. Also, the emission spectrum should overlap with the spectral sensitivity of the photodetector. It is further desirable that the light output is proportional to the deposited energy. If this would not be the case, the light output would be different for a full 511 keV energy absorption by a single photoelectric effect, compared to a full energy absorption by multiple, lower energy, Compton interactions. This would broaden the full energy peak.

The decay time of the excited state should be fast enough to allow a short coincidence time window, to limit the amount of random coincidences. A fast decay time also allows a high count rate performance of the detector. This is especially important for 3D-mode PET, where high counting rates exist and the system sensitivity will be limited by pulse pile up if slow scintillators are used. Additionally, a fast decay time (as well as a high light yield) implies a large initial scintillation photon emission rate I_0, such that a high timing resolution can be obtained for TOF-PET. For timing, it is also important that the scintillator has a fast *rise time*. The rise time is associated with the luminescence process in scintillators. Like a fast decay time, a fast rise time is associated with a large initial scintillation photon emission rate I_0.

Scintillator materials can be organic-based (liquid or plastic) or inorganic. Organic scintillators are generally fast, but have a low light yield. Inorganic scintillators have a higher light yield, but are relatively slow. For all current commercial PET scanners, inorganic scintillators are applied.

3.1.1 Scintillation mechanism in inorganic scintillators

The scintillation mechanism in inorganic scintillators is due to the electronic band structure found in crystals, whereby the conduction band is separated from the valence band by a forbidden energy gap of 4-12 eV. Ionizing radiation causes electrons from the valence band to jump to the conducting band, where they have sufficient energy to mitigate throughout the crystal. Inorganic scintillators commonly contain impurities. These impurities, called *activators*, create special sites in the lattice with a modified band structure. At these sites additional energy states are created within the forbidden energy gap through which the electron can de-excite back to the valence band. The energy of this transition is less than the full energy gap, such that photons in the visible range are created. These de-excitation sites are the *luminescence centers* from which scintillation can take place. Due to the presence of these activators, scintillators are transparent to scintillation light: since the energy of the de-excitation transition is less than the required energy to elevate an electron from the valence to the conduction band, the emission and absorption spectra do not overlap and self-absorption by the crystal is minimal.

3.1.2 Typical inorganic scintillators for PET

As mentioned before, scintillator materials suitable for PET have a small attenuation length, high photofraction, high light yield and fast decay time. The properties of several relevant inorganic scintillators for PET imaging are summarized in Table 3.1.

Bismuth germanate (BGO) has a high density and high effective atomic number Z_{eff} and, therefore, a high detection efficiency for 511 keV gamma photons and a high photofraction PE. The photoelectric cross section σ_p at 511 keV for BGO is 1.6 times that of LSO and 5.8 times that of NaI:Tl [13]. However, its light yield and decay time are inferior compared to the other crystals. This makes it less suitable for fast timing applications, limits the countrate capabilities and increases the number of random coincidences due to the requirement of a wide coincidence window. Due to its high detection efficiency and the widespread availability, BGO has in the past been the most widely used scintillator for commercial PET scanners.

NaI:Tl has high light yield, but low detection efficiency and a low photofraction. Furthermore, it is hygroscopic (it reacts with water), which requires that the crystal is hermetically sealed to prevent the entrance of moisture.

Lutetium oxyorthosilicate (LSO) is arguably the most suitable scintillator for PET and TOF-PET imaging to date. It combines high detection efficiency (attenuation length of 12.3 mm), a high photofraction (34 %), high light yield (30,000 photons/MeV), short decay time (40 ns) and a short rise time (0.5 ns, see [26]). It is not hygroscopic and has good mechanical properties. A disadvantage of the material is the non-proportionality of the light output to the deposited energy [13].

Table 3.1: Properties of common scintillators used for PET (Data from [10])

	NaI	BGO	GSO	LSO	LYSO	LGSO	LuAP	YAP	$LaBr_3$
Peak emission wavelength (nm)	410	480	440	420	420	415	365	350	360
Index of refraction	1.85	2.15	1.85	1.82	1.81	1.8	1.94	1.95	1.9
Light yield (10^3 ph/MeV)	41	9	8	30	30	16	12	17	60
Decay time (ns)	230	300/60	60/600	40	40	65	18	30	16
I_0 at 511 keV (ph/ns)	90	21	60	380	380	125	340	290	1,900
$\triangle E/E$ (%) at 662 keV	6	10	8	10	10	9	15	4.5	3
Density ρ (g/cm^3)	3.67	7.13	6.71	7.35	7.19	6.5	8.34	5.5	5.3
Effective Z (Z_{eff})	50	73	58	65	64	59	65	33	46
$1/\mu$ at 511 keV (mm)	25.9	11.2	15.0	12.3	12.6	14.3	11.0	21.3	22.3
PE (%)[a]	18	44	26	34	33	28	32	4.4	14
PE^2 (%)[b]	3.2	19	6.8	12	11	7.9	10	0.20	1.9
Hygroscopic	Yes	No	No	No	No	No	No	No	Yes
Magnetic susceptibility	No	No	Yes	No	No	Yes	No	No	No

NaI thallium-doped sodium iodide (NaI:Tl), *BGO* bismuth germanate ($Bi_4Ge_3O_{12}$), *GSO* cerium-doped gadolinium orthosilicate (Gd_2SiO_5:Ce), LSO cerium-doped lutetium orthosilicate (Lu_2SiO_5:Ce), *LYSO* cerium-doped lutetium-yttrium oxyorthosilicate ($Lu_{1.9}Y_{0.1}SiO_5$:Ce), *LGSO* cerium-doped lutetium-gadolinium oxyorthosilicate ($Lu_{0.4}Gd_{1.6}SiO_5$:Ce), *LuAP* cerium-doped lutetium-aluminum perovskite ($LuAlO_3$:Ce), *YAP* cerium-doped yttrium-aluminum perovskite ($YAlO_3$:Ce), $LaBr_3$ cerium-doped lanthanum bromide ($LaBr_3$:Ce)

[a] Photoelectric absorption probability (or photofraction) at 511 keV: $PE = 100 \times \sigma_p/(\sigma_p + \sigma_c)$

[b] Coincident photoelectric absorption probability

This results in a difference in light output between a full energy peak from the photoelectric effect and a full energy peak from multiple lower energy interactions due to Compton scattering, thus broadening the energy spectrum. Another disadvantage is the presence of a naturally long-lived lutetium isotope (^{176}Lu) with 2.6 % abundance and a half-life of 4×10^{10} years, undergoing β^--decay. From the abundance, half-life, density and atomic mass one can easily calculate that this isotope accounts for a background singles count rate of 280 counts per second in 1 cm^3 LSO. Since PET scanners are operated in coincidence mode, the majority of these events are automatically filtered out. Still, the number of random coincidences will be higher. For clinical scans the presence of this isotope has negligible impact. However, it may have an impact on dedicated small animal PET in research studies with low count rates [13]. Recently, it was found that the scintillation properties of LSO could significantly be improved by co-doping the crystal with Ca^{2+}. A scintillation output of 38,800 photons/MeV was achieved, while the scintillation decay time was as short as 31 ns [27], thus making the crystal even more attractive for (TOF-)PET.

Lutetium aluminum perovskite (LuAP) has a high detection efficiency (attenuation length of 11 mm), high photofraction (32 %), very short decay time (18 ns), short rise time (0.6 ns, see [26]), but relatively low light yield (12,000 photons/MeV). Due to its favorable properties, there has been a great deal of interest in developing practical scintillators from this material. Useful crystals were, however, limited to thicknesses less than a centimeter because of strong self-absorption of the scintillation light [28, 29]. Like LSO, LuAP contains the natural background of the ^{176}Lu isotope.

Lanthanum bromide ($LaBr_3$:Ce) is a relatively new scintillator [30]. It has very high light yield (60,000 photons/MeV), very short decay time (16 ns) and a short rise time (varying between 0.2 and 0.9 ns, see [26]), and is therefore well-suited for TOF-PET. It has excellent energy resolution (3 % FWHM at 662 keV), enabling efficient rejection of Compton-scattered events within the patient. The very good energy resolution follows from the high light yield, but also from the very small non-proportionality of the light yield with the absorbed energy [25], such that a small difference in light output exists between a full energy peak from the photoelectric effect and a full energy peak from multiple lower energy interactions during Compton scattering. The detection efficiency (attenuation length of 22.3 mm) and photofraction (14 %) are, however, inferior compared to the other scintillation crystals. This means that thick scintillation crystals are required in order to obtain sufficient stopping power. The larger crystal dimension and the low photofraction both lead to an increased fraction of events for which the gamma photons undergo multiple scattering, deteriorating the obtainable spatial resolution. The larger crystal dimension further enhances the degradation from the parallax effect, if no information about DOI is provided (see section 2.2.3).

$LaBr_3$:Ce is hygroscopic and requires hermetic sealing.

3.2 Photodetectors

A photodetector is required to convert the weak light output of a scintillation pulse into a detectable electrical signal. Photomultiplier tubes and solid-state photodetectors are the two main groups of devices for detecting low light levels. Both groups of devices work by transferring the photon energy to an electron by a collision. Two processes can be distinguished. During a photoelectric effect, an electron is liberated when a photon impinges on the surface of a material. The photon energy E_{ph} should be higher than the photoelectric workfunction ϕ, in order for this process to happen. The excess photon energy is transferred to the kinetic energy of the liberated electron E_{kin}

$$E_{kin} = E_{ph} - \phi \tag{3.1}$$

The workfunction thus defines the low-energy limit of the light spectrum that can be detected. Standard bialkali photocathodes in photomultiplier tubes have a high-wavelength threshold at 630 nm (red light) [31]. The second process requires less energy. In a semiconductor an electron can be lifted from the valence to the conduction band. When an electric field is applied, as in a silicon photodiode, the electron can hardly recombine with holes and it is possible to collect and detect the electron. Because of the low energy requirement, such a photodetector can be very efficient. Photodetectors usually multiply the photoelectrons produced by the incident light. This produces a large electrical current even from a single photoelectron, making such photodetectors sensitive to a single incident photon.

Characteristics of various photodetectors are given in Table 3.2.

3.2.1 Photomultiplier tubes

Photomultiplier tubes (PMTs) are extremely sensitive photodetectors. They combine high gain, stability and low noise and are the standard photodetectors used for scintillation detectors. A schematic view of a PMT is shown in Fig. 3.1. PMTs consist of a light transmitting window, a photocathode, a series of electrodes (dynodes) and an anode, all housed in a glass envelope with high vacuum inside. Photons incident on the photocathode liberate photoelectrons by the photoelectric effect into the vacuum. The photoelectrons are accelerated towards the first dynode such that they arrive at much higher energy. The impact of these photoelectrons liberates secondary low-energy electrons which in turn are accelerated towards the second dynode. The repeated structure results in a cascade of electrons which is finally collected by the anode, where a sharp current pulse is produced.

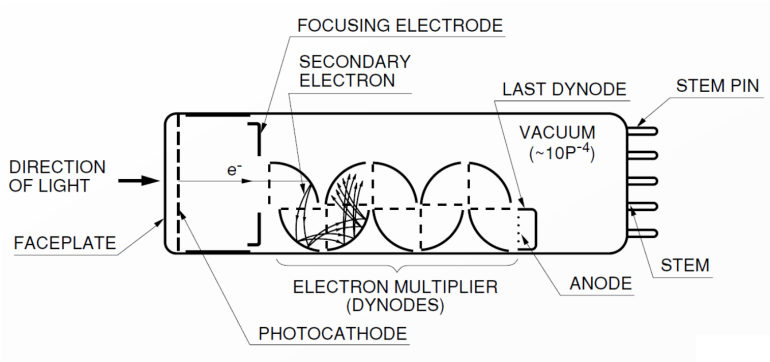

Figure 3.1: Construction of a photomultiplier tube. From [32].

The main characteristic of the PMT is its *quantum efficiency* (QE). This is the probability that a photoelectron is liberated from the photocathode by an incident photon. The QE is a strong function of the wavelength of the incident light and depends on the transmitting window and photocathode properties. PMTs typically show maximum QE values of 20-30 %[2], lower than what can be achieved with solid-state photodetectors.

The transmitting window or faceplate acts as a seal to maintain a vacuum within the PMT. Borosilicate glass is the most commonly used window material. The sensitivity of a PMT in the ultraviolet region is primarily limited by the transmitting window due to absorption inside the glass. Borosilicate glass does not transmit ultraviolet radiation shorter than 300 nm. For this purpose, some PMTs contain UV-glass or quartz that extends the transmittance down to 185 nm and 160 nm, respectively. The refractive index of the transmitting window is typically 1.5 and the window thickness about 1 mm. The refractive index value differs from the index value for scintillators of around 1.9 (Table 3.1), resulting in losses due to optical refraction. Scintillation light undergoes total internal reflection from the window glass as soon as the angle of incidence exceeds the critical angle θ_c, defined by Snell's law:

$$\theta_c = sin^{-1} \frac{n_w}{n_s} \tag{3.2}$$

where n_w and n_s are the refractive indices of the window material and scintillator, respectively. The window is thus only transparent for light entering a cone of aperture $2\theta_c$.

[2]Recently, Hamamatsu developed PMTs with so-called Super Bialkali (SBK) and Ultra Bialkali (UBK) photocathodes, which show maximum QE values of 35 % and 43 %, respectively [33].

A photocathode is a semitransparent layer covered at the inner side of the transmitting window from which the primary photoelectrons are liberated by the photoelectric effect. The photocathode primarily determines the light response characteristic of the PMT as a function of wavelength. Most photocathodes are made of semiconductor material with a low workfunction. Bialkali photocathodes are widely used and have a maximum sensitivity at 420 nm.

The dynode system effectively acts as the multiplication stage of the PMT and determines the gain. It is a low noise amplification, whereby the noise is only introduced by the stochastic character of the emission of secondary electrons [31]. The gain is determined by the number of dynodes and the interstage voltages of the dynodes and typically varies between 10^6-10^7. The dynodes are carefully arranged, such that optimal focusing is achieved at each element. Often, an additional (last) dynode signal is available from the PMT. This signal is directly sensed from the (last) dynode and occurs because the sudden liberation of many secondary electrons from the dynode results in a potential variation. Its amplitude is comparable to that of the anode.

The anode collects the secondary electrons and forms a detectable output pulse. Adequate design is necessary to prevent space charge effects.

The time response of the PMT is primarily determined by the transit time required for the photoelectrons to reach the anode after being emitted from the photocathode and multiplied. The fluctuation on this transit time of each photoelectron is called the transit time spread (TTS). The time response mainly depends on the dynode type and the supply voltage. Increasing the supply voltage improves the electron transit speed and shortens the transit time and TTS. Transit time and TTS both improve in inverse proportion to the square root of the supply voltage [32]. Metal channel type dynodes have a special structure for optimal timing, consisting of extremely thin dynodes that are precisely stacked in close proximity to ensure short electron path lengths. For these dynodes typical values for the anode pulse rise and fall time are 0.65-1.5 ns and 1-3 ns, respectively. The transit time and TTS are 4.7-8.8 ns and 0.4 ns, respectively [32]. Another dynode type which exhibits the best timing properties among currently available dynode types is the microchannel plate (MCP). It consists of a compact array of micrometer sized glass capillaries (microchannels) bundled in parallel. Each channel acts as an independent electron multiplier, whereby the inner surface acts as the secondary electron emitter. A TTS of 25 ps is possible, with rise and decay times of 150 and 360 ps, respectively (specified for a Hamamatsu R3809U-50 MCP-PMT, [34]).

A special kind of PMT is a multianode PMT (MAPMT) that collects the amplified electron current on multiple anodes. A MAPMT type with a focusing mesh of metal channel dynodes is shown in Fig. 3.2. The electron multiplication process in this dynode system has minimal spatial spread, such that the MAPMT is position sensitive. The channels of the MAPMT effectively act as independent PMTs,

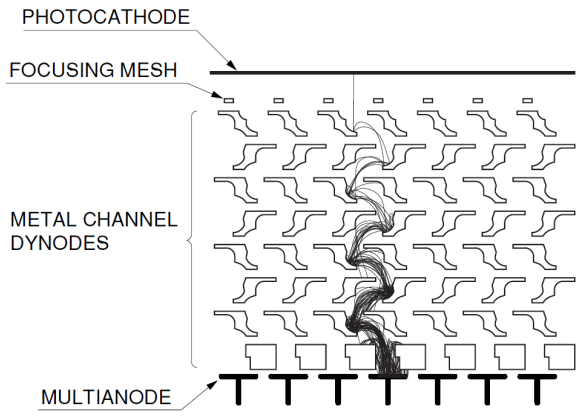

Figure 3.2: Dynode structure of a metal channel dynode type MAPMT. Electron amplification is illustrated. From [32].

but with minimal dead space in between them. This allows fine sampling of the spatial distribution of the scintillation light from a crystal. The MAPMT also provides a (last) dynode signal which is common for all channels. This signal is extremely useful, since it contains the total amount of detected light, and thus directly provides information about the energy deposited in the scintillation crystal. This can thus be used for energy discrimination and/or serve as a timing signal. Due to the segmented character of the anode system, the anode signals would have to be summed in order to get energy information, while a complicated electronic design would be necessary to obtain a timing signal from a combination of the anode signals if the dynode signal was not present. Position sensitive multianode versions of the MCP-PMT are also available.

Drawbacks of PMTs compared to solid-state photodetectors are their relatively low QE of 20-30 %, their large size and their sensitivity to magnetic fields. Because they are bulky, close packing of PMTs in a scanner is difficult. The sensitivity to magnetic fields limits their application in combined PET-MRI systems. Advantages are their high gain, such that additional electronic amplification is not necessary, and their low dark current.

3.2.2 Solid-state photodetectors

Solid-state photodetectors have the advantage that they are compact and essentially transparent to 511 keV gamma rays, allowing close packing and novel crystal read-out designs. Because they can be produced in fully automatic processes, they have the potential for low cost. They are also insensitive to magnetic fields, thus

Table 3.2: Characteristics of photodetectors for PET (Data from [10])

	PMT	APD	SiPM
Active area (mm^2)	1-2,000 cm^2	1-100 mm^2	1-10 mm^2
Gain	10^5-10^7	10^2	10^5-10^6
Dynamic range	10^6	10^4	$10^3/mm^2$
Excess noise factor	0.1-0.2	>2	1.1-1.2
Rise time (ns)	<1	2-3	∼1
Time jitter (ns FWHM)	0.3	>1	0.1
Dark current/countrate	<0.1 nA/cm^2	1-10 nA/mm^2	0.1-1 MHz/mm^2
Capacitance (pF/mm^2)	8.6±0.4	2-10	>30
QE @ 420 nm (%)	25 %[a]	60-80 %	<40 %[b]
After-pulsing	Yes	No	Yes
Bias voltage (V)	1,000-2,000	∼100-1,500	∼50
Power consumption	100 mW/ch	10 $\mu W/mm^2$	<50 $\mu W/mm^2$
Temperature coefficient	<1 %/K	2-3 %/K	3-5 %/K
Bias coefficient	<1 %/V	<10 %/V	∼100 %/V
Magnetic susceptibility	Very high (mT)	No (measured up to 9.4T)	No (measured up to 15T)

[a] The recently introduced Super Bialkali (SBK) and Ultra Bialkali (UBK) PMTs from Hamamatsu have maximum QE values of 35 % and 43 %, respectively [33].

[b] This is the Photon Detection Efficiency: $PDE = QE \cdot \varepsilon \cdot P_{br}$, where ε is the geometric fill factor and P_{br} the probability that an incoming photon triggers a breakdown, see section 3.2.2.

allowing PET-MRI integrated systems. A low bias voltage is required to operate these devices. Because of the thin active layer, the charge moves over small distances, such that they can exhibit good timing performance. Since the photon detection is not limited by the need for the photoelectrons to escape from the surface, like in a photocathode, the maximum QE of 80 % is much higher compared to PMTs. It is sufficient to lift electrons from the valence to the conduction band. The maximum QE also spans almost the whole range of visible light [35].

Photodiodes

Conventional photodiodes have no internal gain, but simply collect the electron-hole pairs produced by the incident light. This results in small signal amplitudes when operated in pulse-mode, whereby electronic noise is a major problem. For scintillators operated in integrating detection mode, like in X-ray CT scanners, the cumulative effect of many scintillation events at high rates overrides the inherent noise of the photodiodes [18]. Due to their high electronic noise, these photosensors have limited use in PET, which requires pulse mode operation.

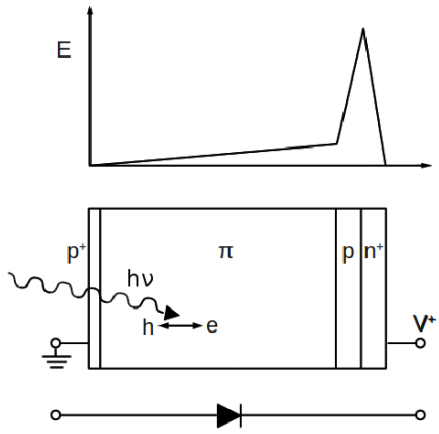

Figure 3.3: Schematic view of a reversely biased APD in reach-through configuration

Avalanche photodiodes

Avalanche photodiodes (APDs) do provide internal gain. These devices commonly have a *reach-through configuration*, consisting of a thin p^+ layer, a wide (>100 μm) depleted drift region (π) and an avalanche region (p and n^+) (Fig. 3.3). A reverse bias voltage is applied on these devices. The avalanche region contains high doping concentrations, such that a high internal electric field is created within this region when the reverse bias is applied. Light enters and interacts within the π region, producing electron-hole pairs. The electric field drifts the electrons towards the avalanche region, where the high electric field accelerates the electrons towards energies capable to ionize Si atoms. This ionization creates secondary electrons that in turn can ionize more Si atoms. This effectively acts as the internal gain process in APDs.

Gains between 50 and 200 are typical, which are much lower compared to the typical gains of 10^6 - 10^7 for PMTs. Therefore, the internal electronic noise of the devices is still relatively high compared to the signal amplitude. Moreover, the multiplication process in APDs itself has a higher inherent noise contribution compared to PMTs, which is parametrized by the excess statistical noise factor F [36]. APDs thus not only have a lower gain, but also a higher statistical variation on this gain. The actual gain depends on the applied reverse voltage and temperature. It varies exponentially with reverse voltage, such that the relative change of gain with voltage is a linear function of the gain. At a gain of 100 the relative change of the gain with voltage is ∼10 %/V, while the relative change with temperature

is typically ∼2-3 %/K [10]. For stable operation at a constant gain, it is therefore necessary to control the reverse voltage and temperature. Higher gains up to 1,000 are possible, but at the cost of a higher excess multiplication noise and a higher variation of the gain with reverse voltage and temperature. APDs are therefore normally operated at moderate internal gains. Because of the low internal gain, low-noise and fast front-end electronics are required to achieve additional signal amplification.

In addition to excess multiplication noise, a relatively high dark current is present in APDs. The timing performance is further inferior to PMTs, due to the relatively low gain. However, compared to PMTs, APDs have a much higher QE of typically 60-80 % (see Table 3.2). They also have the advantages of compactness and insensitivity to magnetic fields. Although they have a higher inherent noise than PMTs, energy resolutions of ∼11 % FWHM were obtained for the 511 keV full energy peak for LYSO crystals coupled to APDs [37], which is the expected energy resolution for LYSO. The system performance of PET is thus not necessarily limited by the excess multiplication noise of APDs.

APDs typically have a maximum size limited to about 1 cm^2. For large area readout, arrays of APD pixels exist [38]. Large-area position sensitive APDs (PSAPDs) with a reduced number of electronic channels are also available [39–41]. These PSAPDs contain four corner contacts placed on the backside, covered by a high resistivity layer. From the signals of the four corner contacts the position of the impinging light can be calculated. Although the number of channels is reduced, the noise of these PSAPDs is generally worse than that of standard APDs [42].

Silicon photomultipliers

Silicon photomultipliers (SiPMs) consist of a densely packed matrix of small (20×20 - 100×100 μm^2) APD cells. The APD cells are all reversely biased above avalanche breakdown (Geiger mode operation) and connected in parallel. In this mode, the internal electric field becomes so high that a very high gain (10^5-10^6) is obtained. Both electrons and holes are now involved in the multiplication process and this multiplication is self-sustaining. Quenching resistors are present to stop the avalanche after a breakdown and to recharge the cell. The avalanche breakdown and subsequent quenching results in a standardized output signal for a single cell, independent of the energy and number of the incoming photons. Energy information is thus essentially lost and a single cell thus functions in digital/switching mode. Because the APD cells are all connected in parallel, the output of the SiPM as a whole is the summed output of the individual cells. This makes the SiPM an analog device, since a wide dynamic range of photons can still be sensed.

Because of the high gain, the device is sensitive to single photons. The energy resolution is even superior to that of PMTs [43], and at low light levels the number

of detected photons can precisely be determined from the detected charge or pulse height (see Fig. 6.1). This proves that there is little gain variation among the cells and that the excess noise factor is very small, due to the standardized output signal following an avalanche breakdown.

The signal pulse shape is quite short, as will be shown in section 6.3 on the pulse shape of a single photoelectron. The signal decay time τ is the same as the cell recovery time and depends on the cell capacitance C and the quenching resistor R: $\tau \sim RC$ (as well as on the shaping time of the front-end amplifier, obviously). The devices show an excellent internal single photoelectron timing resolution of ∼100 ps RMS (see section 6.3). Combined with the high gain and fast response, this makes the timing performance at least as good as that of PMTs, and a coincidence resolving time (CRT) of 100 ps FWHM was obtained using $LaBr_3$ scintillators (see section 8.3.1).

Between the microcells some space is needed for optical separation and for the individual resistors. This limits the area of the sensitive region of the SiPM. Although solid-state photodetectors have a superior QE compared to PMTs (see Table 3.2), this geometric effect lowers the maximum achievable detection efficiency for SiPMs. The *photon detection efficiency* (PDE) is defined by the QE of the active area, the geometric fill factor ε (ratio of the sensitive area), and the probability that an incoming photon triggers a breakdown P_{br}:

$$PDE = QE \cdot \varepsilon \cdot P_{br} \tag{3.3}$$

The microcell size thus determines the geometric fill factor. A large microcell size implies a high PDE, but a low dynamic range since there are less cells per unit area. This size thus needs to be optimized for the particular application involved.

Because of the finite number of cells, the response of the SiPM is non-linear. Saturation in the output occurs when the number of photoelectrons becomes comparable to the number of cells. The number of detected photons $N_{detected}$ during a scintillation pulse can be calculated from the number of cells N_{cells}, number of incoming photons $N_{photons}$ and PDE as follows:

$$N_{detected} = N_{cells} \left(1 - e^{\frac{-PDE \cdot N_{photons}}{N_{cells}}} \right) \tag{3.4}$$

This equation is not exact, since it ignores the finite recovery time of a microcell and thus assumes that a microcell can only fire once during a scintillation event.

Apart from their non-linear response and reduced PDE, SiPMs have a quite high dark count rate (0.1-1 MHz/mm^2, Table 3.2) due to thermal generation of free carriers in each microcell. This is not necessarily a bottleneck for PET: a simple low energy threshold filters most of these dark counts, since their energy content is at most equal to a few microcell discharges. SiPMs further exhibit after-pulsing from carrier trapping and delayed release, as well as from optical crosstalk between

neighboring cells. This artificially increases the energy content of the scintillation pulses and also effectively increases the excess multiplication noise of the SiPM sensor. Both the dark count rate and after-pulsing increase with the gain of the device. The gain strongly depends on the reverse bias voltage and temperature. The gain G is determined by the bias voltage V_b above the breakdown voltage V_{br} (also called overvoltage, typically varying between 1-3 V) and the cell capacitance C

$$G = (V_b - V_{br}) \cdot C/q \tag{3.5}$$

where q is the electron charge. The breakdown voltage varies strongly with temperature on the order of 50 mV/K [31]. Since the gain depends on the overvoltage, both the bias voltage and temperature need to be stable for constant gain. The PDE strongly increases with the gain through the dependence of P_{br} on overvoltage [43]. However, the overvoltage can not be set to very high values, since the SiPM operation will be hampered by spontaneous breakdowns and an increasing dark count rate and afterpulsing.

Because of the high gain, a front-end amplifier is in principle not necessary, and a simple 50 Ohm load can be used to produce signals of several millivolts for single photons [43]. In practice, additional front-end amplifiers with a typical gain of around 10 are used to improve the SNR and detection efficiency of the signals.

An interesting new development is the digital SiPM (dSiPM) from Philips Research [44, 45]. In this sensor, each detected photon is directly converted to a digital signal for each microcell. In addition, the complete trigger logic and time-to-digital converter are integrated onto the sensor. The output of the sensor consists of the number of detected photons and the corresponding time stamp. Since the detected photons are directly digitized, the analog signal generation stage has essentially been removed, such that the detector performance is much less affected by electronic noise. Moreover, since the output of the sensor does not depend on the gain of the individual microcell anymore, the output variation with temperature is an order of magnitude less compared to conventional analog SiPMs. Further, an on-chip saturation correction can be performed using Eq. 3.4. Due to the minimal electronic noise, an excellent CRT of 153 ps FWHM was obtained for LYSO crystals coupled to these dSiPMs [44].

3.3 Scintillation detector designs

The early PET systems consisted of scintillators coupled one-to-one to individual PMTs. The spatial resolution was determined by the scintillation crystal size. As the crystal size was reduced to improve the spatial resolution, the one-to-one coupling scheme could not be retained. The number of PMTs and electronic

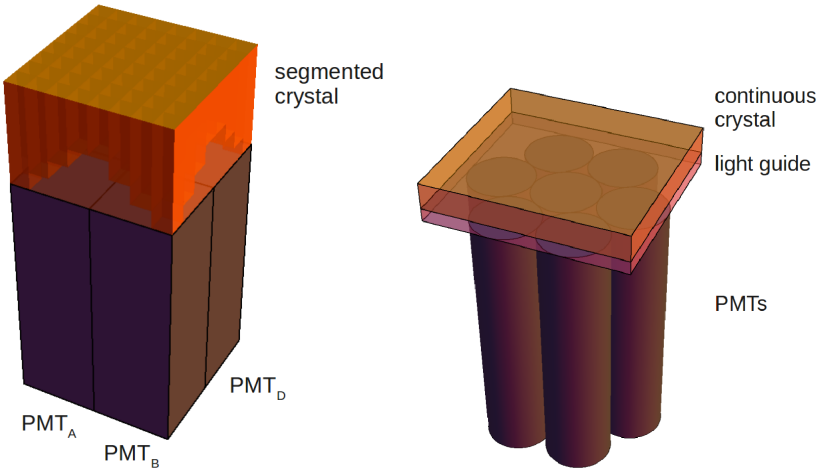

(a) Block detector (b) Gamma camera

Figure 3.4: Early PET detector designs. (a) Block detector consisting of crystal segments, separated by partial saw cuts. The crystal elements are read out by 4 PMTs. (b) Gamma camera consisting of a continuous crystal, read out by a hexagonal array of PMTs through a light guide.

channels had to be kept as low as possible for low cost, while the PMT size could not be made as small as possible. In order to continue to improve the spatial resolution, it was thus necessary to determine the gamma interaction position with an accuracy that was a fraction of the PMT size. This necessarily required that the scintillation light was shared over multiple PMTs, whereby the position was calculated based on the detected light level of each PMT.

The *block detector* allows the use of a small number of PMTs, reading out an array of small crystal elements [46]. Typically, a block detector consists of four PMTs in a rectangular pattern, reading out the crystal elements. The crystal elements are either individual crystals or crystal segments from a block of scintillator, separated by partial saw cuts, see Fig. 3.4(a). The surfaces of each individual crystal element are covered with reflective material to channel the light with low spatial spread towards the PMT and minimize the optical cross-talk between the crystal elements. The depth of the saw cuts is such, that a well-defined light response function (LRF) over the PMTs is produced, and a simple linear positioning scheme based on the ratio of the detected light levels can be used to identify the

crystal segment in which an interaction took place:

$$X = \frac{(PMT_A + PMT_B) - (PMT_C + PMT_D)}{PMT_A + PMT_B + PMT_C + PMT_D} \tag{3.6}$$

$$Y = \frac{(PMT_A + PMT_C) - (PMT_B + PMT_D)}{PMT_A + PMT_B + PMT_C + PMT_D} \tag{3.7}$$

where PMT_A, PMT_B, and so forth are the detected light levels from the respective PMTs. The intrinsic spatial resolution is thus defined by the crystal element size, instead of the PMT size. This allows a low number of PMTs and thus low cost, while providing high spatial resolution. Because the light is channeled towards the PMTs with low spatial spread, thick scintillation crystals can be used for high sensitivity while maintaining good spatial resolution.

The other detector design consists of a large flat unsegmented crystal plane, read out by an array of PMTs, the *Anger camera* or *gamma camera*, see Fig. 3.4(b). This design was invented in 1958 [47] and used for planar imaging (i.e. 2D-imaging) of gamma photon emitting radioisotopes, *scintigraphy*. In planar imaging and SPECT the gamma camera contains collimation holes to define the direction of the impinging gamma photons. The gamma camera has also been used for PET imaging, but of course without the presence of the collimator[3]. Since the scintillation light is not channeled to the PMTs, it is spread out over a larger number of PMTs. This requires a scintillator with a high light output, in order to minimize the statistical spread associated with photon counting. The gamma camera was developed for the NaI:Tl scintillator (which has a high light output, see section 3.1) and 140 keV gamma-rays (^{99m}Tc radioisotope). For 511 keV annihilation gamma-rays, NaI:Tl has a low linear attenuation coefficient and low photoelectric absorption probability, see section 3.1.

The segmented or unsegmented (continuous) nature of the crystals distinguishes these two designs and remains the most basic feature of present-day scintillation detector designs for PET.

3.3.1 Segmented vs. continuous designs

As mentioned, the segmented crystal design channels the scintillation light towards the photosensor with minimal spatial spread. A well-defined light response function (LRF) is generated on the front face of the photosensor, such that a small number of photosensors and a simple (linear) positioning scheme can be used. The spatial resolution is defined by the crystal segment size. Since the light is channeled towards the photosensor, this spatial resolution is constant over the DOI-range of the crystal. The crystal segments can thus originate from a thick (30 mm) block

[3]In PET, a collimator is not necessary since the direction of the gamma photons is known from the coincident detection nature, see section 2.2.

of scintillator for high stopping power, while maintaining good spatial resolution. Nearly all commercial scanners employ the segmented crystal design.

However, there are a number of drawbacks with this design compared to the continuous crystal design:

- As one aims to improve the spatial resolution, the cross-sectional area of the crystal segments needs to become smaller. However, the costs increase dramatically due to the increase in complexity to manufacture smaller crystal segments and due to the larger number.

- Because of the finite thickness of the reflective material between the crystal segments, a volume fraction of the segmented crystal contains non-scintillating material, i.e. dead space. This reduces the detection efficiency of the segmented crystal.

- The cross-sectional area of the crystal segments needs to be small for good position resolution, while the length should be large for good detection efficiency. For long and narrow crystal segments the scintillation photons undergo multiple reflections before reaching the photosensor. Since crystal surfaces are never perfectly reflective, a fraction of the scintillation light will be lost. The light collection efficiency for segmented crystals is thus generally lower compared to continuous crystals. This means that the energy and timing resolution of continuous crystals is generally better compared to segmented crystals, since both parameters depend on the number of detected scintillation photons (see section 3.1).

- Continuous crystals inherently provide information about the DOI, while complicated and expensive detector modifications are necessary to enable DOI detection for segmented crystals. This last point will further be discussed in section 3.3.3.

For continuous scintillators, the linear positioning scheme in Eqs. 3.6 and 3.7 can in principle be used, however it leads to strong artifacts near the crystal borders. More complex statistical methods can be used for more accurate position estimation, like maximum likelihood estimation (MLE), neural networks or nearest neighbor estimation. Spatial resolutions below 2 mm FWHM can be reached with these methods [37, 48–50], which is better than for segmented scintillators with a typical crystal segment size of 4 mm (e.g., the Philips Gemini TOF PET/CT scanner employs $4\times4\times22$ mm^3 LSO crystals [51]). These estimation methods all work by finely sampling the LRF from the continuous crystal using a photosensor array.

A major drawback of continuous scintillators with respect to segmented scintillators is the trade-off between efficiency and obtainable spatial resolution of the

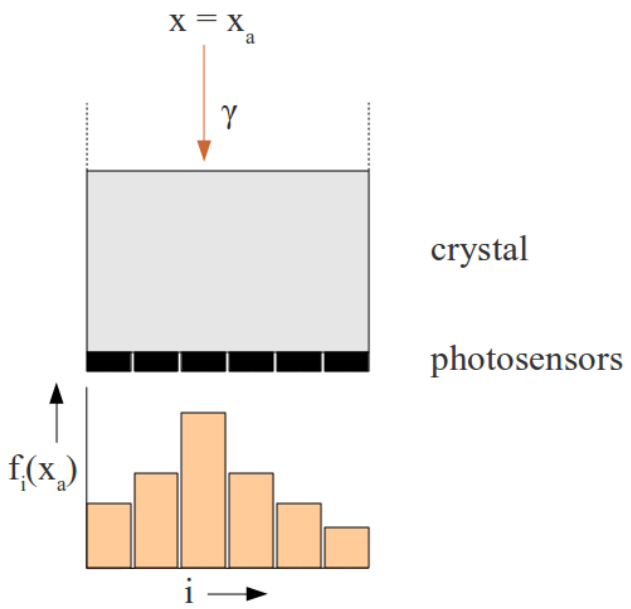

Figure 3.5: Continuous scintillation crystal, illuminated by a perpendicular beam of gamma photons at a certain position $x = x_a$. The mean response of the photosensors for this beam position $f_i(x_a)$ is indicated at the bottom.

detector. Since the scintillation light is not channeled with a low spatial spread towards the photosensor, a thicker scintillation crystal for higher sensitivity implies a larger light spread and thus a worse spatial resolution. This follows from the statistical fluctuations in the signal generation process. The following analysis is taken from [52]. Consider a continuous scintillation crystal, read out by a 1D array of photosensors and illuminated by a beam of gamma photons, impinging perpendicularly at the crystal surface (Fig. 3.5). Indicate the mean number of photoelectrons generated in the i^{th} photosensor for a beam at position x by $f_i(x)$. Assume that the fluctuations in the signal generation process are mainly introduced by the statistics of scintillation photon generation in the crystal and photoelectron generation at the photosensors, which are described by Poisson processes. The probability for generating $\{m_1, m_2, ..., m_n\}$ photoelectrons in the corresponding photosensors for a beam at position x is then given by Poisson statistics:

$$P[m_1, m_2, ..., m_n|x] = \prod_{i=1}^{n} \frac{f_i(x)^{m_i} e^{-f_i(x)}}{m_i!} \tag{3.8}$$

The other way around, given the photoelectron distribution $\{m_1, m_2, ..., m_n\}$, the probability that this distribution was generated by a beam at position x is given by the same equation. According to Maximum Likelihood Estimation (MLE), the best estimate for the beam position $\hat{x}$, given a certain distribution $\{m_1, m_2, ..., m_n\}$, is the one for which this probability is maximum:

$$\hat{x} = \arg_x max\, P[m_1, m_2, ..., m_n|x] \tag{3.9}$$

For mathematical convenience, instead of P, the logarithm of P ($\ln P$) can be maximized[4]. The maximum can be found by calculating the root of the first derivative of $\ln P$ with respect to x:

$$\frac{\partial}{\partial x} \ln P[m_1, m_2, ..., m_n|x] = \sum_{i=1}^{n} \frac{m_i}{f_i(x)} \frac{\partial f_i(x)}{\partial x} - \sum_{i=1}^{n} \frac{\partial f_i(x)}{\partial x} = 0 \tag{3.10}$$

The Cramér-Rao lower bound σ_{lb}^2 sets a lower bound on the variance of an unbiased estimator. This means that, given a certain statistical model, the best obtainable resolution for estimating a model's parameter is given by the Cramér-Rao lower bound. This is only valid for unbiased estimators, i.e. the expected value of the estimator should be the same as the true value of the parameter that is being estimated. In the current example, it can be calculated as follows:

$$\sigma_{lb}^2 = \frac{1}{I(x)} \tag{3.11}$$

where the Fisher information $I(x)$ is defined by

$$I(x) = -E\left[\frac{\partial^2}{\partial x^2} \ln P[m_1, m_2, ..., m_n|x]\right] \tag{3.12}$$

$$= \sum_{i=1}^{n} \frac{1}{f_i(x)} \left(\frac{\partial f_i(x)}{\partial x}\right)^2 \tag{3.13}$$

Here, E denotes the expected value, such that $E[m_i|x] = f_i(x)$. Eqs. 3.11 - 3.13 say that the best obtainable resolution for estimating the beam position x_a is primarily determined by the slopes $\partial f_i(x)/\partial x$ at x_a. A larger scintillation light spread induces a more uniform light distribution at the photosensor plane, thus decreasing the slopes $\partial f_i(x)/\partial x$ and worsening the best obtainable spatial resolution. From this, it follows that by increasing the thickness of monolithic scintillation crystals, the obtainable spatial resolution degrades due to an increasing light spread. In the same way, the obtainable spatial resolution for events close to the photosensor array is better than for events more distant from the photosensor array. Experimental studies of the positioning performance of monolithic scintillation crystals with varying thickness at various excitation depths are presented in chapter 5.

[4]This is justified, since $\ln P$ is a monotonically increasing function of P, meaning that $\ln P$ increases if P increases and decreases if P decreases. The maximum of $\ln P$ is thus located at the same x as the maximum of P.

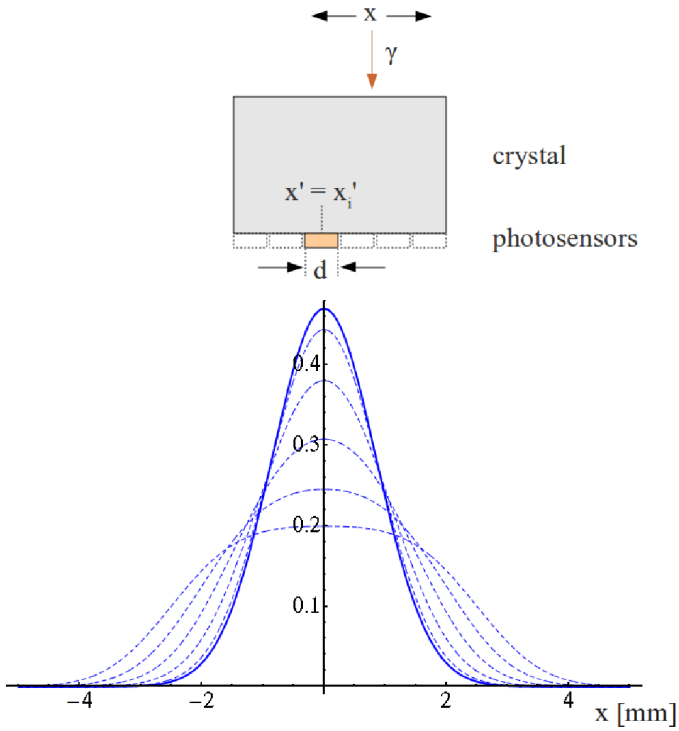

Figure 3.6: Widening of the photon distribution function LRF due to the finite pixel size. Upper figure: The LRF is evaluated for photosensor i at fixed location $x' = x'_i$ by varying the beam position x over the crystal surface. Lower figure: The LRF is indicated by the solid line and is given by Eq. 3.15, whereby $\sigma = 2/2.355$ mm and $x' = x'_i$. The dashed lines are plots of the normalized pixel response $f_i(x)/\int_{-\infty}^{+\infty} f_i(x)dx$, whereby $f_i(x)$ is given by Eq. 3.16, for pixel widths $d = \{1, 2, 3, 4, 5\}$ mm. The beam coordinate axis is centered at the photosensor location ($x = 0$ for $x' = x'_i$).

It is explicitly noted here that the distribution $\{f_1(x), f_2(x), ..., f_n(x)\}$ is a *sampled* representation of the mean light distribution function LRF at the photosensor plane for a beam at position x. Each photosensor i has a certain size and the mean number of generated photoelectrons $f_i(x)$ depends on the LRF distribution over the photosensor. Mathematically, this involves an integration of LRF over the photosensor surface [53]:

$$f_i(x) = \int_{x'_i - d/2}^{x'_i + d/2} N \cdot QE \cdot LRF(x, x')dx' \tag{3.14}$$

where N denotes the total number of scintillation photons incident on the photosensors, QE the quantum efficiency and x'_i the location of photosensor i of width d. The spatial integration of LRF over the photosensor surface widens the resulting $f_i(x)$ distribution. This can be illustrated as follows (see Fig. 3.6). Assume that the LRF is a Gaussian distribution function[5]:

$$LRF(x, x') = \frac{1}{\sqrt{2\pi\sigma^2}} e^{-\frac{(x-x')^2}{2\sigma^2}} \tag{3.15}$$

The FWHM width of a Gaussian distribution function is equal to $2\sqrt{2\ln 2} \cdot \sigma \approx 2.355 \cdot \sigma$. Using eq. 3.14, $f_i(x)$ can be calculated as follows:

$$f_i(x) = \frac{N \cdot QE}{2} \left(erf\left[\frac{x - (x'_i - d/2)}{\sqrt{2}\sigma}\right] - erf\left[\frac{x - (x'_i + d/2)}{\sqrt{2}\sigma}\right] \right) \tag{3.16}$$

where erf is the Gauss error function. The FWHM width of $f_i(x)$ in Eq. 3.16 is equal to $\sqrt{d^2 + (2.355 \cdot \sigma)^2}$. Eq. 3.16 is plotted in Fig. 3.6 for the pixel widths $d = \{1, 2, 3, 4, 5\}$ mm and LRF width of $2.355 \cdot \sigma = 2$ mm FWHM. It is apparent that the finite pixel size convolutes the light distribution function LRF, resulting in a broadened pixel response $f_i(x)$ in case the pixel size is larger than the width of the LRF. This broadening effect decreases the slope $\partial f_i(x)/\partial x$ along x and, in conjuction with Eqs. 3.11 - 3.13, deteriorates the obtainable spatial resolution. This means that the pixel width d is a primary factor in determining the obtainable spatial resolution of the monolithic scintillation detector.

More generally, the crystal readout geometry (i.e. size, number and location of the photosensors on the crystal) determines the effect of the statistics in scintillation photon generation, transport and collection on the detector spatial resolution. E.g., with the help of Eqs. 3.11 - 3.13, one can see that the obtainable spatial resolution will be improved when two photosensor arrays are placed on opposing crystal sides, as compared to one array on one crystal side. Since the distance between gamma interactions and a photosensor array is at most half the crystal length for double sided readout, the scintillation light is less spread out on one of the photosensor planes, improving the spatial resolution according to Eqs. 3.11 - 3.13.

The actual spatial resolution is worse than indicated by σ_{lb} in Eqs. 3.11 - 3.13 due to additional degrading factors besides statistics in scintillation photon collection, like position blurring introduced by multiple Compton scattering (see next section) and noise sources introduced by the photosensor (like excess multiplication noise) and associated electronics.

[5]It should be noted that in this example no attempt is made to present a realistic model of the LRF. It is only wished to illustrate the broadening effect induced by the finite pixel size. An alternative LRF function could as well have been chosen for this illustration.

3.3.2 Effect of Compton scattering within the crystal

The obtainable spatial resolution is degraded in both crystal designs by Compton scattering. In Table 3.1, one can find that the probability for a 511 keV gamma ray to undergo photoelectric absorption instead of Compton scatter during its first interaction in the crystal is less than 50 % (44 % for BGO, 34 % for LSO, 14 % for $LaBr_3$).

During Compton scattering, a significant fraction of the energy is transferred to an electron, producing scintillation photons inside the crystal, while the scattering angle can be large. From relativistic energy and momentum conservation, one can calculate that the energy of the Compton scattered gamma photon $E_{\gamma'}$ depends on the scattering angle θ, as defined in Fig. 3.7(a), in the following way [53]:

$$E_{\gamma'}(E_\gamma, \theta) = \frac{E_\gamma}{1 + \frac{E_\gamma}{m_e c^2}(1 - \cos\theta)} \tag{3.17}$$

where E_γ is the energy of the incoming gamma photon, c the light speed and m_e the electron mass (511 keV/c^2). For incident annihilation photons (E_γ = 511 keV $= m_e c^2$), this reduces to

$$E_{\gamma'}(\theta) = \frac{E_\gamma}{2 - \cos\theta} \tag{3.18}$$

The energy transferred to the electron is equal to $E_\gamma - E_{\gamma'}$. For backscatter ($\theta = 180°$), the transferred energy obtains a maximum of $E_\gamma - E_{\gamma'} = 2E_\gamma/3 \approx$ 341 keV. No energy is transferred at $\theta = 0°$. $E_\gamma - E_{\gamma'}$ is plotted in Fig. 3.7(b). The differential cross section for Compton scattering is given by the Klein-Nishina formula:

$$\frac{d\sigma}{d\Omega}(E_\gamma, \theta) = \frac{r_e^2}{2}\frac{E_{\gamma'}^2}{E_\gamma^2}\left(\frac{E_{\gamma'}}{E_\gamma} + \frac{E_\gamma}{E_{\gamma'}} - 1 + \cos^2\theta\right) \tag{3.19}$$

where r_e is the classical electron radius ($2.82 \cdot 10^{-15}$ m) and $E_{\gamma'}$ is defined according to Eq. 3.17. Eq. 3.19 gives the angular (θ) distribution of the Compton scattered gamma photon per unit solid angle Ω (steradian). The true angular distribution (per unit scattering angle θ) can be obtained by integrating Eq. 3.19 over the circumference spanned by the azimuthal coordinate φ, indicated in Fig. 3.7(a):

$$\frac{d\sigma}{d\theta}(E_\gamma, \theta) = \frac{d\sigma}{d\Omega}(E_\gamma, \theta) \cdot 2\pi \sin\theta \tag{3.20}$$

Eqs. 3.19 and 3.20 are plotted for incident 511 keV gamma photons in Figs. 3.7(c) and 3.7(d), respectively. Fig. 3.7(d) shows that the scattering angle distribution is broad, obtaining a maximum at $\theta \approx 35°$.

The scattered gamma photon can interact at a different location by a photoelectric absorption or a subsequent Compton scatter (thus creating multiple scintillation centers), or leave the crystal without further interaction. The creation of

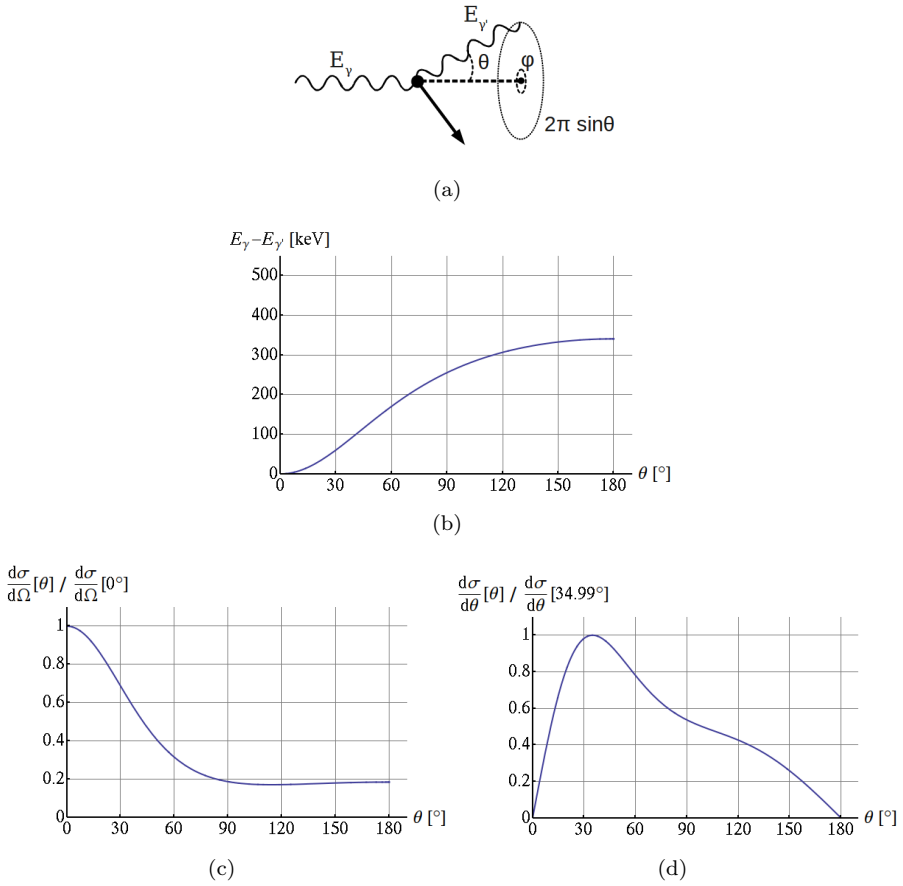

Figure 3.7: (a) Schematic view of Compton scattering. A gamma photon of energy E_γ collides with an electron at rest. A new gamma photon of energy $E_{\gamma'}$ emerges at angle θ. (b) Energy $E_\gamma - E_{\gamma'}$ transferred to the electron as a function of θ for $E_\gamma = 511$ keV. (c) Differential cross section for $E_\gamma = 511$ keV, normalized at $\theta = 0°$. (d) Cross section per unit scattering angle θ for $E_\gamma = 511$ keV, normalized at $\theta = 34.99°$.

multiple scintillation centers within the same crystal acts as a position blurring effect, because the produced LRF on the photosensor is distorted with respect to the LRF from a single interaction event (see Fig. 3.8). The thicker the crystal, the higher the fraction of events for which the full 511 keV energy was absorbed by multiple interactions. This again acts as a tradeoff between detection efficiency and obtainable spatial resolution. For events with inter-detector Compton scat-

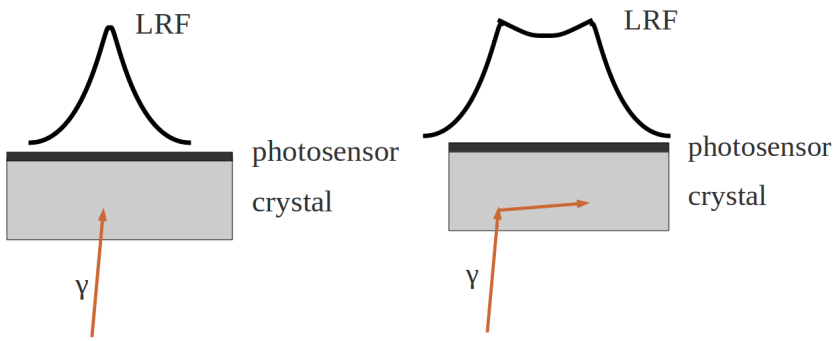

(a) LRF from single interaction (b) LRF from multiple interactions

Figure 3.8: Illustration of LRF broadening due to multiple scintillation centers in the crystals. This causes position blurring in both segmented and continuous crystal designs.

tering, the energy is shared among different detectors. These events can either be filtered out or properly reconstructed by Compton kinematics, such as in a Compton camera [54]. Compton events for which the full 511 keV energy was not absorbed by the crystal can be filtered out by energy thresholding (as occurs for events that had a Compton interaction within the examined body, section 2.2.3).

3.3.3 Designs for DOI detection

As discussed in section 2.2.3, the parallax effect is one of the most important degrading factors in PET imaging. It shows up for a gamma photon that enters the crystal from an oblique angle, while the detector does not give information about the DOI. Especially for thick crystals it is important to correct for this error, since the DOI spread is large. Enabling DOI detection in PET detectors has been one of the most active fields of research in PET imaging. This section gives an overview of some proposed scintillation detector designs with DOI detection capability.

DOI detection in segmented crystals

Position estimation in segmented crystals is based on identification of the crystal segment in which a gamma interaction took place. Since the scintillation light is channeled towards the photosensor, the LRF essentially does not vary with DOI,

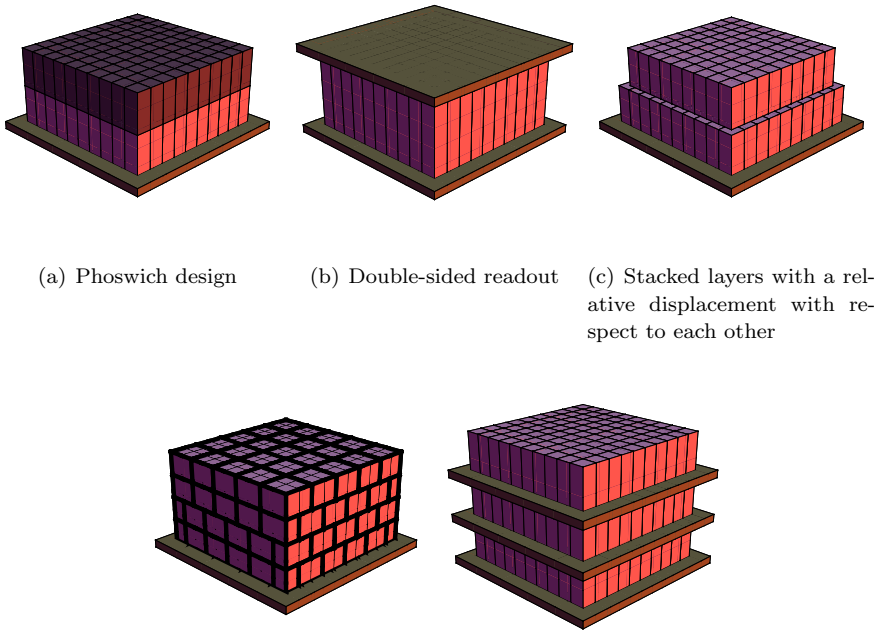

(a) Phoswich design

(b) Double-sided readout

(c) Stacked layers with a relative displacement with respect to each other

(d) Layers with reflective optical structure

(e) Multiple photosensors

Figure 3.9: Common designs for DOI detection in segmented crystals

by design[6]. Therefore, for conventional PET detectors with segmented crystals, DOI detection is not possible. Most commercial PET scanners do not offer DOI detection, and often have large detector rings while employing a small transaxial field-of-view (FOV) to reduce the parallax error (see section 2.2.3). Detector modifications are necessary to add DOI detection. Fig. 3.9 shows several segmented crystal designs that enable DOI detection.

The phoswich design is one of the oldest approaches and proposed by many groups (e.g. [55–57]). Stacked scintillators with different decay times are used. The pulse shape of the scintillation signal depends on the particular scintillator in which the interaction took place, and one can measure the pulse shape to identify the scintillator (pulse shape discrimation, PSD). Simply setting different time windows is often sufficient to discriminate the crystals. Drawbacks are the costs

[6] Although there may be variations in detected energy as a function of DOI, due to variations in light absorption.

of fabrication to assemble these crystals and possible limitations to the obtainable timing resolution, since the decay times of the scintillators need to vary sufficiently to allow for crystal discrimination and can thus necessarily not be optimized for the fastest timing.

Another approach is to attach photodetectors at both ends of the crystal segments. DOI can be determined by the ratio of the detected light at the photosensors. For this readout design, at least one of the photodetectors should be transparent to gamma photons to avoid gamma absorption. In [58], SiPMs are used at both ends of a $1.8 \times 2 \times 20$ mm^3 LYSO crystal, achieving a DOI resolution of 4.5 mm FWHM. In [59], a DOI resolution of 2 mm FWHM was achieved for an LSO crystal array with $1 \times 1 \times 20$ mm^3 segments, read out by PSAPDs at both ends. Although a good DOI resolution can be obtained by the dual-sided readout, detector costs are increased significantly due to the larger number of photosensors and readout channels. Since the detected light output per photosensor is less, the timing resolution will also be degraded in case only one of the photosensors is used for time pickoff.

Multi-layered crystals with DOI-encoding have also been built. The layers are either stacked with a small offset with respect to each other (Fig. 3.9(c)) or have a special reflector structure (Fig. 3.9(d)). The arrangement of the layers is such, that all crystal segments can be expressed on a 2D position map without overlapping. Only one position-sensitive photosensor is therefore needed to identify the crystal segments in 3D. Drawback of this method are the fabrication costs and difficulties with light collection. Due to the complex optical structure, there will be more optical reflections and associated absorption of the scintillation light, thus leading to a deterioration of the timing and energy resolution, especially for the layers far from the photosensor. In [60], four layers of $1.46 \times 1.46 \times 4.5$ mm^3 LSO crystal segments were used in a special reflector structure. The energy resolutions of the 1st and 4th layer were 11.6 % and 19.1 %, respectively. The difference in light collection efficiency for the layers also leads to profound transit time differences, thus broadening the time spectrum. In [60], a transit time difference of 150 ps was observed between the 1st and 4th layer. A DOI correction to the timing can be applied to improve the timing resolution [61].

It has been proposed to optically couple neighboring crystal segments [62]. The interface between the crystal segments is such that the amount of light sharing is varied along the DOI-direction. The DOI can be extracted from the ratio of the collected light by each crystal segment. This approach also only requires a single position-sensitive photosensor.

Various layers of thin solid-state photodetectors and crystals can also be used to identify crystal segments in 3D (Fig. 3.9(e)). In [63], $1 \times 1 \times 3$ mm^3 LSO crystal segments were coupled with their long side to extremely thin ($<300\mu$m) PSAPDs, such that a high packing fraction is achieved. With this approach, the light collec-

tion efficiency is much better compared to the other approaches. However, high costs are associated with the high density of electronic channels and photodetectors.

In conclusion, enabling DOI measurement in segmented crystals is possible, but not trivial. It involves costly detector modifications (e.g. additional photosensors and electronic channels, or complex optical structures), while other detector performance parameters (energy and timing resolution) may degrade due to reduced light collection.

DOI detection in continuous crystals

In continuous crystals the light is not confined to a crystal segment, but spreads out through the crystal volume. Due to this spreading, the minimum obtainable spatial resolution in continuous crystals is degraded (see Eqs. 3.11 - 3.13). The LRF not only varies with the 2D entrance position onto the crystal, but also with the DOI: The LRF is less spread out for photoconversion positions close to the photosensor, compared to positions far from the photosensor (see Figs. 4.11 and 8.7). Especially for thick scintillation crystals, this variation with DOI can lead to systematic errors if the positioning is based on a simple 2D centroid calculation of the LRF. The variation of the LRF with DOI can, however, also be exploited to estimate the 3D photoconversion position (thus including DOI) using more advanced position algorithms. In contrast to segmented crystals, continuous crystals thus inherently provide information about the DOI. The expensive and complex optical modifications of the crystal mentioned in section 3.3.3, which often deteriorate the light collection efficiency, are therefore not needed. Continuous crystals already had the cost advantage with respect to segmented crystals (section 3.3.1). The ability to estimate the DOI with a single photosensor array without crystal modifications makes them even more cost effective for PET detectors with DOI detection capability. The central question is how thick the crystals can be made for optimal efficiency, such that accurate positioning is still possible (Eqs. 3.11 - 3.13). For thick scintillation crystals, this may require a double-sided readout.

For single-sided readout, the LRF as a function of 3D position needs to be known. This information can be achieved from a detector calibration with a pencil beam of gamma photons, or from a theoretical model of the detector response function. In general, statistical methods (e.g., maximum likelihood estimation (MLE) [50, 64, 65] and in this work in chapter 4, neural networks [66] or nearest neighbors [37]) are used for 3D position estimation. Detectors based on continuous crystals that use a single photosensor array to estimate the 3D position are described in [49, 50, 64, 67–69] and in this work (chapter 4). It is also possible to calibrate the detector on the entry point of the gamma ray on the front surface of the crystal, such that DOI is intrinsically corrected for, although this requires a

detector calibration at various incident angles [37].

3.4 Alternative radiation detectors

Scintillation detectors still dominate in PET imaging. Some (prototype) scanners have also been built from alternative detectors, generally with the goal to achieve very high sub-millimeter spatial resolution, primarily for pre-clinical small animal imaging. The following sections describe alternative detectors, from which (prototype) scanners have or have not (yet) been built.

3.4.1 Semiconductor detectors

Semiconductor detectors are the most important alternative radiation detectors besides scintillation detectors. In these detectors an incident ionizing particle produces a large number of charge carriers along its trajectory, electron-hole pairs, that are collected at electrodes by applying an electric field. The fundamental working principle is thereby similar to the conventional photodiode, discussed in section 3.2. Silicon (Si) and germanium (Ge) are the most commonly used semiconductor detector materials. Cadmium telluride (CdTe) and cadmium zinc telluride (CdZnTe, or CZT) are more recent materials.

The conversion of the radiation energy into carriers is much more efficient than the conversion into scintillation light in scintillation detectors, which takes multiple inefficient conversion steps. In scintillation detectors, only a few thousand primary photoelectrons are created by the scintillation light in the photodetector. The statistical fluctuation is therefore relatively large and this inherently limits the maximum obtainable energy resolution. In semiconductor detectors a much larger number of carriers are produced, such that one generally obtains a better energy resolution for these detectors. An energy resolution less than 2 % at 511 keV can be achieved with CdTe and CdZnTe (CZT) detectors [10]. This allows a much narrower energy window to be set compared to scintillation detectors, thus rejecting more gamma photons that scattered within the body.

Another advantage is the ability to design compact 3D pixel arrays in fine arrangement, whereby the individual pixels are in mm-scale. This allows sub-millimeter spatial resolution and 3D localization of the gamma photon interaction point, thus including DOI, without dead space between the pixels [70, 71]. Due to the high spatial resolution, high energy resolution and pixelated design, it is further possible to recover scattered events by Compton kinematics [72]. In this way the point of first interaction can be determined, such that position blurring due to multiple scatter is not an issue.

However, there are also a number of disadvantages with these detectors. Both Si and Ge have a high thermally generated dark current at room temperature,

such that these materials need to be cooled in order to reduce this background noise source. Another problem in semiconductor detectors is the presence of impurities which trap the charge carriers during ionization events, and thus lower the signal, and limit the detector thickness to about 1 cm [12]. This problem may be solved by preparing high purity samples of detector material, like high purity germanium (HPGe, a standard technique for about 25 years), which is an expensive operation, however. Semiconductor detectors further have a significantly lower detection efficiency and an inferior timing performance due to long collection times, compared to PET-relevant scintillation detectors. The cost is also higher for the basic materials and front-end multichannel electronics. The recent semiconductor materials CdTe and CZT partly overcome these problems, as they can be operated at room temperature without excessive noise and have a relatively high stopping power due to their high density and atomic number (ρ equal to 6.06 g/cm^3, Z equal to 48 and 52 for Cd and Te, respectively). However, the efficiency for CZT is still 3 times lower than for LSO scintillators and also the timing performance is still inferior, requiring a large coincidence time window with an associated large background of random coincidences [73]. Further, the purity problem still restricts the size of these detector materials and only permits a planar design. Although the pixelated design requires the individual detector elements to be small for high spatial resolution, one readout channel for every pixel implies a high cost.

Due to the unfavorable properties with respect to timing and efficiency, these detectors are currently not suited for whole-body imaging. However, their superior spatial resolution is interesting for small animal and brain imaging. An animal PET scanner based on the CdTe semiconductor detector has already been built [70]. A prototype brain 3D PET scanner using CdTe detectors was shown to be feasible for clinical use with high spatial resolution, DOI reconstruction and good energy resolution [74]. Clinical images of this scanner and of a conventional PET scanner based on BGO scintillators were compared, and it was concluded that the higher spatial and energy resolution of the CdTe scanner resulted in a better tumor identification [75].

3.4.2 Gaseous ionization detectors

A few PET detectors based on gaseous ionization detectors exist, such as multi-wire proportional chambers (MWPCs) [76, 77] and resistive plate chambers (RPCs) [78]. These devices are generally more complex to fabricate into a scanner than scintillation and semiconductor detectors [42]. In these detectors, gamma photons interact in metal conversion layers, such as lead layers with a matrix of small holes in the MWPC-based HIDAC camera [79] or metallic electrodes in RPCs [78]. The resulting electrons will ionize gas chambers and initiate avalanches of electrons that are collected by an electric field between electrodes. There is virtually no

energy resolution [42] due to the high ionization energy[7], such that a small number of electrons are produced. Compton scattered events can thus not be filtered out. However, the construction of RPC detectors is inexpensive such that a large fraction of the total solid angle can be covered, therefore still leading to a high system sensitivity [78]. In addition, these detectors exhibit an excellent timing resolution of 300 ps FWHM for 511 keV gamma photons [80], sub-millimeter spatial resolution and DOI reconstruction capability due to detector stacking in the DOI-direction. MWPC detectors also provide sub-millimeter resolution, but have inferior performance with respect to detection efficiency, count rate performance and timing resolution [10].

3.4.3 Liquid xenon detectors

Liquid Xenon (LXe) detects gamma photons by emitting scintillation light and producing electron-ion pairs by ionization [81]. It has a reasonable stopping power (density 3.06 g/cm^3, comparable to NaI, but much lower than LSO and BGO), good ionization and scintillation yields (scintillation light yield 46,000 photons/MeV) and fast timing (scintillation decay components of 2 and 27 ns, [10]). The charge can be measured in a drift chamber and provides 3D sub-millimeter resolution (due to small electron diffusion), while the scintillation light provides sub-nanosecond timing resolution. The combination of both signals leads to an energy resolution below 10 % FWHM [82].

3.5 PET detector concept in the current work

In the current work a TOF-PET detector concept is investigated based on a monolithic (continuous) scintillation crystal and fast solid-state photosensors (SiPMs). The advantages of monolithic scintillation crystals (high gamma detection efficiency due to absence of dead space; high scintillation light collection efficiency; intrinsic DOI detection capability; no costs involved with crystal segmentation, see section 3.3.1) and SiPMs (high gain; fast response; MR compatibility; compactness; flexible readout geometries; low costs, see section 3.2.2) carry the prospect of fast, low-cost, MR-compatible TOF-PET detectors with DOI measurement. Since the scintillation light is not channeled towards the photosensor with low spatial spread (see section 3.3.1), an important question is whether a good positioning performance can be obtained for thick (efficient) monolithic scintillation crystals. This may require double-sided readout and thus an increase in detector costs. LYSO and $LaBr_3$ crystals are chosen as scintillation materials, due to their favorable timing properties (see Table 3.1).

[7] Ionization energy of gas is around 30 eV, while this is around 3 eV for semiconductors.

Chapter 4 presents a calibration method and a positioning algorithm based on MLE for reconstructing the 3D interaction position (thus including DOI) inside the monolithic scintillation crystal. In chapter 5, the positioning performance of monolithic scintillation crystals of varying thickness, coupled to a single MAPMT, is tested using the MLE method described in chapter 4. The timing performance of SiPM sensors (in particular their single photoelectron timing resolution) is presented in chapter 6. Timing measurements of single SiPM sensors coupled to small $LaBr_3$:Ce crystals are presented in chapter 7. Chapter 8 presents positioning and timing measurements for monolithic $LaBr_3$ crystals coupled to a single SiPM array, as well as ultrafast timing measurements for small $LaBr_3$ crystals coupled to single SiPMs.

4 Time walk correction for TOF-PET detectors based on a monolithic scintillation crystal coupled to a photosensor array

This chapter has been published as: R. Vinke, H. Löhner, D. Schaart, H. van Dam, S. Seifert, F. Beekman, and P. Dendooven, "Time walk correction for TOF-PET detectors based on a monolithic scintillation crystal coupled to a photosensor array," Nucl. Instr. Meth. A, vol. 621, pp. 595-604, 2010.

Abstract

When optimizing the timing performance of a time-of-flight positron emission tomography (TOF-PET) detector based on a monolithic scintillation crystal coupled to a photosensor array, time walk as a function of annihilation photon interaction location inside the crystal needs to be considered. In order to determine the 3D spatial coordinates of the annihilation photon interaction location, a maximum likelihood estimation algorithm was developed, based on a detector characterization by a scan of a 511 keV photon beam across the front and one of the side surfaces of the crystal. The time walk effect was investigated using a 20 mm × 20 mm × 12 mm LYSO crystal coupled to a fast 4×4 multi-anode photomultiplier tube (MAPMT). In the plane parallel to the photosensor array, a spatial resolution of 2.4 mm FWHM is obtained. In the direction perpendicular to the MAPMT (depth-of-interaction, DOI), the resolution ranges from 2.3 mm FWHM near the MAPMT to 4 mm FWHM at a distance of 10 mm. These resolutions are uncorrected for the ∼1 mm beam diameter. A coincidence timing resolution of 358 ps FWHM is obtained in coincidence with a BaF_2 detector. A time walk depending on the 3D annihilation photon interaction location is observed. Throughout the crystal, the time walk spans a range of 100 ps. Calibration of the time walk vs. interaction location allows an event-by-event correction of the time walk.

4.1 Introduction

Positron emission tomography (PET) detectors based on a monolithic scintillation crystal coupled to a photosensor array have the potential to increase PET system sensitivity compared to block detectors consisting of pixelated crystals [48, 83]. Additionally, it has been shown that statistics-based positioning algorithms give

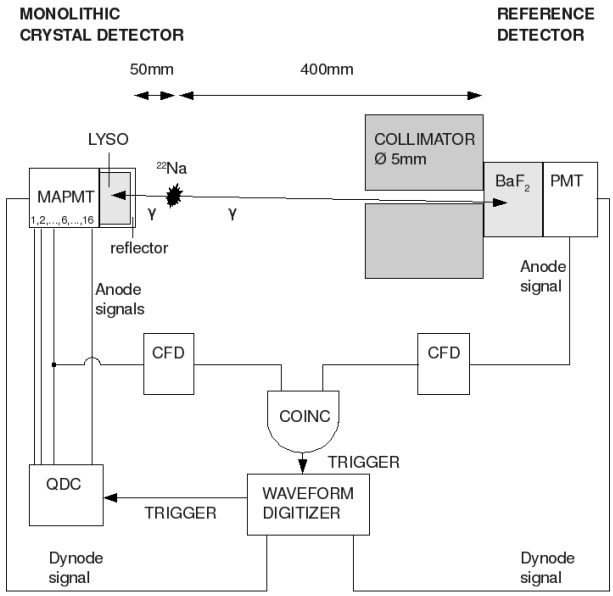

Figure 4.1: Schematic view of the experimental setup.

excellent intrinsic spatial resolution for detectors based on these monolithic scintillation crystals [37, 65, 84–86], with depth-of-interaction (DOI) reconstruction capability [49].

It is well known that including time-of-flight (TOF) information in the image reconstruction process can significantly reduce the noise variance in the image [6, 8], thereby effectively increasing the PET system sensitivity. In the optimization of the timing performance of a TOF-PET detector based on a monolithic scintillation crystal coupled to a photosensor array, time walk as a function of annihilation photon interaction location inside the crystal needs to be considered. This study focuses on this effect. In order to determine the 3D spatial coordinates of the annihilation photon interaction location, a maximum likelihood estimation algorithm was developed. The timing performance was studied in a coincidence setup with a BaF_2 detector, using digital time pickoff techniques on the timing signals. The time walk as function of the 3D position-of-interaction is then deduced and an event-by-event correction can be applied.

4.2 Materials and methods

4.2.1 Experimental setup

A schematic view of the setup is shown in Fig. 4.1. A monolithic polished LYSO crystal with dimensions 20 mm × 20 mm × 12 mm was coupled to a Hamamatsu position-sensitive H8711-03 4×4 multi-anode photomultiplier (MAPMT) using Sylgard® 527 dielectric gel as coupling material [87]. The MAPMT anode sizes are 4.2 mm × 4.2 mm and the center-to-center spacing is 4.5 mm. The crystal sides not facing the MAPMT were covered with a reflective PTFE based material (Spectralon® [88]) to maximize the light collection efficiency. The last dynode signal of the MAPMT contains the light intensity collected by each individual channel. This signal therefore served as the 'timing signal' for the monolithic crystal detector. A ^{22}Na source provided 511 keV positron annihilation photon pairs. A fast BaF_2 detector was used as a reference detector. This detector (Scionix model 25.4 B 20 / 2Q-BAF-X-NEG + VD29-124KT) consists of a 20 mm thick, 25.4 mm diameter crystal mounted on an XP2020Q photomultiplier tube and has a timing resolution for 511 keV photons of about 180 ps. The dynode (timing) signals of both detectors were sent to an Agilent DC282 waveform digitizer. No amplifiers were used. Timing traces were digitized at 2 GS/s (500 ps/pt) for both detectors at 2 GHz bandwidth. The MAPMT anode signals (the 'energy signals') were sent directly to a LeCroy 4300B 16-channel charge integrating ADC (QDC), interfaced to a CAMAC system. For deriving the coincidence trigger, one of the center anode signals of the MAPMT (anode #6) was split and one branch sent to a constant fraction discriminator (CFD). The anode output of the BaF_2 PMT was sent to a second CFD. The two CFD outputs were sent to a logic coincidence unit and the resulting output served as the trigger signal for the waveform digitizer.

The systems acquiring the energy and timing signals (the QDC and waveform digitizer, respectively) were synchronized in order to be able to combine the energy and timing information for each event. This was done by operating the CAMAC system in 'slave'-mode: charge pulses were digitized only after a trigger was received from the waveform digitizer. A separate event counter was installed in the CAMAC system to count the number of triggers sent out by the waveform digitizer. In this way, events that were rejected by the QDC because they occurred during a 'dead time'-state could be tracked afterwards. Synchronization could be confirmed after acquisition by cross-correlating the energy of the MAPMT dynode pulse, as obtained from the waveform digitizer, with the sum of the MAPMT anode channels, as recorded by the CAMAC system. The synchronization of the waveform digitizer and CAMAC system leads to each event consisting of 2 digitized dynode pulses and the energies detected by the 16 anodes of the MAPMT.

To be able to reconstruct the 3D position-of-interaction of the gamma pho-

tons in the monolithic scintillation crystal (see section 4.1), the detector response had to be calibrated as a function of gamma beam position. To obtain a beam with small spot size on the monolithic crystal, the ^{22}Na source was placed close to the monolithic crystal surface (50 mm). The reference detector was placed at a distance of 400 mm to the ^{22}Na source at the opposite side. By only taking coincidence events into account, the beam is electronically collimated at the monolithic crystal detector. The spot size of the gamma photon beam was 5 mm in diameter at the crystal surface of the reference detector (a 50 mm thick lead collimator with a 5 mm diameter hole was used for this purpose), resulting in a spot size of ∼1 mm in diameter at the monolithic crystal surface whenever both photons of the annihilation pair were detected. Two perpendicular motorized translation stages allowed scanning the monolithic crystal in the plane perpendicular to the beam and obtain a position calibration set. A calibration scan of the front surface (XY-scan) was made. After this, the detector was turned by 90 degrees and a calibration scan of one of the side surfaces (YZ-scan) was made. By combining the calibration information from these two directions, a 3D calibration set was obtained. This 3D calibration set was then used to estimate the 3D position-of-interaction of the gamma photons inside the crystal by Maximum Likelihood Estimation (MLE). Details are given in sections 4.2.3 to 4.2.6. For the position analysis, only 511 keV photopeak events were taken into account for the monolithic crystal detector, using an energy window of 450-570 keV.

4.2.2 Time pickoff procedure

Fig. 4.2 shows typical 511 keV dynode signals for both detectors. The 10-90% risetime was ∼5.3 ns for the LYSO-MAPMT dynode signal and ∼2.1 ns for the BaF_2 dynode signal.

In all timing-related analysis, the 511 keV full-energy peak was selected in both detectors. Specifically, an energy window of 450-570 keV and 380-660 keV was applied for the LYSO and BaF_2 events, respectively. This corresponded to 67% of the coincidence events for LYSO and 42% of the coincidence events for BaF_2. Taken together, the timing analysis included 28% of all coincidence events.

As time pickoff procedure, a digitalized constant fraction (dCF) procedure was used [18]: First, the detector signal was recovered from the sampled waveform by full cubic spline interpolation. Next, a delayed waveform and an attenuated and inverted waveform were created from the interpolated input waveform. The two waveforms were added to form the bipolar dCF signal. Fig. 4.2 shows typical bipolar dCF signals. The arrival time was determined as the zero-crossing time of the bipolar dCF signal. For the LYSO-MAPMT dynode signal, a delay of 15 ns and an attenuation factor of 0.06 were chosen. For the BaF_2 dynode signal, 3 ns was chosen as delay and 0.18 as attenuation factor. These parameter values gave

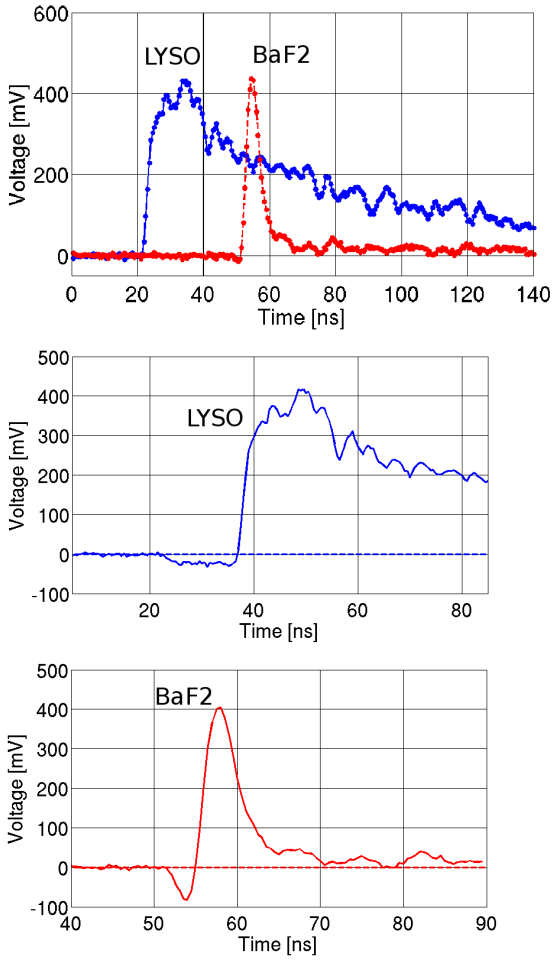

Figure 4.2: Upper graph: Typical 511 keV LYSO-MAPMT (solid blue line) and BaF_2 (dashed red line) dynode signals. The dots indicate the digitizer sampled points. Lower graphs: Bipolar dCF signals for which the zero-crossing moment defines the pulse time. Middle graph: LYSO-MAPMT dCF signal. Lower graph: BaF_2 dCF signal.

the optimal coincidence timing resolution. The coincidence timing resolution is deduced from the spectrum of the time differences between the LYSO and BaF_2 signals.

4.2.3 Calibration scans

In the following sections, the x- and y-coordinates define the coordinates parallel to the MAPMT plane and range between 0 mm and 20 mm. The center of the detector is thus located at $(x, y) = (10, 10)$. The z-coordinate defines the coordinate perpendicular to the MAPMT plane and ranges between 0 mm and 12 mm and corresponds to the DOI. The MAPMT plane is located at z = 12 mm.

Scans of the monolithic crystal were performed with the gamma beam impinging perpendicularly on the 20 mm × 20 mm front face (XY-scan) and on one of the 20 mm × 12 mm side faces (YZ-scan). Both scans were performed with a 2 mm grid spacing. For every beam position 10,000 coincidence events were collected. After selecting the full-energy events for the monolithic crystal detector, ∼6,700 events remained per beam position (see section 4.2.2). The YZ-scan provides the detector response at defined z-positions and thus allows the estimation of the DOI for the events in the XY-scan. By combining the information from the XY- and YZ-scans, the x-, y- and z-coordinate of the photoconversion position in the crystal can be estimated for any event. The used algorithms are described in sections 4.2.4, 4.2.5 and 4.2.6.

Because of the exponential attenuation law, the positions of the photon interactions are not uniformly distributed over the crystal. The annihilation photon flux decreases exponentially as a function of DOI (for LYSO the radiation length is 11.6 mm). This implies that the calibration sets contain more events at small DOI than events at large DOI. Specifically, the XY-scan contains more events at small z-coordinates ($z < 6$) than events at large z-coordinates ($z > 6$). Likewise, the YZ-scan contains more events at small x-coordinates ($x < 10$) than events at large x-coordinates ($x > 10$).

4.2.4 2D-calibration of the XY-scan

For each event, the photon distribution pattern $\{m_1, m_2, \ldots, m_{16}\}$ was calculated by normalizing the MAPMT detected energies e_i by the total detected energy as follows:

$$m_i = e_i / \sum_{j=1}^{16} e_j \tag{4.1}$$

here i is the MAPMT anode index. The probability density function of m_i for a certain anode and for a certain beam position is an anode response function (RF). The XY-scan of 11 × 11 grid points thus gives 1936 response functions. Each of these is least square fitted with a Gaussian with a high-energy exponential tail:

$$RF_i[m_i|x,y] = \begin{cases} N \cdot exp\left[-\frac{(m_i-\mu_i)^2}{2\sigma_i^2}\right] & m_i \leqslant (\mu_i+\Delta_i) \\ N \cdot exp\left[\frac{-\Delta_i \cdot (m_i-\mu_i-\Delta_i/2)}{\sigma_i^2}\right] & \text{otherwise} \end{cases} \tag{4.2}$$

where N is the normalization constant:

$$N = \frac{1}{\sqrt{\pi/2} \cdot \sigma_i \cdot \left(1 + erf\left[\frac{\Delta_i}{\sqrt{2}\sigma_i}\right]\right) + \frac{\sigma_i^2}{\Delta_i} \cdot exp\left[-\frac{\Delta_i^2}{2\sigma_i^2}\right]} \tag{4.3}$$

with erf the Gauss error function. Thus, for each anode (i) and beam position (x,y), the response function is described by three parameters:

- centroid: $\mu_i(x,y)$
- width: $\sigma_i(x,y)$
- start of tail with respect to centroid: $\Delta_i(x,y)$ ($\Delta_i > 0$).

The exponential tail shows up for anodes in line with the gamma beam and results from photoconversion locations near the MAPMT. For these locations a relatively large fraction of scintillation photons accumulates in the nearby anode, resulting in a large value for m_i for the particular anode.

For purely Gaussian functions, the tail parameter attains an asymptotic value: $\Delta_i \to \infty$. To obtain an alternative to this parameter with a limited value range, another variable was introduced in the model: the fraction $f_i(x,y)$ of the peak amplitude of the distribution at which the tail starts; by definition its range is between 0 and 1. Δ_i is related to f_i as follows:

$$\Delta_i = \sigma_i \sqrt{-2 \cdot ln[f_i]} \tag{4.4}$$

Fig. 4.3 shows an example of a fitted response function with exponential tail.

The values of $\mu_i(x,y)$, $\sigma_i(x,y)$ and $f_i(x,y)$ (as function of beam position and anode index) were stored for further processing in the MLE position estimation. To obtain the parameter values on a fine grid with 0.5 mm spacing (as opposed to the 2 mm grid of the calibration scan), a bicubic spline interpolation was applied. As an example, Fig. 4.4 shows the centroid distribution for one of the central anodes as a function of beam position.

Given a certain beam position (x,y), the probability for observing the photon distribution pattern $\{m_1, m_2, ..., m_{16}\}$ is given by the product of the individual

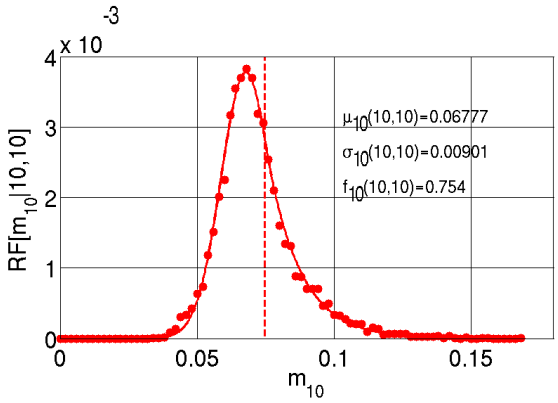

Figure 4.3: Fitted response function from the XY-scan for anode #10 and xy-beam position in the center of the crystal: (x,y)= (10,10). The dotted vertical line respresents the transition from the Gaussian to exponential regime. The values of the fitted parameters $\mu_i(x,y)$, $\sigma_i(x,y)$ and $f_i(x,y)$ are given.

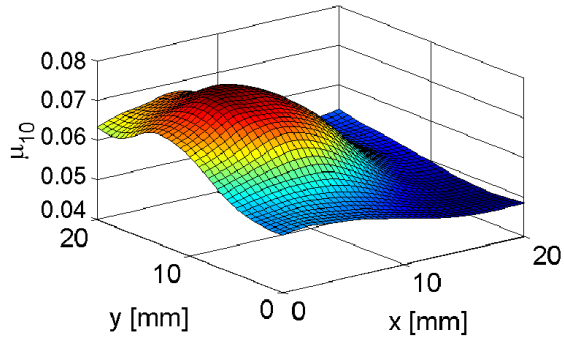

Figure 4.4: Centroid distribution for anode #10, $\mu_{10}(x,y)$, as function of beam position on a 0.5 mm grid.

normalized response functions:

$$P[m_1, m_2, ..., m_{16}|x,y] = \prod_{i=1}^{16} RF_i[m_i|x,y] \tag{4.5}$$

The other way around, given a certain pattern $\{m_1, m_2, ..., m_{16}\}$, the probability that the pattern was generated by a beam at position (x,y) is given by the same equation. In the MLE-approach, the estimate of beam position, $(\hat{x},\hat{y})$, for a certain pattern $\{m_1, m_2, ..., m_{16}\}$ is the one that maximizes this probability:

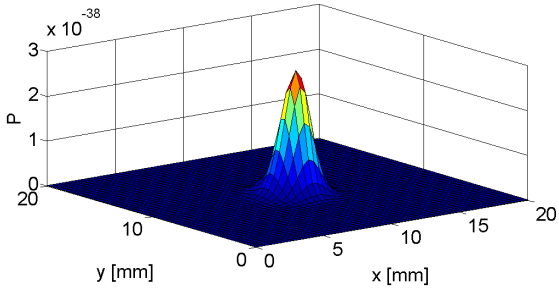

Figure 4.5: Distribution of $P[m_1, m_2, ..., m_{16}|x, y]$ in the xy-plane for a certain event.

$$(\hat{x}, \hat{y}) = \arg_{x,y} max\ P[m_1, m_2, ..., m_{16}|x, y] \tag{4.6}$$

It is noteworthy to explicitly mention here that with this MLE-approach no prior knowledge on the scintillation photon distribution patterns $\{m_1, m_2, ..., m_{16}\}$ is used during the estimation of the position-of-interaction. Additionally, no assumption is made about the variance of the normalized detected anode energy m_i. This variance is captured by the σ_i parameter in eq. 4.2 and is thus independently calibrated for each anode as a function of beam position. Determined from experiment, this σ_i parameter inherently contains all variance contributions, such as varying number of generated photons per scintillation event, PMT gain variance, electronic noise, etc. Likewise, the systematic variation of m_i with DOI is captured by the tail parameter f_i and is thus also determined from experiment. The MLE-estimation in eq. 4.6 calculates the probability of a beam position for a certain event using the calibration information on signal variance and DOI dependence, along with the calibrated information on the average signal.

Fig. 4.5 shows the distribution of $P[m_1, m_2, ..., m_{16}|x, y]$ for a certain event. The peak value can clearly be localized. For each event, the maximum of the probability distribution was searched on a 0.5 mm grid and the x- and y-position corresponding to this maximum were taken as the estimated x- and y-position of the photoconversion inside the crystal.

4.2.5 3D-calibration of the YZ-scan

The calibration method that was used for the XY-scan could not directly be used for the YZ-scan. It was found that anode response functions for which the gamma beam passes close to the MAPMT are heavily distorted from a Gaussian-like shape, making a parametrization of the response function inconvenient. The reason is that

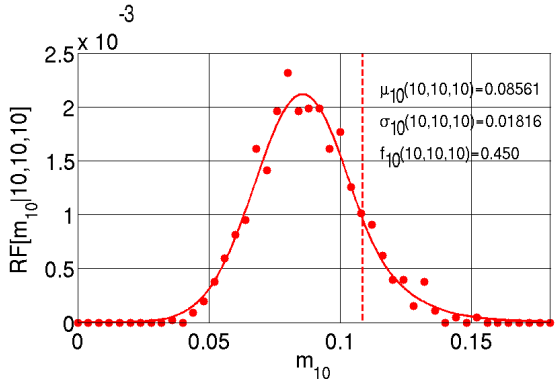

Figure 4.6: Fitted response function from the YZ-scan for anode #10, yz-beam position (y,z) = (10,10), and for which the gamma photons interacted in the x-position range $9 \leqslant x \leqslant 11$. The dotted vertical line respresents the transition from the Gaussian to exponential regime. The values of the fitted parameters $\mu_i(x, y, z)$, $\sigma_i(x, y, z)$ and $f_i(x, y, z)$ are given.

the data set for a certain (y,z) position of the gamma beam contains interactions for which the photoconversion x-position covers the whole 20 mm width of the crystal. For a particular anode, this results in a large signal when the photoconversion x-position is close to the anode and a small signal when this position is far away from the anode.

To remedy this, the photoconversion x-position was estimated for each YZ-event using the method described in section 4.2.4. A 3D-calibration set was built based on the estimated x-position and the beam-defined y- and z-position. Thus a separate response function was constructed for each of the 16 anodes, each of the 11×7 (y,z) grid positions of the incoming gamma beam and each of the (chosen) 10 bins of 2 mm width in the x-direction, giving a total of 12,320 response functions. For these response functions, the Gaussian with exponential tail appeared to be a reasonable model and the procedure detailed in section 4.2.4 to determine the three parameters $\mu_i(x, y, z)$, $\sigma_i(x, y, z)$ and $f_i(x, y, z)$ was performed. An example of a response function is shown in Fig. 4.6. Here the photoconversion position was chosen near the MAPMT: (x,y,z) = (10,10,10) (the MAPMT is located at z=12). Note the higher centroid value compared to the one in Fig. 4.3 with (x, y) = (10,10) for which the z-coordinate covered the full thickness of the crystal. This is evidently caused by a larger scintillation photon flux at the anode location due to the nearby photoconversion position.

To obtain the parameter values on a fine 3D-grid with 0.5 mm spacing, a tricubic spline interpolation was applied. For an event, the 3D-photoconversion

position could now be estimated using a 3D-version of the MLE estimation method:

$$(\hat{x}, \hat{y}, \hat{z}) = \arg_{x,y,z} max\ P[m_1, m_2, ..., m_{16}|x, y, z] \tag{4.7}$$

4.2.6 3D-calibration of the XY-scan

When building a 3D-calibration set according to the method in the previous section, the set will be built from events in the YZ-scan. The 2D-calibration set in section 4.2.4 is built from events in the XY-scan. In order to be able to make a direct comparison in x- and y-position reconstruction performance between a 2D-MLE and 3D-MLE set, it is desirable that the 3D-calibration set is also built from events in the XY-scan. In this way, in case a performance difference is observed, one can exclude the possibility that this is caused by differences in the distribution of photoconversion positions in the XY- and YZ-calibration set. (The position of the photon interaction is not uniformly distributed over the crystal, see section 4.2.3). When both the 2D-MLE and 3D-MLE calibration sets are based on events from the XY-scan, the calibrated information density as function of position (i.e. number of photoconversion interactions as function of position) is exactly the same for both sets. In order to obtain a 3D-calibration set from events in the XY-scan, the photoconversion z-position was estimated for each XY-event using the method described in section 4.2.5. Specifically, the 3D-calibration set built from YZ-events was used to estimate the photoconversion z-position, by searching the maximum probability on the 3D-grid in eq. 4.7. A new 3D-calibration set was built based on the estimated z-position and the beam-defined x- and y-position. A separate response function was constructed for each of the 16 anodes, each of the 11 $\times$ 11 (x,y) grid positions of the incoming gamma beam and each of the (chosen) 6 bins of 2 mm width in the z-direction, giving a total of 11,616 response functions. For the remainder of the calibration procedure and the MLE estimation method, the same procedure was followed as outlined in section 4.2.5.

4.2.7 MAPMT response characterization

As the characterization of the time walk as a function of scintillation location is a central theme in this paper, it is important to characterize the response of the MAPMT. Differences in transit time, quantum efficiency or gain of the MAPMT anodes would directly affect the time walk measurements. For this purpose, the MAPMT was directly excited by picosecond laser pulses (using a Hamamatsu PLP-10 light pulser) with 405 nm wavelength and 70 ps pulse width. Each MAPMT anode was separately illuminated, covering the other 15 anodes with black tape and ensuring that each illuminated anode had the same position with respect to the laser beam. No attenuation filter was used, to ensure that for each light pulse

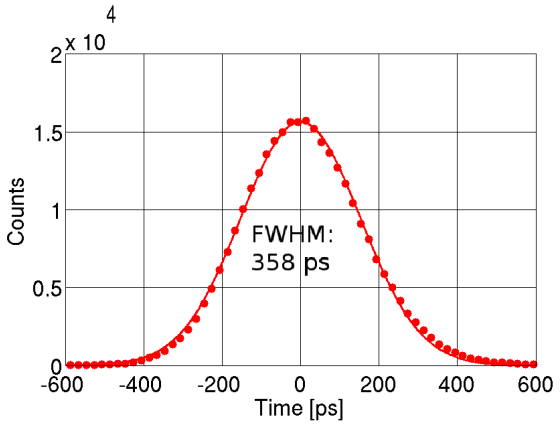

Figure 4.7: Time difference spectrum (LYSO minus BaF_2 arrival time) for events from the XY-scan. The centroid is set at 0.

a large number of light photons were detected in order to minimize the MAPMT transit time spread for an individual anode. (The transit time spread is inversely proportional to the square root of the number of detected photoelectrons [32]). For each anode measurement, digital time pickoff was performed on the dynode signal and the picosecond laser trigger pulse. The time differences were histogrammed and fitted with a Gaussian. The centroids of the time difference spectra were recorded and served as a measure for the relative transit time differences among the anodes. In addition, the energies of the dynode signals were determined by a digital summing operation along the time-axis. The dynode energies were also histogrammed and fitted with a Gaussian. The centroids of the energy histograms served as a measure for the combined effect of anode quantum efficiency and gain.

4.3 Results and discussion

4.3.1 Coincidence timing

Fig. 4.7 shows the time difference spectrum (LYSO minus BaF_2 arrival time) for events from the XY-scan constructed as described in section 4.2.2. A coincidence timing resolution of 358 $\pm$ 0.5 ps FWHM is obtained. The coincidence timing resolutions for the central and middle region (region 1 and 2 in Fig. 4.13) are both equal to 354 ps FWHM. At the crystal edges (region 3 in Fig. 4.13) the coincidence timing resolution is somewhat worse: 360 ps FWHM.

Subtracting the contribution from the BaF_2 detector (about 180 ps FWHM) gives a single detector timing resolution of the LYSO detector of about 309 ps

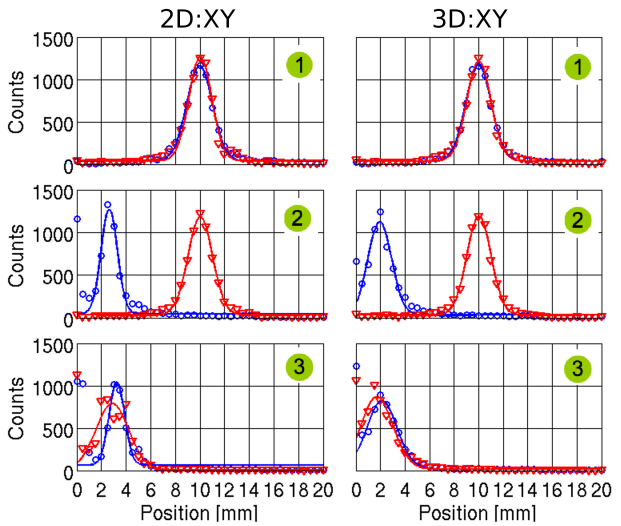

2D:XY			
Beam mark	Beam pos (x,y) [mm]	Centroid (x,y) [mm]	FWHM (x,y) [mm]
1	(10,10)	10.0, 10.0	2.4, 2.2
2	(2,10)	2.6, 10.0	1.6, 2.3
3	(2,2)	3.3, 2.9	1.5, 3.2

3D:XY			
Beam mark	Beam pos (x,y) [mm]	Centroid (x,y) [mm]	FWHM (x,y) [mm]
1	(10,10)	10.0, 10.0	2.4, 2.3
2	(2,10)	1.9, 10.0	2.3, 2.3
3	(2,2)	2.1, 1.7	2.9, 3.1

Figure 4.8: Reconstructed x-profiles (blue circles) and y-profiles (red triangles) for 3 beam positions in the XY-scan: (x,y) = (10,10); (2,10); (2,2). 2D:XY indicates the 2D-MLE procedure described in section 4.2.4; 3D:XY indicates the 3D-MLE procedure in section 4.2.6. The values of the centroid and FWHM of the reconstructed position distribution are obtained from a least-square fit with a Gaussian plus constant background (blue(x) and red(y) solid curves).

FWHM (and a corresponding coincidence timing resolution for two such detectors of about 438 ps FWHM).

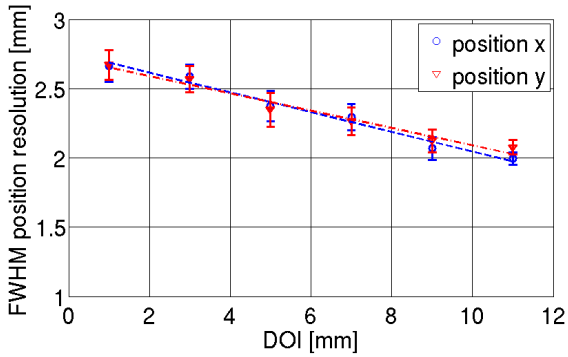

Figure 4.9: FWHM position resolution of the 3D-MLE reconstruction as function of DOI for xy-beam positions in the central 10 mm × 10 mm square of the crystal. The error bars indicate the 95%-confidence bounds for the FWHM resolution, as obtained from a least-square fit with a Gaussian plus constant background. The lines show the result of a linear fit. The MAPMT is located at z = 12mm.

4.3.2 xy-estimation

Fig. 4.8 shows the results of the xy-reconstruction for three beam positions in the XY-scan as determined using the 2D-MLE and 3D-MLE procedures outlined in section 4.2.4 and 4.2.6. In the center of the crystal the two estimation procedures have similar performance and a FWHM resolution of ∼2.4 mm is obtained. At the crystal edges a non-linearity can be observed for the response of the 2D-MLE procedure: the centroid of the reconstructed positions is shifted with respect to the true beam position. Because this does not (or to a far lesser extent) show up for the 3D-MLE response, the effect can evidently be explained by the inability of the 2D-MLE procedure to handle events near the edge of the crystal for which the photoconversion z-position (or DOI) covers the whole range of the crystal. At the crystal edges a large fraction of the events have estimated position values in the last bin of the position grid for both procedures. This can be explained by the method of position reconstruction: the MLE-maximum is located on a finite grid spanning the crystal geometry. For events with actual MLE-maxima outside the used grid of reconstruction, the position is estimated on the edges of the grid because the actual MLE-maxima are not covered by the calibrations scans. (Because of the finite position resolution, some MLE-maxima can be located outside the used grid of reconstruction).

As the DOI is simultanuously estimated for the 3D-MLE procedure when reconstructing the x and y positions, it is possible to evaluate the xy-position resolution as function of DOI. In order to do this, 6 DOI-bins of 2 mm width were set up.

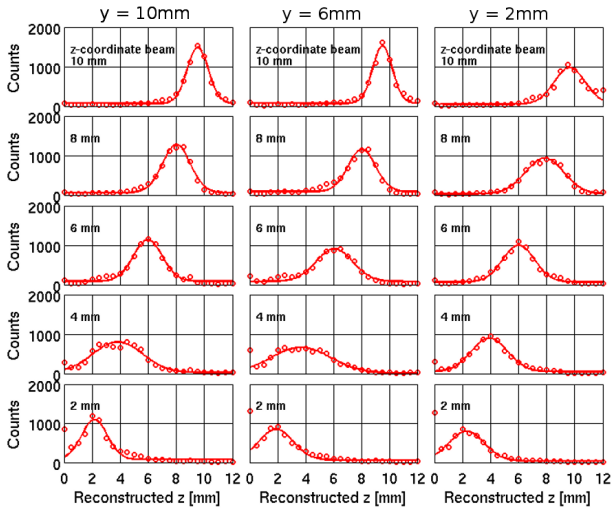

Figure 4.10: z-resolutions for YZ beam positions in the center (y = 10 mm), off center (y = 6 mm) and edge (y = 2 mm) of the crystal. The MAPMT is located at z = 12mm.

Individual reconstruction results were assigned to the proper bin, according to the estimated DOI. Because the 3D-MLE procedure has a good linearity performance (see Fig. 4.8), reconstructions at multiple xy-beam positions could be merged to build up statistics. For this purpose, the reconstructed profiles for the xy-beam positions in the central 10 mm × 10 mm square (25 beam positions) were aligned and merged. The resulting FWHM position resolution as function of DOI is shown in Fig. 4.9. It is apparent that the position resolution improves when the gamma photon interaction position approaches the photosensor. In combination with the exponential attenuation law for gamma photons, this explains the general observation that the position resolution is better when a light sensor is placed at the side of the crystal facing the beam instead of at the opposite side [38, 86]. A practical consideration in this respect is the absorption of the gamma photons by the light sensor. This prohibits positioning a PMT on the crystal side facing the beam, but is not an issue for thin semiconductor light sensors.

4.3.3 z-estimation

Since the YZ-scan provides the detector response at defined z-positions, it is possible to evaluate the z-reconstruction performance of the detector by estimating the position-of-interaction for the events from the YZ-scan. Fig. 4.10 shows the z-resolution for events in the YZ-scan in three regions of the crystal. For locating

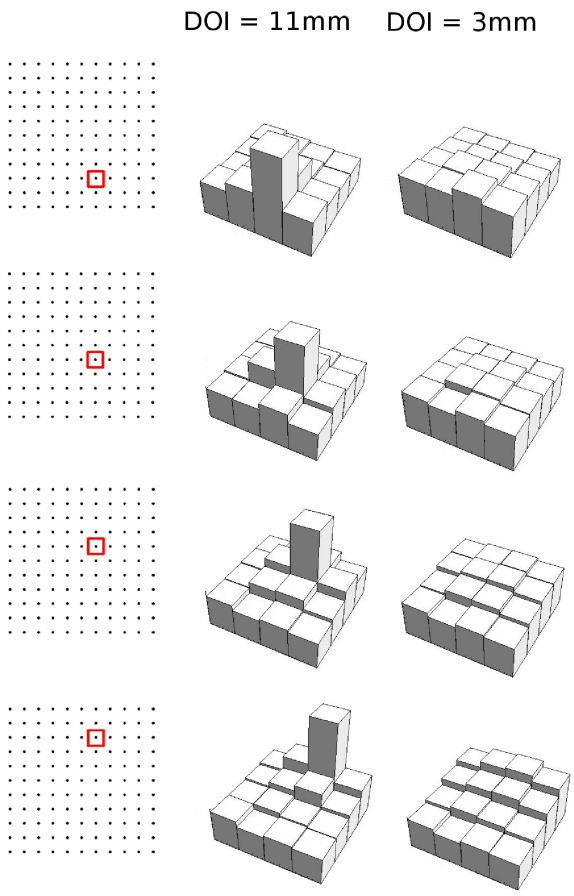

Figure 4.11: Average scintillation photon distribution patterns $\{\overline{m}_1, \overline{m}_2, \ldots, \overline{m}_{16}\}$. *The left column indicates xy-beam positions for which the* $\{\overline{m}_1, \overline{m}_2, \ldots, \overline{m}_{16}\}$ *patterns are shown at* $10 \leq DOI \leq 12$ *mm (center column) and* $2 \leq DOI \leq 4$ *mm (right column).*

the MLE-maxima in eq. 4.7, 3D-localization was applied using the 3D-calibration set built from the YZ-scan. The FWHM z-resolution is about 2.3 mm for events near the sensor array (high z-coordinate) and degrades to about 4 mm for events away from the sensor array. The effect of events being attributed to the edge of the crystal as seen in Fig. 4.8 also shows up here. For events near the sensor array (high z-coordinate) a systematic error in the z-estimation is present. Sorting the z-reconstructions according to the estimated x-coordinate, it appeared that this systematic error showed up for events at small x-coordinates. Apparently there

was a systematic error in the 3D-YZ calibration set for events that interacted in this region. It might have been caused by systematic errors in the x-estimation at high z-coordinates by the 2D-MLE procedure that was used to build up the 3D-YZ calibration set (see section 4.2.5). Fig. 4.8 also showed that the 2D-MLE procedure had difficulty handling events near the edge of the crystal.

For events from the XY-scan, average photon distribution patterns as a funtion of the reconstructed z-position (i.e. DOI) were set up. This was done by sorting the events from each xy-beam position into 6 DOI-bins of 2 mm width according to the reconstructed DOI. The DOI was reconstructed by locating the MLE-maxima in eq. 4.7, applying 3D-localization using the 3D-calibration set built from the YZ-scan. For each xy-beam position, each DOI-bin and each anode, the m_i distribution (see section 4.2.4) was fitted by a Gaussian and the resulting centroid $\overline{m}_i$ was recorded. $\{\overline{m}_1, \overline{m}_2, \ldots, \overline{m}_{16}\}$ thus represented the average scintillation photon distribution pattern. Fig. 4.11 shows the calculated patterns for 4 xy-beam postions at small DOI (DOI = 3 mm) and large DOI (DOI = 11 mm). The patterns show the expected behavior: for positions-of-interaction near the MAPMT (i.e. large DOI), there is a high local flux of scintillation photons at the nearby anode location, resulting in a peaked distribution. This flux is more uniform over the MAPMT when the postion-of-interaction is at a larger distance from the MAPMT (i.e. small DOI), resulting in a more uniform distribution. No prior knowledge on the scintillation photon distribution patterns was used during the estimation of the DOI (see sections 4.2.4 and 4.2.5). It demonstrates that the DOI is correlated with the scintillation photon distribution width at the sensor array, even in the presence of a reflective Spectralon enclosure (section 4.2.1).

These results show that monolithic scintillation crystals are suitable for accurate DOI-reconstruction using only one photosensor array. A block detector composed of crystal segments is not able to do this directy, since it confines the scintillation light to a single crystal segment and thus the correlation between DOI and scintillation photon distribution width at the sensor array is lost.

Extrapolating the DOI reconstruction result in Fig. 4.10 to thicker monolithic scintillation crystals coupled to a single photosensor array, we expect that DOI reconstruction is possible for gamma interactions located at a distance of at least 20 mm from the photosensor array.

4.3.4 Arrival time versus DOI

Sorting the events from the XY-scan according to the reconstructed DOI (as in section 4.3.3) allows the evaluation of the arrival time as a function of DOI. The average arrival time was calculated by fitting the time difference (LYSO time minus BaF_2 time) spectrum by a Gaussian and recording the centroid. The LYSO and BaF_2 times were determined by the time pickoff method in section 4.2.2. Fig. 4.12

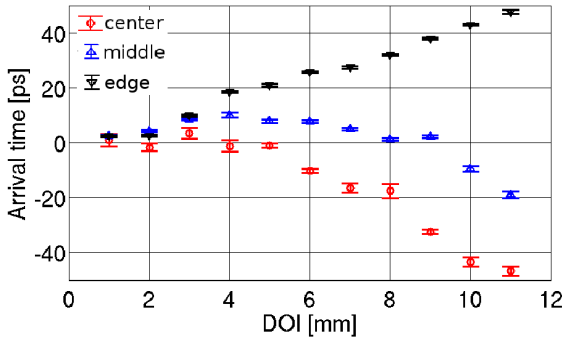

Figure 4.12: Fitted centroid of the time difference spectra (LYSO minus BaF_2 arrival time) as a function of DOI for XY-beam positions in the three crystal regions shown in Fig. 4.13. The error bars indicate the 95%-confidence bounds. The MAPMT is located at DOI = 12mm.

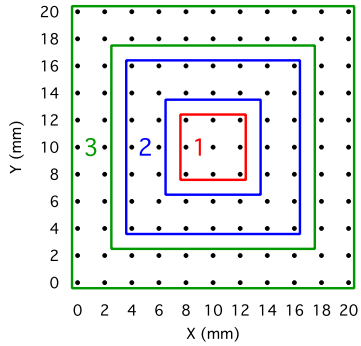

Figure 4.13: Regions selected in the XY-scan for analysis of the DOI time walk effect (Fig. 4.12): center (1); middle (2); edge (3). The dots represent the calibration scan grid.

shows the result for the three crystal regions shown in Fig. 4.13.

One observes a time walk vs. DOI, but the walk behavior is not uniform across the crystal. For the central region, events at large DOI are detected earlier than events at small DOI (the LYSO minus the BaF_2 arrival time is smaller). For the middle region in Fig. 4.13, the time walk is less apparent; for the edge region, events at large DOI are detected at a later time than events at small DOI.

Fig. 4.14 provides some insight into this complex walk behavior. For each event, the dynode energy was calculated from the digitized MAPMT dynode waveforms (shown in Fig. 4.2) by a digital summing operation along the time axis. Events

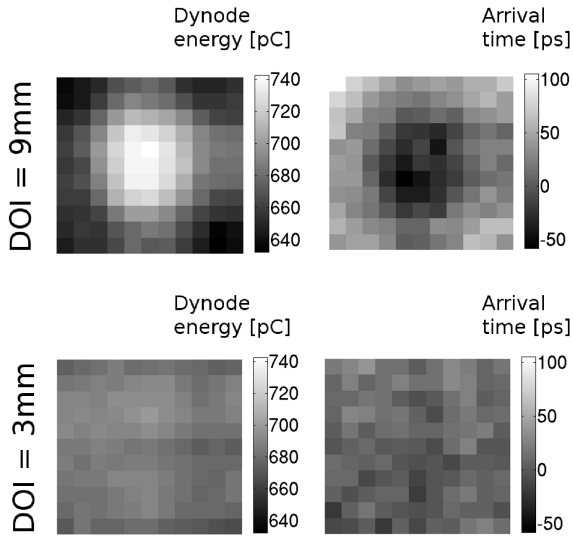

Figure 4.14: Dynode energy distribution and arrival time distribution in the transversal xy-planes located at large DOI ($8 \leq DOI \leq 10$ mm) and small DOI ($2 \leq DOI \leq 4$ mm). Each xy-bin corresponds to a beam position in the scan grid (Fig. 4.13).

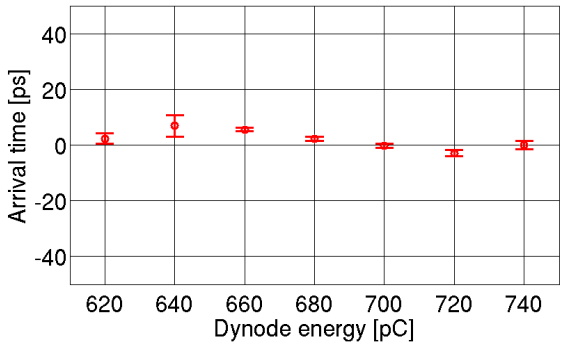

Figure 4.15: Fitted centroid of the time difference spectra (LYSO minus BaF_2 arrival time) as a function of the dynode energy in 20 pC bins for the transversal xy-plane located at small DOI ($0.5 \leq DOI \leq 1.5$ mm). The error bars indicate the 95% confidence bounds.

from the XY-scan were sorted into 2×2×2 mm^3 voxels according to the beam-defined x- and y-position and the reconstructed DOI. For each voxel, Gaussian fits of the dynode energy distribution and the time difference distribution were

performed. The energy and time centroids are shown in Fig. 4.14 for the z-planes at large DOI (9 mm) and small DOI (3 mm). Note that the time walk graphs in Fig. 4.14 show the same behavior as the time walk graph in Fig. 4.12. It is apparent that the average dynode energy shows the same pattern over position as the time walk and that these two quantities are thus somehow related.

It has to be checked whether the constant fraction time pickoff algorithm (section 4.2.2) was able to correct for time walk induced by pulse amplitude variation. (Since the pulse amplitude is determined by the dynode energy, this might be a possible explanation for the observed relationship between time walk and dynode energy). This can be done by selecting a crystal region for which there is no time walk variation over position, and verifying that the average arrival time over dynode energy is constant in this region. In Fig. 4.12 and 4.14 one observes that there is almost no time walk over xy-position for the crystal region at small DOI. Although the average dynode energy is also constant in this region (Fig. 4.14), this does not imply that there is no variation in dynode energy over the events: The FWHM of the LYSO dynode energy resolution is equal to 11.4%, which is normal for LYSO at 511 keV. This variation in LYSO dynode energy at small DOI covers the full range of the variation in *average* LYSO dynode energy over the entire crystal shown in Fig. 4.14. Fig. 4.15 shows the arrival time variation over dynode energy at small DOI ($0.5 \leq \text{DOI} \leq 1.5$ mm). It is apparent that there is virtually no time walk over dynode energy in this region, as desired from the time pickoff algorithm. The correlation between the average dynode energy and the time walk in Fig. 4.14 can thus not be attributed to the time pickoff algorithm.

A potential cause for the time walk and dynode energy variation over position might be a non-uniformity in the response between the MAPMT anodes. The MAPMT response was characterized according to the method in section 4.2.7. The energy and time centroids vary randomly over the anodes, no pattern can be discerned. The dynode energy and arrival time patterns observed in Fig. 4.14 can thus not be attributed to the anode non-uniformity of the MAPMT. At large DOI the largest fraction of the scintillation light is collected by the center anodes for events from the center region (see Fig. 4.11). The same holds for the edge anodes for events from the edge region. By averaging the centroids of the time difference spectra over the four center anodes and the twelve edge anodes separately, it appeared that the center anodes reacted on average about 20 ps faster than the edge anodes. For the LYSO crystal, there was a variation in the average arrival time at large DOI (DOI = 11 mm) of $\sim$100 ps between events from the center and edge region (see Fig. 4.12). This also means that the arrival time variation at large DOI can not be attributed to the anode non-uniformity of the MAPMT.

When one excludes the possibility that the dynode energy variation over position is caused by a non-uniformity in the response between the MAPMT anodes, the variation can only be caused by a varying scintillation light loss over posi-

tion. This implies that for scintillation locations at large DOI nearby the crystal side surfaces the largest number of scintillation photons is lost (see Fig. 4.14); for scintillation locations at large DOI in the center of the crystal the smallest number of scintillation photons is lost; while at small DOI the loss is more uniform vs. x,y position and in between these two extremes. Likewise, when one excludes that the time walk variation over position is caused by a non-uniformity in the response between the MAPMT anodes, the variation can only be caused by a variation in travel time of the scintillation photons from their point of creation to the photosensor.

Photon loss is to be attributed to self-absorption inside the crystal and absorption at the surfaces, and as such depends on the scintillator material quality, the surface finish and the packaging. Reflection at the surfaces is on average accompanied by a longer travel path and thus longer travel time as well as larger self-absorption. The observed time walk behavior thus results from differences in the scintillation photon transport from the place of creation to the sensor.

Light collection is slower towards the edges/corners due to the increased importance, because of geometric reasons, of reflections with the crystal surfaces. This effect is enhanced at large DOI because the crystal surface coupled to the MAPMT (20×20 mm^2) is somewhat larger than the sensitive area of the MAPMT (18×18 mm^2). The time walk is reduced for small DOI because of the vicinity of the crystal front edge which reflects scintillation photons that were emitted away from the MAPMT, increasing the early photon flux towards the MAPMT, i.e. speeding up the arrival of the first few photons, and thus counteracting the time walk with DOI. The speed of scintillation photons within the crystal is equal to c/n (with c the speed of light in vacuum and n the index of refraction, about 1.82 for LYSO). The maximum average arrival time variation of $\sim$100 ps in Fig. 4.12 translates into an average path length variation of $\sim$16 mm, not surprisingly comparable to the crystal size.

Using the observed time walk vs. 3D gamma interaction position, an event-by-event software correction to the timing can be applied. After correction, the residual time walk throughout the crystal is at the level of just a few ps. For the detector used in this work, only a small improvement of the overall coincidence timing resolution from 358 to 354 ps FWHM results (see Table 4.1), since most gamma photons interact at small DOI, where time walk is small. When only taking events at large DOI into account, the improvement is larger (see Table 4.1).

For $3\times3\times30$ mm^3 LSO crystals Moses and Derenzo reported arrival time variations between 200 ps and 400 ps, depending on the crystal surface treatment [89]. It was shown that this effect significantly degraded the timing resolution for detectors utilizing these crystals. They attributed the effect to the scintillation light undergoing multiple reflections at quasi-random angles within the crystal.

The crystal thickness in the current work was equal to 12 mm. For thicker

Table 4.1: Coincidence resolving times (CRTs) for different DOI regions. The third column indicates the obtained CRTs after performing a position correction to the timing. The fourth column indicates the improvement in CRT due to this correction.

DOI region [mm]	FWHM CRT without correction [ps]	FWHM CRT with correction [ps]	CRT improvement [ps]
[0 - 12]	357.7 ± 0.5	353.5 ± 0.5	4.2
[6 - 12]	360.4 ± 0.5	352.5 ± 0.5	7.9
[9 - 12]	364.8 ± 0.8	352.6 ± 0.7	12.2
[10.5 - 12]	368.0 ± 1.1	351.7 ± 0.9	16.3

monolithic crystals one expects a larger arrival time variation, thereby degrading the timing resolution. A time walk correction according to the estimated interaction position may improve the timing resolution for such crystals.

4.4 Conclusion

In order to investigate the time walk as function of photoconversion location inside a monolithic crystal coupled to a photosensor array, a maximum likelihood estimation algorithm that determines the x-, y-, and z (i.e. DOI)-coordinates of the photoconversion location was developed. For a 20 mm × 20 mm × 12 mm LYSO crystal coupled to a fast 4×4 multi-anode photomultiplier tube, a spatial resolution in the plane of the MAPMT of 2.4 mm FWHM is obtained. The DOI-resolution ranges from 2.3 mm FWHM near the photomultiplier tube to 4 mm FWHM at a distance of 10 mm. These resolution are uncorrected for the ∼1 mm diameter beam of annihilation photons. In a coincidence set-up with a BaF_2 detector, timing signals were digitized at 2 GS/s and digital time pickoff was performed. A coincidence timing resolution of 358 ps FWHM was obtained. A time walk depending on the 3D photoconversion location is observed. The time walk throughout the crystal spans a range of 100 ps. Calibrating the time walk vs. interaction location allows an event-by-event correction that leaves a residual time walk of just a few ps, making it irrelevant for the timing performance of the detector. From an extrapolation of our results, we estimate that the DOI resolution is sufficient to correct for time walk such that it becomes irrelevant up to a crystal thickness of at least 20 mm, thick enough for an L(Y)SO-based PET scanner. The same can

hold for even thicker crystals when using a photosensor array at both the front and back. This geometry is possible with solid-state sensors such as silicon photomultipliers, and is especially relevant for $LaBr_3$ crystals as the rather large 511 keV attenuation length of 22 mm warrants the use of thick crystals.

5 Thick monolithic scintillation crystals for TOF-PET with depth-of-interaction measurement

This chapter has been published as: R. Vinke, H.T. van Dam, S. Seifert, F.J. Beekman, H. Löhner, D.R. Schaart, and P. Dendooven, "Thick monolithic scintillation crystals for TOF-PET with depth-of-interaction measurement," in 2010 IEEE Nucl. Sci. Symp. Conf. Record, NM3-3, 2010.

Abstract

Positron emission tomography (PET) detectors based on monolithic scintillation crystals show excellent intrinsic spatial resolution and allow depth-of-interaction (DOI) reconstruction using a single photosensor array. The inclusion of time-of-flight (TOF) information in the image reconstruction significantly reduces the image noise variance, effectively increasing the PET system sensitivity. For optimal detection efficiency, thick crystals are needed. However, the attainable spatial resolution decreases as the crystal thickness is increased. A maximum-likelihood-estimation (MLE) algorithm was developed to determine the 3D gamma interaction position. We present results on positioning and timing performance vs. crystal thickness for three monolithic LYSO crystals (16.2 mm × 18 mm × z, z = 10 mm, 15 mm, or 20 mm) coupled to a multi-anode photomultiplier (MA-PMT). The positioning performance varied with the distance to the MA-PMT. For the 20 mm thick LYSO crystal the position resolution parallel to the MA-PMT varied between 2.5 and 4.5 mm FWHM with the distance, while the DOI could be reconstructed with a resolution varying between 2 and 5 mm FWHM. For the 20 mm thick LYSO crystal in coincidence with a fast BaF_2 detector, a coincidence resolving time (CRT) of 324 ps FWHM was obtained using digital time pickoff. We observed a signal propagation time variation with gamma interaction position from 30 ps for the 10 mm thick crystal to 65 ps for the 20 mm thick crystal. We conclude that thick monolithic scintillation crystals for optimal detection efficiency show very good timing resolution, which hardly degrades when increasing the crystal thickness from 10 mm to 20 mm, and allow for accurate position reconstruction (including DOI) at minimal detector costs (using a single photosensor array to read out the crystal).

5.1 Introduction

Positron emission tomography (PET) detectors based on monolithic scintillation crystals show excellent intrinsic spatial resolution and allow depth-of-interaction (DOI) reconstruction using a single photosensor array due to the correlation of the width of the scintillation light distribution across the sensor array with the DOI. Including time-of-flight (TOF) information in image reconstruction significantly reduces the image noise variance, which effectively increases the PET system sensitivity. For optimal detection efficiency, thick crystals are needed. However, the attainable spatial resolution decreases as the crystal thickness is increased, due to an increasing fraction of full-energy events for which the gamma photon undergoes multiple interactions within the crystal (producing various scintillation centers) and due to an increasing spread of the scintillation light distribution. In the same way, the attainable spatial resolution is better for events close to the photosensor than events distant from the photosensor, since events close to the photosensor produce a narrower scintillation light distribution at the photosensor plane.

In our study of the performance of monolithic TOF-PET detectors, we have developed a maximum-likelihood-estimation (MLE) algorithm to determine the 3D gamma interaction position [64] as well as digital time pickoff techniques [90] and combined these to correct for the time walk vs. interaction position. Here we present results on detector performance vs. crystal thickness.

5.2 Materials and Methods

5.2.1 Experimental setup

The experimental setup, shown in Fig. 5.1, is briefly described; for more details, see [64]. Polished LYSO crystals (16.2 mm × 18 mm × z, z = 10 mm, 15 mm, or 20 mm) were coupled to a Hamamatsu H8711-03 4×4 multi-anode photomultiplier (MA-PMT) using optical grease; all other crystal sides were wrapped in reflective Teflon tape. The last, common, dynode signal served as 'timing signal'; the anode ('energy') signals were sent directly to a LeCroy 4300B 16-channel QDC interfaced to a CAMAC system. The LYSO detector was put in coincidence with a fast BaF_2 detector, having a timing resolution for 511 keV photons of about 180 ps. The dynode (timing) signals of both detectors were sent to an Agilent DC282 waveform digitizer (4 GS/s per channel, 10 bit voltage resolution, 700 MHz anti-aliasing filter). The energy and timing information for each event were combined by synchronizing the QDC and waveform digitizer.

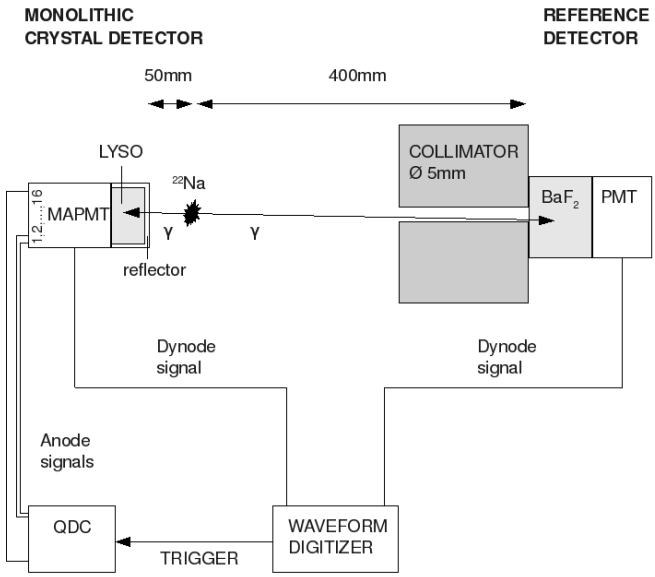

Figure 5.1: Schematic overview of the experimental setup

5.2.2 Time pickoff method

Fig. 5.2a shows typical timing signals of both detectors. In order to minimize the influence of the digitizer noise on the timing resolution, the digitizer input range was set to a low value of 100 mV (∼20% of the 511 keV pulse amplitude for both detectors). No timing accuracy is lost by this procedure as the first part of the pulse rising edge corresponds to the earliest detected scintillation photons, and is thus associated with a minimum time spread. For timing analysis, coincidence events with energies falling in the FWTM range of the 511 keV photopeak for both detectors were selected. A timestamp was derived by applying a leading edge time-pickoff (trigger level 5 mV above a baseline determined for each trace before the onset of the pulse) to a cubic spline interpolation of each sampled pulse.

5.2.3 Position determination

The detector response was calibrated as function of gamma beam position by scanning a pencil beam (∼1 mm diameter) across the 16.2 mm × 18 mm front surface (XY-scan) and one of the 18 mm × z side surfaces (YZ-scan) of the crystal. An MLE algorithm combining information from these two scans allowed to reconstruct the 3D interaction position of the gamma photons inside the crystal (see [64] for this method). For position analysis, only events with energies falling in the FWTM

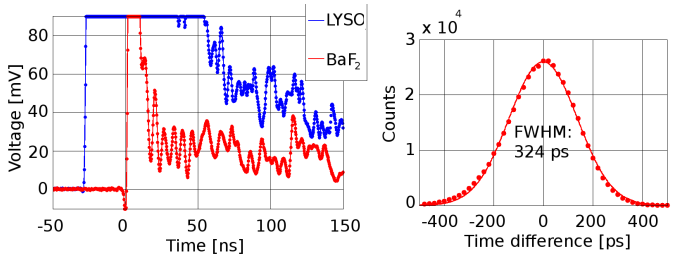

Figure 5.2: a) Typical 511 keV LYSO (blue) and BaF_2 (red) timing signals. Dots: digitizer sampled points. Lines: cubic spline interpolation. b) Coincidence timing spectrum for the 16.2 mm × 18 mm × 20 mm LYSO detector in coincidence with the BaF_2 detector. A Gaussian fit (solid line) gives a FWHM of 324 ps.

range of the 511 keV photopeak were taken into account.

5.3 Results and discussion

5.3.1 Energy resolution

The energy resolutions of the 16.2 mm × 18 mm × z LYSO detectors were about 11%, a value typical for LYSO and thus indicating good light collection and detection efficiency.

5.3.2 Timing

Fig. 5.2b shows the timing resolution for the 16.2 mm × 18 mm × 20 mm crystal detector in coincidence with the BaF_2 detector. A coincidence resolving time (CRT) of 324 ps FWHM was obtained. Quadratic subtraction of the 180 ps timing resolution of the BaF_2 detector results in a single detector resolution of 270 ps FWHM (and a CRT of 380 ps FWHM for two such detectors). Comparable timing resolutions were obtained for the smaller crystal detectors (see Table 5.1). We attribute the minor variation in resolution to small differences in the assembly of the detectors, leading to differences in optical coupling and crystal surface reflection properties.

Average signal propagation times inside the LYSO crystals are determined as the center of the timing spectra (deduced from a fit with a Gaussian). Fig. 5.3 shows the results as function of the gamma beam excitation depth in the side-surface scan, which corresponds to the DOI for beams entering the crystal front surface.

Table 5.1: Coincidence Resolving Times (CRTs) for the LYSO detectors.

Crystal thickness [mm]	FWHM CRT [ps]
10	332 ± 1
15	333 ± 1
20	324 ± 1

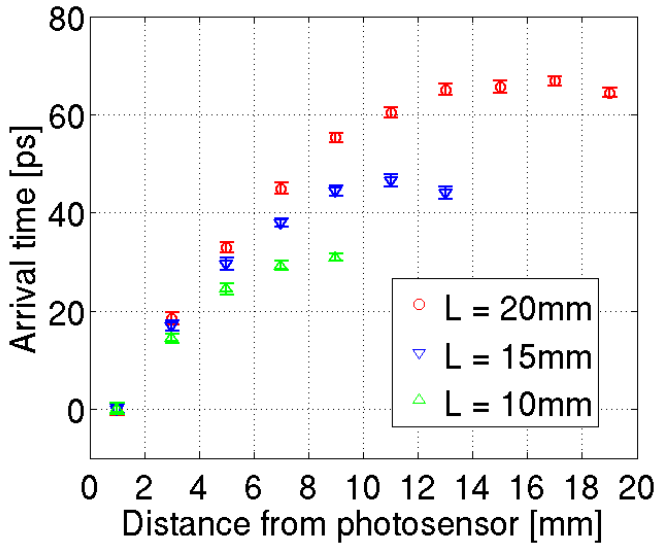

Figure 5.3: Average signal propagation time (arrival time) as a function of distance to photosensor. The timing distributions were merged for beam positions in the central 10 mm y-range of the crystal. L indicates the crystal thickness. Error bars indicate the 95%-confidence bounds.

Close to the photosensor, an appreciable time walk of about 8 ps/mm is observed. At a large distance from the photosensor, reflections from the crystal surface opposite to the photosensor boost the early arrival of scintillation photons, flattening the time walk behavior. The overall detector timing resolution might be improved by applying a position-dependent correction to the timing. For the present detector this gives no improvement. However, this might be an interesting opportunity for monolithic crystals read out by a semiconductor photosensor array on the front side of the crystal, facing the gamma photon source (to improve the positioning performance, see next section). Since the majority of gamma photons interact at small DOI (due to the exponential attenuation law), and thus close to the photosensor for such a configuration, the propagation time variation effect

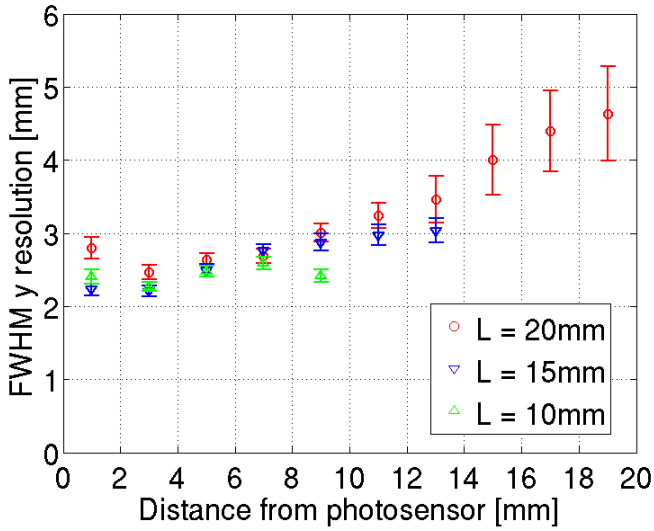

Figure 5.4: Position resolution in the y-direction vs. distance from photosensor for beams entering the crystal side surface at the center of the 18 mm y-range. L indicates the crystal thickness. Error bars indicate the 95%-confidence bounds.

on the overall timing resolution will be larger, and a correction more important. Earlier, we showed that excellent timing resolutions can be obtained for monolithic crystals coupled to SiPM arrays [90], thus making such a correction feasible.

5.3.3 Positioning

Fig. 5.4 shows the spatial resolution in the y-direction, determined using beams entering the crystal side surface. The spatial resolution degrades as the distance to the photosensor increases. Still, a reasonable spatial resolution of 4.6 mm FWHM is obtained at 19 mm from the MAPMT, even in the presence of the reflective crystal side surfaces. Fig. 5.5 shows the DOI resolution determined using beams entering the crystal side surface. The DOI resolution decreases as the distance to the photosensor increases. Still, a DOI resolution of 5.3 mm FWHM is obtained at 15 mm distance from the photosensor for the 20 mm thick crystal. Closer to the crystal front surface, the DOI reconstruction performance quickly deteriorates for the 15 and 20 mm thick crystals due to edge artifacts.

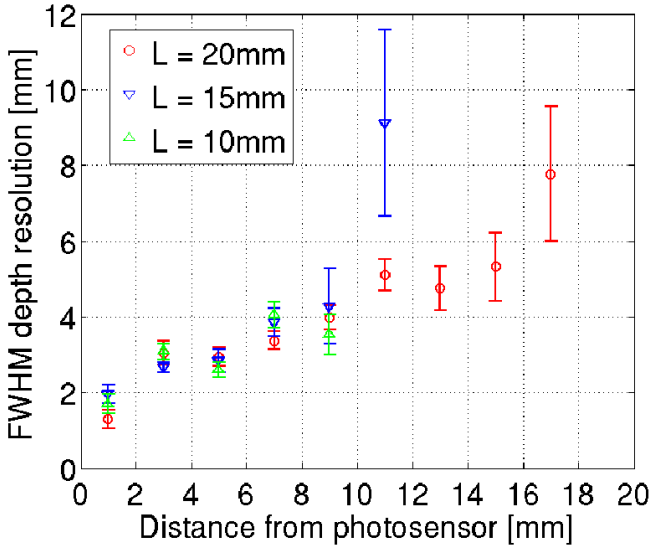

Figure 5.5: Depth resolution vs. distance from photosensor. The depth reconstruction results were merged for beam positions over the entire 18 mm y-range of the crystal. L indicates the crystal thickness.

5.4 Conclusions

We have shown that monolithic LYSO scintillation crystals with a thickness relevant for PET (until 20 mm) exhibit good energy and timing performance. The overall detector timing resolution may be further improved by applying a position-dependent correction to the timing. The DOI can be reconstructed with good resolution using only a single photosensor array (in contrast to PET detectors based on conventional segmented scintillation crystals, for which costly crystal and detector arrangements are necessary). The positioning performance degrades as the crystal thickness is increased, but might still be at an acceptable level if maximum detection efficiency is required at minimal detector costs (using a single photosensor array to read out the crystal). There is a trade-off between the crystal thickness (and thus the detection efficiency) and spatial resolution. Since semiconductor light sensors are essentially transparent to gamma rays, the spatial resolution can be improved by placing such a photosensor on the front surface of the crystal (facing the gamma beam), such that most gamma rays interact at a small distance from the photosensor. For such a configuration, a correction for the time walk vs. position-of-interaction may allow to maintain excellent timing resolution. For a crystal read out by photosensor arrays at two opposing sides, the positioning

performance is expected to improve even more. In the near future, the positioning and timing performance will be tested for a monolithic scintillation crystal read out by a SiPM array, whereby the SiPM array faces the gamma photon beam.

Acknowledgment

This work was supported by a 2010 IEEE MIC Trainee Grant.

6 Optimizing the timing resolution of SiPM sensors for use in TOF-PET detectors

This chapter has been published as: R. Vinke, H. Löhner, D. Schaart, H. van Dam, S. Seifert, F. Beekman, and P. Dendooven, "Optimizing the timing resolution of SiPM sensors for use in TOF-PET detectors," Nucl. Instr. and Meth. A, vol. 610, pp. 188-191, 2009.

Abstract

We have investigated the timing performance of Hamamatsu Multi-Pixel Photon Counter (MPPC) photosensors in light of their use in time-of-flight (TOF) positron emission tomography detectors. Measurements using picosecond laser pulses show a single photo-electron RMS timing resolution down to about 100 ps. In coincidences of 511 keV photons detected with an LYSO crystal coupled to a MPPC and a BaF_2 detector, an optimum FWHM timing resolution of 600 ps was obtained with leading edge time pickoff at the 1-1.5 photo-electron level. By optimizing the LYSO/MPPC coupling, this can be improved by a factor of 2. We further conclude that the use of stored digitized pulses allows great flexibility and efficiency in developing data analysis algorithms.

6.1 Introduction

In time-of-flight positron emission tomography (TOF-PET), the time difference in the detection of two 511 keV annihilation photons is used to narrow down the position of positron annihilation on the line-of-response between two detectors. Improving on spatial resolution of present-day whole-body PET scanners (about 3-5 mm) would require a timing resolution better than ∼30 ps. Present technology is far from reaching this goal; the only commercially available TOF-PET scanner has a timing resolution of ∼600 ps [8]. In the foreseeable future the great advantage of TOF-PET is in reducing the image noise rather than allowing a direct determination of the annihilation position [6].

Several TOF-PET scanners using BaF_2 and CsF scintillator detectors were developed in the 1980's [91]. These efforts were abandoned with the advent of the BGO scintillator, due to its higher detection efficiency. The more recent discovery of scintillators such as L(Y)SO (highly efficient and fast) and $LaBr_3$ (very bright

and fast), has revived the TOF-PET research and it is to be expected that many PET scanners will soon be TOF-capable.

In parallel with advances in scintillator materials, new fast and cost-effective photosensors are being developed. The so-called silicon photomultiplier (SiPM) is at the forefront of this development [92]. It combines low noise, high gain and fast timing. Single-photo-electron timing resolutions close to 50 ps root-mean-square (RMS) have been reported [93]. SiPMs are insensitive to high magnetic fields, making them compatible with a Magnetic Resonance Imaging (MRI) environment and thus suitable for combined PET/MRI scanners (e.g. [94]).

We are developing novel PET detector technology based on monolithic scintillators and pixellated light sensors [38]. This concept promises improved sensitivity and spatial resolution. We are giving high priority to TOF capability and compatibility with an MRI environment, two of the major technological focus points in PET technology today. To meet these requirements, we use SiPM light sensor arrays.

The aim of the present work is to improve the timing capabilities of SiPM based scintillation detectors through the development of optimized fast amplifiers and time pick-off techniques.

6.2 Experimental set-up

In all measurements described here, signal traces were digitized using an Acqiris DC282 digitizer with 10 bit resolution and, when using one input channel, an 8 GS/s sampling rate. Data presented here were obtained using two input channels, resulting in 4 GS/s for each channel. The advantage of this approach in which the full detector signals are stored, is that analysis algorithms can be developed and optimized using the same data set. This allows great flexibility and removes any suspicion of changing experimental conditions that might arise in extensive measurement series.

The basic timing properties of SiPMs from Hamamatsu (so-called Multi-Pixel Photon Counter, MPPC) were investigated using a picosecond laser. A Hamamatsu PLP10-40 laser diode head (wavelength 405 nm) with C10196 Controller was used. The laser pulse width is $\sim$70 ps; time jitter with the "synch out" output from the Controller is less than 10 ps. 1 mm^2 MPPCs with microcell size 25$\times$25, 50$\times$50 and 100$\times$100 μm^2 (model S10362-11-025U, -050U and -100U), thus having respectively 1600, 400 and 100 microcells, were illuminated with laser pulses with intensity regulated using neutral density filters. The MPPC signals were amplified by a custom-built fast voltage amplifier (amplification factor 10), giving an average signal rise time of 1.2 ns. The amplifier output and the laser controller synch out were sent to the Acqiris digitizer and events containing both digitized traces were

stored.

In a second set of measurements, a 2×2×8 mm^3 LYSO crystal was mounted on the MPPCs. Using a ^{22}Na source, coincidences with a BaF_2 detector were measured. This detector (Scionix model 25.4 B 20 / 2Q-BAF-X-NEG + VD29-124KT) consists of a 20 mm thick, 25.4 mm diameter crystal mounted on an XP2020Q photomultiplier tube and has a timing resolution for 511 keV photons of about 180 ps. The LYSO and BaF_2 signals were sent to the Acqiris digitizer.

6.3 Results and discussion

For the measurements with picosecond laser pulses, only MPPC traces containing a single pulse and no afterpulses are used for further analysis. The fraction of pulses that are distorted by afterpulses and spontaneous breakdowns increases with increasing operating voltage. For the 400-microcell MPPC, the fraction of single photo-electron pulses that are distorted by afterpulses is 12% for 1.0 V over-voltage and 45% for 2.0 V over-voltage. This limits the maximum usable operating voltage (and thus also the maximum gain).

The pulse height spectrum for the 1600-microcell MPPC at low light intensity level is shown in Fig. 6.1. The clear peak separation demonstrates the photon counting capability of these devices and allows one to translate the peak amplitude to the number of fired cells. Because of the linear relationship between MPPC gain and reverse bias, the breakdown voltage can be determined by measuring the peak amplitude (or peak charge) as a function of operating voltage for a number of multiple-photo-electron peaks (Fig. 6.2).

The pulse arrival time is determined by using a digital form of constant fraction discrimination (dCFD) [95]. For each trace, the signal amplitude is determined as the difference between the signal maximum and the baseline level (Fig. 6.3); the latter being determined as the average of the signal samples preceding the MPPC pulse. The pulse arrival time is then taken as the time at which the rising edge of the signal crosses a trigger level equal to the baseline level plus the 30% fraction of the signal amplitude. A linear interpolation of time vs. signal between the two consecutive samples with amplitudes below and above the trigger level is performed. The arrival time of the synch out pulse is determined in the same way. However, as the synch out provides a standard pulse, its time jitter is for all practical purposes independent of the time pickoff method. A histogram of differences between the MPPC and synch out pulse arrival times is constructed and the resulting peak fitted with a Gaussian, with the RMS timing resolution as one of the fit parameters. The timing resolution was found to be optimum for a dCFD fraction of 30%, but not very sensitive to it.

Fig. 6.4 shows the RMS timing resolution for the 400-microcell MPPC as func-

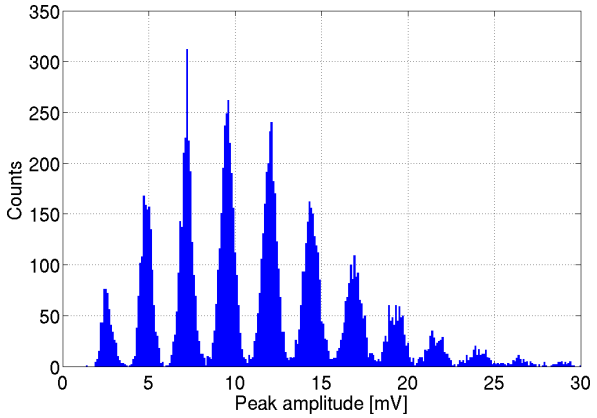

Figure 6.1: Pulse height distribution for the 1600-microcell MPPC operated at 71 V. Clear separation of peaks corresponding to a different number of photo-electrons is seen.

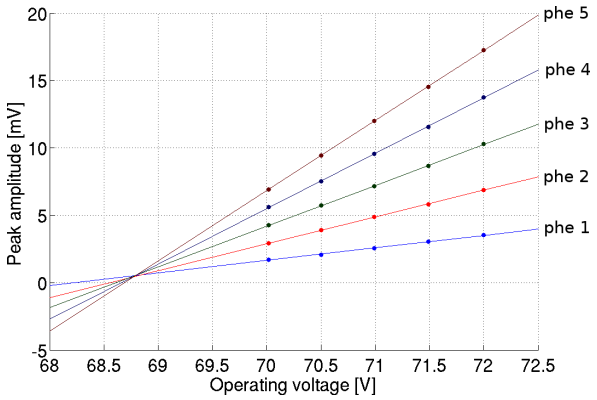

Figure 6.2: Determination of the breakdown voltage for the 1600-microcell MPPC. The peak amplitudes for the 1^{st} to 5^{th} photo-electron peaks are linear with operating voltage and cross at the breakdown voltage.

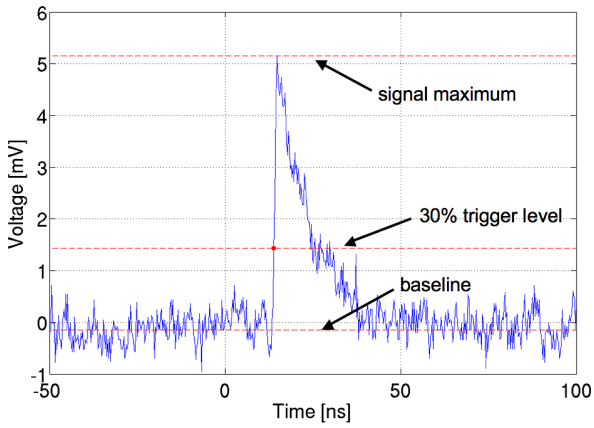

Figure 6.3: Time pickoff procedure on a single photo-electron signal.

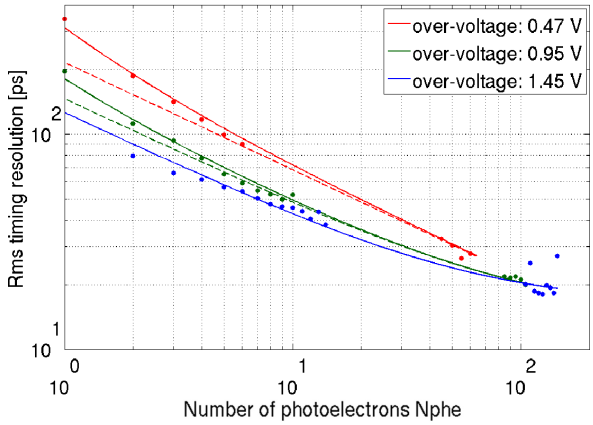

Figure 6.4: RMS timing resolution as function of the number of photo-electrons for the 400-microcell MPPC for several operating voltages (voltage above breakdown is indicated). Solid lines represent the fit of eq. 6.2. Dotted lines show the fit neglecting the electronic noise contribution and using only data points for which $N_{phe} > 5$. The higher the gain (i.e. over-voltage), the smaller the difference between these fits.

tion of the number of detected photo-electrons and for a number of operating voltages. The three contributions to the timing resolution are described below. A single-point comparison time pickoff method gives a timing error (σ_n) associated with the RMS electronic noise voltage ($\tilde{v}_n$) [96]:

$$\sigma_n = \tilde{v}_n (dv_r/dt)^{-1} \tag{6.1}$$

where dv_r/dt is the signal slope at the trigger point. Assuming a pulse risetime independent of pulse amplitude, the signal slope is proportional to the pulse amplitude. The amplitude scales with the MPPC gain, whereas in our measurements, $\tilde{v}_n$ is constant at about 0.3 mV: σ_n thus decreases with increasing gain. As the pulse amplitude is proportional to the number of detected photo-electrons (N_{phe}), $\sigma_n \propto 1/N_{phe}$. For the data point in Fig. 6.4 with over-voltage 0.47 V and N_{phe}=1, dv_r/dt=1.1 mV/ns, giving σ_n=270 ps; the fit with Eq. 6.2 gives a compatible value of 230 ps. The time from when a photon enters the MPPC until the output pulse appears shows a certain jitter. This internal timing resolution of the device (σ_i) is best described by Poisson statistics, i.e. $\sigma_i \propto 1/\sqrt{N_{phe}}$. A residual contribution (σ_0) is caused by additional sources that do not depend on N_{phe}, such as sampling clock jitter and laser synch out jitter. The independent contributions add in quadrature to give the measured timing resolution (σ_m):

$$\sigma_m^2 = \sigma_i^2 + \sigma_n^2 + \sigma_0^2 = \frac{\sigma_{i,spe}^2}{N_{phe}} + \frac{\sigma_{n,spe}^2}{N_{phe}^2} + \sigma_0^2 \tag{6.2}$$

where the subscript "spe" refers to the single photo-electron value of the corresponding RMS timing resolution. Fig. 6.5 shows the RMS s.p.e. internal timing resolution as function of over-voltage for the MPPC devices; a s.p.e. timing resolution down to about 100 ps is obtained.

In the measurements with the LYSO crystal, the highest scintillation photon flux on the photosensor occurs during the initial moments of the scintillation process. The associated time spread is therefore lowest when triggering on the first detected photon [97]. The fastest photons are those travelling in a straight line to the photosensor. Due to the geometric mismatch between the 2x2 mm^2 scintillator side and the 1x1 mm^2 MPPC, we estimate a four-fold loss in the detection of these fastest photons and, according to Poisson statistics, a 2-fold loss in timing resolution. The low number of scintillation photons hitting the sensor (about 400 out of 13 000 for the full absorption of a 511 keV annihilation photon) points to a non-optimal intrinsic optical coupling of the crystal to the sensor; optimizing this coupling should improve the timing resolution further. Although a less than optimum timing performance is thus to be expected, we could investigate the optimum time pickoff procedure in an efficient manner by using the same set of stored

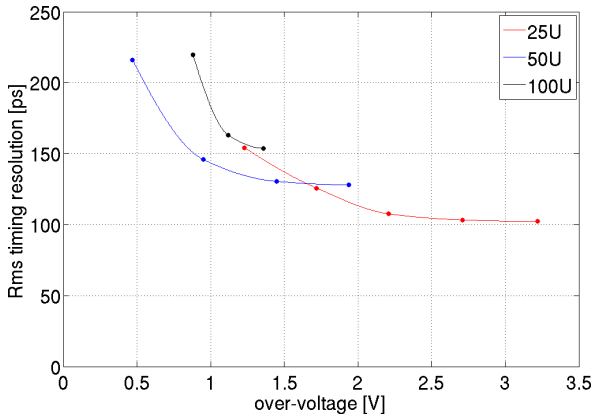

Figure 6.5: RMS single photo-electron timing resolution as function of over-voltage.

digitized detector pulses. Events for which the full 511 keV photon energy was detected in both detectors were selected for analysis.

Our results confirm that it is best to trigger on the first photon detected. Fig. 6.6 shows the best timing resolution using a leading edge trigger at a trigger level for the LYSO detector equivalent to 1-1.5 photo-electrons, about 3% of the 511 keV signal height. For trigger levels comparable to the noise level, the timing performance decreases as the trigger level crossing time is influenced by the noise. In these measurements, the combination of digitizer quantization noise and preamplifier electronic noise was 1.5 mV RMS; an increase in timing resolution is observed for trigger levels <4 mV.

The best timing resolution was obtained for the 100-microcell MPPC because it has a higher photon detection efficiency (PDE) due to its higher fill factor, resulting in a higher fraction of detected initial scintillation photons.

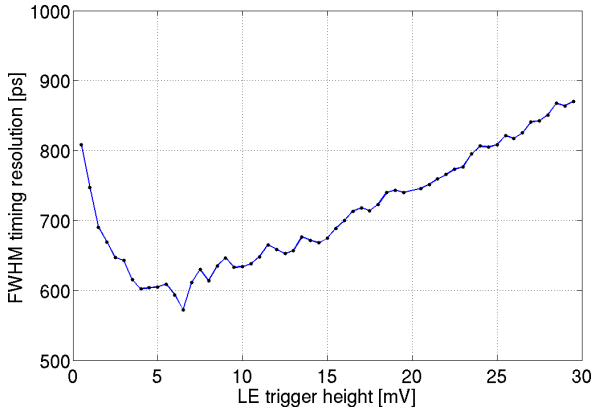

Figure 6.6: FWHM coincidence timing resolution between a BaF_2 reference detector and a LYSO crystal mounted on a 100-microcell MPPC as a function of leading edge trigger level of the LYSO detector. Time pickoff on the BaF_2 is also performed by leading edge triggering.

7 $LaBr_3$:Ce and SiPMs for time-of-flight PET: achieving 100 ps coincidence resolving time

This chapter has been published as: D.R. Schaart, S. Seifert, R. Vinke, H.T. van Dam, P. Dendooven, H. Löhner, and F.J. Beekman, "$LaBr_3$:Ce and SiPMs for time-of-flight PET: achieving 100 ps coincidence resolving time," Phys. Med. Biol., vol. 55, pp. N179-N189, 2010.

Abstract

The use of time-of-flight (TOF) information in positron emission tomography (PET) enables significant improvement in image noise properties and, therefore, lesion detection. Silicon photomultipliers (SiPMs) are solid-state photosensors that have several advantages over photomultiplier tubes (PMTs). SiPMs are small, essentially transparent to 511 keV gamma rays and insensitive to magnetic fields. This enables novel detector designs aimed at e.g. compactness, high resolution, depth-of-interaction (DOI) correction and MRI compatibility. The goal of the present work is to study the timing performance of SiPMs in combination with $LaBr_3$:Ce(5%), a relatively new scintillator with promising characteristics for TOF-PET. Measurements were performed with two, bare, 3 mm × 3 mm × 5mm $LaBr_3$:Ce(5%) crystals, each coupled to a 3 mm × 3 mm SiPM. Using a ^{22}Na point source placed at various positions in between the two detectors, a coincidence resolving time (CRT) of ∼100 ps FWHM for 511 keV annihilation photon pairs was achieved, corresponding to a TOF positioning resolution of ∼15 mm FWHM. At the same time, pulse height spectra with well-resolved full-energy peaks were obtained. To our knowledge this is the best CRT reported for SiPM-based scintillation detectors to date. It is concluded that SiPM-based scintillation detectors can provide timing resolutions at least as good as detectors based on PMTs.

7.1 Introduction

The use of time-of-flight (TOF) information in positron emission tomography (PET) has recently been demonstrated to enable significant improvement in image noise properties and, therefore, lesion detection, especially in heavier patients [7, 51, 98–100]. This warrants further research into TOF-capable PET scintillation detectors, in particular with the aim to obtain better timing resolution.

The relatively new inorganic scintillator $LaBr_3$:Ce has high potential for TOF-PET [101]. Commercial-grade $LaBr_3$:Ce(5%) has a fast decay time of ∼16 ns [102], a high light yield of ∼70.000 photons MeV^{-1} [103], an excellent energy resolution of ∼2.6% FWHM at 662 keV [104], a mass density of 5.1 g cm^3 [105] and an effective atomic number of 46.9 [25]. To optimally benefit from the advantages of $LaBr_3$:Ce in a PET detector, the scintillation light should be read out using a photosensor with fast response and high photodetection efficiency (PDE) at the $LaBr_3$:Ce emission wavelengths (∼380 nm).

Excellent coincidence resolving times (CRTs) have already been demonstrated with $LaBr_3$:Ce crystals of various dimensions and Ce concentrations, coupled to fast photomultiplier tubes (PMTs) [106–108]. However, silicon photomultipliers (SiPMs) are turning into a promising alternative for PMTs, as of recently [42, 109–117]. Similar to PMTs, SiPMs have a gain in the order of $\sim 10^6$. In addition, these solid-state devices are much more compact and essentially transparent to 511 keV gamma rays. This enables novel detector designs aimed at, for example, compactness, high resolution, depth-of-interaction (DOI) correction, etc [86, 118–124]. Moreover, in contrast with PMTs, SiPMs are compatible with magnetic fields, a feature that is very interesting in light of recent endeavours to combine PET and MRI into hybrid imaging devices [94, 125–127].

The goal of the present work is to study the timing performance of commercially available 3 mm × 3 mm SiPMs in combination with $LaBr_3$:Ce(5%) for TOF-PET. We use relatively small $LaBr_3$:Ce(5%) crystals to minimize time walk due to the variation of photon path lengths with the position-of-interaction. However, when using larger crystals, one may attempt to achieve similarly good timing resolution by applying a position-of-interaction correction to the timing information [61, 89, 128].

7.2 Materials and methods

7.2.1 Detectors

Measurements were performed with two, identical, SiPM-based scintillation detectors. In each detector a bare 3 mm × 3 mm × 5 mm $LaBr_3$:Ce(5%) crystal (Saint-Gobain BrilLanCe 380) was enclosed in a reflective casing made from Spectralon, a PTFE-based material with reflectivity specified to be better than 98% at 380 nm, i.e. the wavelength of maximum emission of $LaBr_3$:Ce(5%). A 3 mm × 3 mm SiPM (Hamamatsu MPPC-S10362-33-050C) was coupled directly to each of the $LaBr_3$:Ce crystals using a transparent silicone encapsulation gel (Lightspan LS-3252). Each SiPM consists of an array of 3600 self-quenched Geiger Mode Avalanche Photodiodes at a pitch of 50 μm. Both SiPMs were operated at ∼2.0 V above their breakdown voltages, which were measured to be ∼69.7 V and ∼70.1 V,

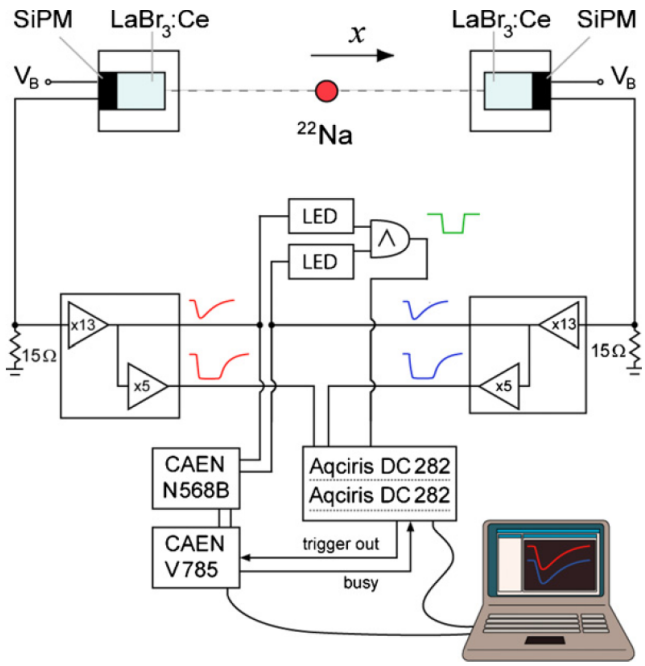

Figure 7.1: Schematic overview of the experimental setup. See the text for explanation.

respectively. All experiments were performed at room temperature and in a dry atmosphere to protect the hygroscopic $LaBr_3$:Ce crystals.

7.2.2 Measurement setup

Figure 7.1 shows a schematic representation of the measurement setup. The two detectors and a ^{22}Na point source (Isotope Products Laboratories, active volume $\varnothing$ 0.5 mm $\times$ 1 mm) were mounted on an optical rail, such that the source could be placed at various positions x in between the two detectors.

The SiPM charge pulses were converted to voltage pulses by means of 15 Ω shunt resistors and fed into voltage preamplifiers made in-house. Each preamplifier consisted of two cascaded amplification stages, as indicated in figure 7.1. The first amplification stage (gain $\sim$13) consisted of a Texas Instruments OPA847 opamp in a non-inverting configuration with a feedback resistor of 270 Ω and a 22 Ω resistor to ground. The second stage (gain $\sim$5) consisted of an ac-coupled monolithic microwave integrated circuit (MMIC) low noise amplifier (Avago Technologies MGA-61563). Care was taken to minimize the total length of the leads

between the SiPM and the preamplifier (< 1 cm).

In the timing experiments, the signals of the first amplification stages were used to obtain a coincidence trigger, by feeding them into LeCroy 825 leading edge discriminators (LEDs) and connecting the discriminator outputs to a LeCroy 465 coincidence unit. The signals of the first amplification stages were also used to determine the two pulse heights of each coincident pulse pair. This was done by feeding these signals into a CAEN N568B multi-channel shaping amplifier (shaping time 100 ns) connected to a CAEN V785 multi-channel, peak-sensitive ADC.

The pulses from the secondary amplification stages of the two preamplifiers were digitized by two, synchronized, Acqiris DC282 fast sampling ADCs. Both ADCs were operated at the maximum sampling rate of 8 GS s^{-1} and at a 10-bit resolution. The synchronization clock jitter between the two ADCs is specified to be $\leqslant 1$ ps. The trigger for the two synchronized ADCs was provided by the above-mentioned LeCroy 465 coincidence unit. The gain of the secondary amplification stages was chosen such that the ADC input range (set to 500 mV) corresponded to only ∼12.5% of the amplitude of a 511 keV pulse. As the optimum trigger threshold for timing lies within this portion of the pulse rising edge, this approach minimizes the contribution of ADC noise to the overall signal-to-noise ratio of the digitized (partial) pulse traces. The traces of each coincident pulse pair were stored in a PC, together with the corresponding pulse heights recorded by the CAEN V785 ADC. The stored data were subsequently used for offline, digital time pick-off as described in section 7.2.3.

Experiments were also performed by irradiating the detectors with a ^{22}Na source and feeding the signals from the first amplification stages of the preamplifiers directly into the Acqiris ADCs, using an ADC input range larger than the maximum pulse amplitude and applying no coincidence condition. About 105 full pulse traces thus acquired were stored for offline analysis of the pulse shape and energy content.

7.2.3 Digital time pickoff

A selection of digitized pulse traces for timing analysis was performed using the pulse height information recorded by the CAEN V785 ADCs. Only events with energies between ∼490 keV and ∼532 keV were accepted, corresponding to the full-width-at-tenth-maximum (FWTM) of the full-energy peak. Time stamps were subsequently derived by interpolating each trace with a cubic spline and determining the intersection of the interpolated data with a fixed threshold relative to the baseline, set at approximately nine times the pulse height of a single photon pulse. The baseline was determined for each trace individually as the average signal in the region between ∼1.2 ns and ∼0.2 ns before the onset of the pulse.

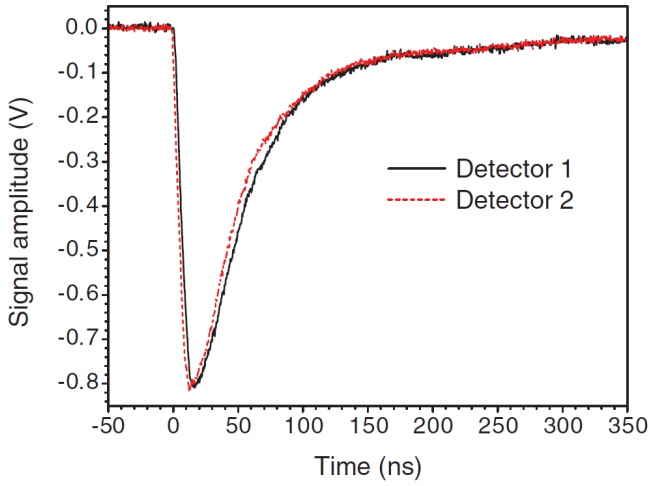

Figure 7.2: Typical digitized pulse traces of the two detectors, measured with 511 keV photons. The average 10-90% rise time of the recorded 511 keV pulses equals ∼9 ns.

7.3 Results

7.3.1 Pulse shape

Figure 7.2 shows some typical examples of 511 keV pulse traces from the two detectors. These were obtained by feeding the outputs of the first amplification stages of the preamplifiers directly into the Acqiris DC282 ADCs. The average 10-90% rise time of the pulses in the full-energy peak equals ∼9 ns. As the pulse shape equals the convolution of the scintillation light pulse and the SiPM response, the rise time is primarily determined by the low pass (i.e. integrating) characteristics of the SiPM and the scintillation decay time. The influence of the high-bandwidth preamplifiers and other electronics on the pulse rise time is expected to be negligible in our measurements.

7.3.2 Timing spectra

Figure 7.3 shows the timing spectra obtained with the ^{22}Na point source located at positions $x_1 =$ óÃÉ20 mm ± 0.25 mm (green diamonds), $x_2 = 0$ mm ± 0.25 mm (black squares) and $x_3 = 20$ mm ± 0.25 mm (blue circles). These spectra were obtained using the digital time pickoff method described in section 7.2.3, using 3624, 7326 and 3346 coincident events per spectrum, respectively. The FWHM coincidence resolving times (CRTs), determined from Gaussian fits to the data

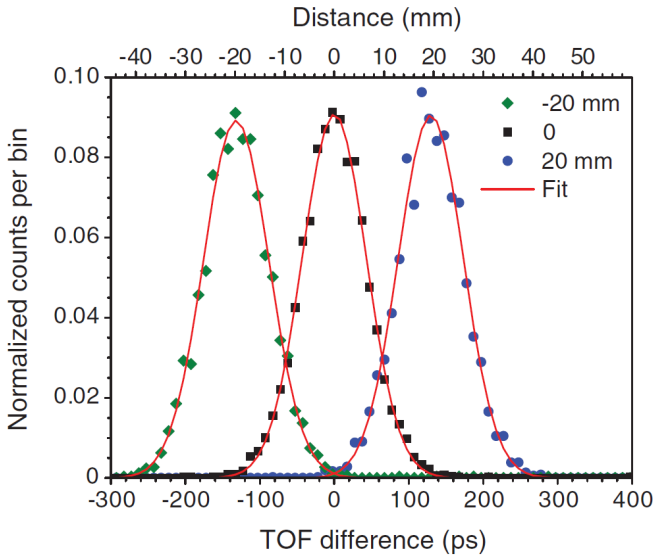

Figure 7.3: Timing spectra recorded with two 3 mm × 3 mm × 5 mm $LaBr_3$:Ce crystals read out by 3 mm × 3 mm SiPMs, using a ^{22}Na point source located at x_1 = óÃÉ20 mm ± 0.25 mm (green diamonds), x_2 = 0 mm ± 0.25 mm (black squares), and x_3 = 20 mm ± 0.25 mm (blue circles). The red curves indicate Gaussian fits to the data. The average coincidence resolving time (CRT) equals 101 ps ± 2 ps FWHM, corresponding to 15.1 mm ± 0.3 mm FWHM.

(the red curves in the figure), are 101.8 ps, 99.5 ps and 103.4 ps for x_1, x_2 and x_3, respectively. The weighted average of these values equals 101 ps ± 2 ps FWHM, corresponding to a TOF positioning resolution of 15.1 mm ± 0.3 mm FWHM.

7.3.3 Pulse height spectra

Figure 7.4 shows the ^{22}Na pulse height spectra measured with both detectors. These were derived by integration of the digitized pulses from the first amplification stages of the preamplifiers. A baseline correction was applied to each pulse before integration. The 511 keV full-energy peaks can be seen to be superimposed on the Compton ridges of the 1275 keV peaks. The latter peaks are relatively small due to the small crystal size.

The observed widths of the 511 keV peaks are ∼3.7% FWHM and ∼3.2% FWHM for detector 1 and detector 2, respectively. These small widths are partly due to SiPM saturation, as discussed in more detail in section 7.4.3. Nevertheless, all full-energy peaks are well resolved and can be clearly distinguished from the

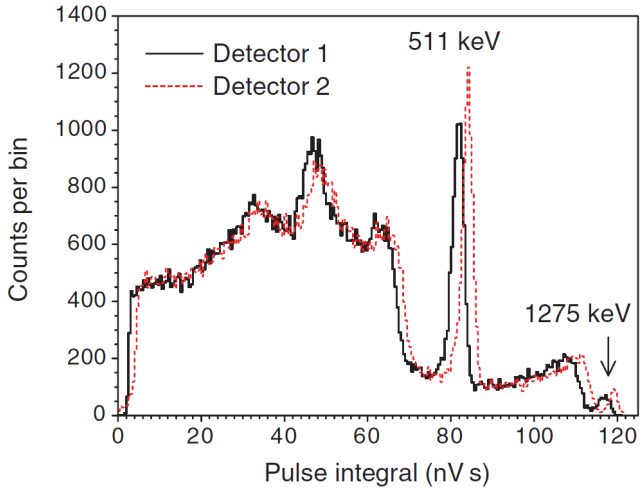

Figure 7.4: Pulse height spectra of the two detectors, measured using a ^{22}Na source. The observed widths of the 511 keV peaks are ∼3.7% FWHM and ∼3.2% FWHM for detector 1 and detector 2, respectively.

corresponding Compton ridges.

7.4 Discussion

7.4.1 Timing performance

The above results were achieved using detectors based on 3 mm × 3 mm × 5 mm $LaBr_3$:Ce(5%) crystals and 3 mm × 3 mm SiPMs. To obtain sufficient system sensitivity, a clinical TOF-PET scanner might, for example, be based on several stacked layers of such detector elements. Alternatively, the detector design might be based on longer crystals. The use of monolithic crystals read out by position-sensitive SiPM arrays may also be considered. While many different detector designs could thus be envisaged, the timing performance is generally expected to deteriorate in larger crystals due to the variation of photon path lengths with the position-of-interaction. Fortunately, it may be possible to at least partly correct for this effect if the position-of-interaction in the crystal is known [61, 89, 128]. The results presented here may thus be seen as representing the CRT in principle achievable with $LaBr_3$:Ce(5%) and 3 mm × 3 mm SiPMs commercially available at the time of writing.

The present work can be compared to results obtained with SiPMs by other authors. Several studies have been performed using LSO:Ce and similar materials.

Some of the best results reported are those from Göttlich *et al* [129], which reached a CRT of 460 ps FWHM using two 3 mm × 3 mm × 15 mm lutetium fine silicate (LFS) crystals coupled to the same Hamamatsu SiPMs as the ones used here, those from Burr and Wang [130], which obtained a CRT of 268 ps FWHM using two 3 mm × 3 mm × 10 mm LYSO:Ce crystals and prototypes of the same SiPMs as used in the present study and those from Kim *et al* [131], which achieved a CRT of 240 ps FWHM using 3 mm × 3 mm × 10 mm LYSO:Ce crystals coupled to the same SiPMs as those used here.

Few studies have so far been performed with $LaBr_3$:Ce [132], presumably because of the difficulties encountered in using this hygroscopic material. To our knowledge the CRT obtained with $LaBr_3$:Ce(5%) in the present work is significantly better than those reported for LSO:Ce, LYSO:Ce and LFS to date.

It is acknowledged that the performance of a PET scintillator is not only determined by its timing resolution. Compared to LSO:Ce and similar materials, a disadvantage of $LaBr_3$:Ce is its lower stopping power, giving rise to increased intra- and inter-crystal scattering and requiring thicker detectors to obtain equal detection efficiency. In principle, thicker detectors may give rise to increased parallax errors. However, these can be mitigated by using stacked layers of small detector elements as mentioned above or by implementing some form of depth-of-interaction (DOI) correction, see e.g. [42] and references therein.

An important advantage of $LaBr_3$:Ce is its much higher light yield, which is a crucial factor for obtaining high spatial resolution. Moreover, both its superior timing (randoms suppression, TOF) and its excellent energy resolution (scatter rejection) are of great advantage to improve image quality, especially in heavier patients [133].

Given the above advantages and disadvantages, at present it is difficult to predict the overall performance of $LaBr_3$:Ce in comparison to other PET scintillators, especially since the only $LaBr_3$:Ce-based prototype scanner realized to date [133] has not yet been optimized with respect to all of the above factors. In contrast, LSO:Ce and similar materials are used in many commercial systems, most of which have undergone multiple iterations of optimization. Thus, further research into the use of $LaBr_3$:Ce in TOF-PET is warranted.

7.4.2 SiPMs versus PMTs

The average 10-90% rise time of ∼9 ns obtained in this study is relatively large compared to the values typically found with fast PMTs. For example, Kuhn *et al* [106] measured a 10-90% rise time of ∼3 ns for a 4 mm × 4 mm × 30 mm $LaBr_3$:Ce(5%) crystal on a Hamamatsu R4998 PMT. In principle, a longer rise time is undesirable as the timing resolution ÕÅt associated with electronic and

sampling noise is equal to the ratio of the noise and the signal slope [96]:

$$\sigma_t \sim \frac{\sigma_v}{dv/dt} \tag{7.1}$$

where σ_v is the RMS noise voltage and dv/dt denotes the slope of the pulse leading edge at the point where it crosses the trigger level.

However, the absolute slope dv/dt is proportional to the photosensor photodetection efficiency. It is not trivial to specify the PDE of the SiPMs used here, since it is a function of bias voltage, temperature, degree of saturation, etc and varies between individual devices of the same type. However, according to the manufacturerÕÀÊs data sheet [134], it may be as high as ∼45% at 380 nm, the wavelength of maximum emission of $LaBr_3$:Ce(5%). While it is to be noted that this figure includes contributions from cross-talk and after-pulsing [117, 135], it is considerably higher than the quantum efficiency (QE) of, for example, the above-mentioned R4998 PMT, which is estimated to be ∼16% at 380 nm from the manufacturerÕÀÊs datasheet [136]. A second advantage of a higher PDE is that a larger number of primary charge carriers per pulse reduce the influence of statistical fluctuations on the timing resolution.

A full analysis of the timing resolution would require additional factors to be taken into account, such as photosensor dark current, transit time jitter, etc, but this is left for future publication. In this note we merely wish to illustrate that the different characteristics of SiPMs and PMTs make it interesting to compare the timing resolution achieved in this work with those published for PMTs in combination with the same scintillation material.

For example, a CRT of 240 ps FWHM has been measured with two, 4 mm × 4 mm × 30 mm $LaBr_3$:Ce(5%) crystals coupled to R4998 PMTs [106], while Kyba *et al* [107] reported a CRT of 160 ps FWHM for two ∅ 13 mm × 13 mm $LaBr_3$:Ce(5%) crystals coupled to the same PMTs, thereby demonstrating the dependence of CRT on crystal dimensions. A simulation by Kuhn *et al* [106] predicts a CRT of ∼100 ps FWHM for very small crystals. The dependence of CRT on the time pick-off method was tested by Wiener *et al* [137] by comparing analogue to digital methods. Although it was originally reported that the CRT with digital waveform sampling was superior, further work has since demonstrated that these measurements are sensitive to the assumptions made about the shape of the signal rising edge, and that the timing resolutions obtained with digital and analogue methods are comparable (private communication). Given these results, the present work indicates that SiPM-based scintillation detectors can provide timing resolutions at least as good as those obtained with PMTs.

It is noted that scintillators exist that may provide even better timing resolution than commercial-grade $LaBr_3$:Ce(5%). For example, increasing the Ce concentration in $LaBr_3$:Ce to ∼30% appears to improve timing resolution signif-

icantly [106, 138]. Other materials, such as $CeBr_3$ and LuI_3:Ce, are also investigated as candidates for TOF-PET [108, 139, 140]. Hence, it would be interesting to study the timing performance of SiPMs in combination with $LaBr_3$:Ce(30%) and other promising new materials.

7.4.3 SiPM saturation

In principle, it might also be possible to further improve the timing resolution by using SiPMs containing fewer but larger microcells, thus improving their fill factor and, therefore, their PDE. However, if the number of microcells would be made too small, this might lead to excessive saturation. Such saturation causes the pulse height spectra of SiPM-based scintillation detectors to increasingly be compressed along the energy axis with increasing gamma energy [141, 142]. As can be seen from the relative positions of the 511 keV and 1275 keV peaks in figure 7.4, a significant degree of saturation already occurs in the present experiments. While the excellent energy resolution of $LaBr_3$:Ce already gives rise to a relatively small width of the 511 keV full-energy peaks, this implies that the peak widths observed in figure 7.4 are additionally reduced by SiPM saturation. From a practical point of view, however, it is important that well-resolved 511 keV full-energy peaks are still obtained. In a clinical PET system, this is crucial for accurate rejection of photons that have undergone Compton scattering in the patient. It is noted that, in addition to SiPM saturation, the pulse height spectra may in principle also be influenced by electronic non-proportionality as described by Seifert *et al* [143, 144]. However, this effect is expected to be small in our measurements.

7.5 Conclusions

The experiments presented here show that SiPM-based scintillation detectors for TOF-PET can provide timing resolutions at least as good as detectors based on conventional PMTs. At the same time, pulse height spectra with well-resolved full-energy peaks can be obtained, which is necessary for accurate rejection of Compton-scattered photons. The use of $LaBr_3$:Ce(5%) allowed us to achieve a CRT of ∼100 ps FWHM for 511 keV annihilation photon pairs, corresponding to a TOF positioning resolution of ∼15 mm FWHM. To our knowledge this is the best experimental figure reported for SiPM-based scintillation detectors to date. It is not unlikely that further optimization of scintillation materials and SiPM technology will lead to even better results in the near future. Given the advantages of SiPMs over PMTs, such as their small size, transparency to 511 keV gamma rays, magnetic field compatibility, etc, we conclude that detectors based on $LaBr_3$:Ce and SiPMs have high potential for use in TOF-PET devices.

Acknowledgments

We would like to thank Joel Karp of the Department of Radiology, University of Pennsylvania, PA, USA, for helpful discussions. This work was supported in part by SenterNovem under grant no IS055019.

8 Optimization of digital time pickoff methods for $LaBr_3$-SiPM TOF-PET detectors

This chapter has been published as: R. Vinke, S. Seifert, D. Schaart, F. Schreuder, M. de Boer, H. van Dam, F. Beekman, H. Löhner, and P. Dendooven, "Optimization of digital time pickoff methods for $LaBr_3$-SiPM TOF-PET detectors," in 2009 IEEE Nucl. Sci. Symp. Conf. Record, pp. 2962-2968, 2009.

Abstract

The relatively new inorganic scintillator $LaBr_3$:Ce is well suited for time-of-flight positron emission tomography (TOF-PET), since it has short scintillation decay time, high light yield and very good energy resolution. Silicion photomultipliers (SiPMs) show low noise, high gain and small transit-time jitter, and are thus well suited for fast timing applications. The work presented here focuses on the timing performance of bare $LaBr_3$:Ce(5%) crystals coupled to commercially available SiPMs. First, relatively small crystals coupled to single SiPMs were used to study the intrinsic timing resolution of such detectors. Special attention was paid to the optimization of digital signal processing (DSP) time-pickoff methods. A coincidence timing resolution of 101 ps FWHM was achieved. Next, a monolithic $LaBr_3$:Ce crystal was coupled to a 4×4 SiPM array and an intial timing performance characterization was performed. A single detector timing resolution of 225 ps FWHM was achieved. The timing delay induced by the scintillation photon transport was virtually constant over the depth-of-interaction (DOI) range of the detector.

8.1 Introduction

It is well known that significant improvements in image quality can be achieved when using time-of-flight (TOF) information in the image reconstruction process for positron emission tomography (PET): the noise variance in the image is significantly reduced, thereby effectively increasing the PET system sensitivity [6, 8]. For this purpose, the timing resolution of TOF-PET scintillation detectors needs to optimized. The relatively new inorganic scintillator $LaBr_3$:Ce is well suited for TOF-PET [101], since it has short scintillation decay time (∼16 ns [102]), high light yield (∼70.000 photons/MeV [103]) and very good energy resolution (∼2.6% at 662 keV [104]). Excellent timing performance has been shown for $LaBr_3$:Ce crystals coupled to photomultipliers (PMTs) [106–108]. Silicion photomultipliers

(SiPMs) are a new solid state alternative to PMTs [42, 109–117]. Showing low noise, high gain and small transit-time jitter, they are well suited for fast timing applications (see e.g. [145]).

The overall goal of our work is to study the performance of monolithic scintillation crystals of the TOF-PET relevant scintillators $LaBr_3$:Ce and L(Y)SO, read out by an array of SiPMs. It has already been shown that statistics-based positioning algorithms give excellent intrinsic spatial resolution for detectors based on monolithic crystals [37, 48, 65, 85, 86], with depth-of-interaction (DOI) reconstruction capability [49, 64, 128]. The absence of dead space (as present between crystal pixels in standard block detectors) allows very high system sensitivity [83].

The work presented here focuses on the timing performance of bare $LaBr_3$:Ce(5%) crystals coupled to commercially available SiPMs. First, relatively small crystals coupled to single SiPMs were used to study the intrinsic timing resolution of such detectors. Special attention was paid to the optimization of digital signal processing (DSP) time-pickoff methods. Next, monolithic $LaBr_3$:Ce(5%) crystals were coupled to 4×4 SiPM arrays. The timing resolution deteriorates for this latter configuration, because the scintillation light has to be shared over multiple SiPMs, with each SiPM introducing dark counts, and each associated preamplifier introducing electronic noise to the scintillation signal. Additionally, the variation of the scintillation photon path lengths inside the crystal increases due to the larger dimension of the crystal, which might increase the position-of-interaction related time walk. To study the last effect, the time walk as function of the reconstructed 3D position-of-interaction is measured. If present, a position correction to the timing might improve the timing resolution for thick monolithic scintillation crystals.

8.2 Materials and methods

8.2.1 Small crystal pixel setup

For a detailed description of the small crystal pixel setup, the reader is referred to [146]. This section is a summary of that description.

All experiments were performed in a dark box under a protective, dry atmosphere (because of the hygroscopicity of the $LaBr_3$:Ce crystals).

Two detectors consisting of bare 3×3×5 mm^3 $LaBr_3$:Ce(5%) crystals coupled to 3×3 mm^2 SiPMs (Hamamatsu MPPC-S10362-33-050C) with 50×50 μm^2 microcell size were assembled. All crystal surfaces not coupled to the SiPM were covered with highly reflective material (Spectralon® [88]) to maximize the scintillation light collection efficiency. A ^{22}Na source provided 511 keV positron annihilation photons. A high-bandwidth low-noise preamplifier provided two signal branches: an 'energy signal' and a 'timing signal'. Compared to the energy signal, the timing signal had a higher amplification (60× versus 12×). The timing signals were

acquired by an Agilent DC282 waveform digitizer running at 8 GS/s for both detectors and at 10 bit voltage resolution, with digitizer electronic anti-aliasing (low-pass) filter set at 700 MHz. By using the high amplification for the timing signal, the digitizer noise contribution to the timing resolution σ_t was minimized [96]:

$$\sigma_t = \frac{\sigma_v}{dv/dt} \tag{8.1}$$

where σ_v is the RMS noise voltage and dv/dt the slope of the pulse rising edge at the trigger level. The energy signals were simultaneously acquired by a second acquisition system that was synchronized with the waveform digitizer. For timing analysis, only coincidence events were taken into account with energies falling in the full-width-at-tenth-max (FWTM) range of the 511 keV photopeak for both detectors.

8.2.2 Monolithic crystal setup

A schematic of the monolithic crystal setup is shown in Fig. 8.1. All experiments were performed in a dark box under a protective, dry atmosphere.

A bare 16.2×18×10 mm^3 $LaBr_3$:Ce(5%) polished crystal was coupled to a Hamamatsu S11064-050P(X1) 4×4 SiPM array, with 3×3 mm^2 SiPM pixel size and 50×50 μm^2 microcell size (i.e. 3600 cells per SiPM pixel), using silicone encapsulation gel. The 16.2×18 mm^2 crystal front surface size matched the SiPM array size. To maximize the light collection efficiency, the crystal was wrapped in Teflon. The signals of the SiPM array were amplified using a 16 channel preamplifier made in-house. The 16 signal outputs of this preamplifier (the 'energy signals') were split after the first amplification stage. For each channel one branch was sent to a second amplification stage. The 16 branches were combined into an an analogue sum at this stage and formed the 'timing signal' of the monolithic crystal detector. In the electronic design it was ensured that the electrical path lengths were the same for the 16 branches that were used to generate the timing signal. A ^{22}Na source provided 511 keV positron annihilation photons. One of the small crystal pixel detectors, as described in section 8.2.1, was used as a reference detector. The timing signals of both detectors were sent to the Agilent DC282 waveform digitizer, mentioned in section 8.2.1. Timing traces were digitized at 8 GS/s for both detectors. The electronic anti-aliasing filter was set at 700 MHz for both detectors. The second branches of the 16 energy signals were fed into a CAEN N568B spectroscopy amplifier and read out by a peak sensing ADC (CAEN V785). The remaining branches were fed into a summing amplifier and subsequently sent to a discriminator to reject the majority of the Compton scattered events. The discriminator output of the monolithic crystal detector was combined with the

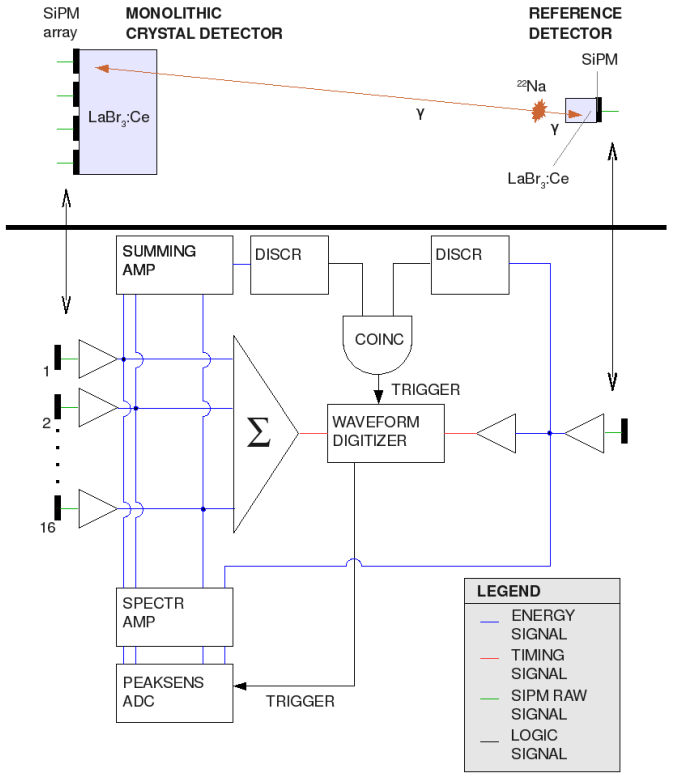

Figure 8.1: Schematic monolithic crystal setup. The blue lines indicate the energy signals, red lines the timing signals, green lines the SiPM current signals, black lines logic signals.

discriminator output of the reference detector in a logic coincidence unit, to accept coincidence events only. The output of this coincidence unit served as the trigger signal for the waveform digitizer. The systems acquiring the energy and timing signals (the peak sensing ADC and waveform digitizer, respectively) were synchronized in order to be able to combine the energy and timing information for each event.

For timing analysis, the monolithic crystal was placed at a large distance from the ^{22}Na source and reference detector to ensure a uniform illumination of the monolithic crystal (see Fig.8.2). Only 511 keV photopeak events were taken into account for further analysis by Gaussian fitting the energy spectra for both detectors and selecting events for which the detected energy was in the FWTM range of the fitted photopeaks for both detectors.

To be able to reconstruct the 3D position-of-interaction of the gamma photons

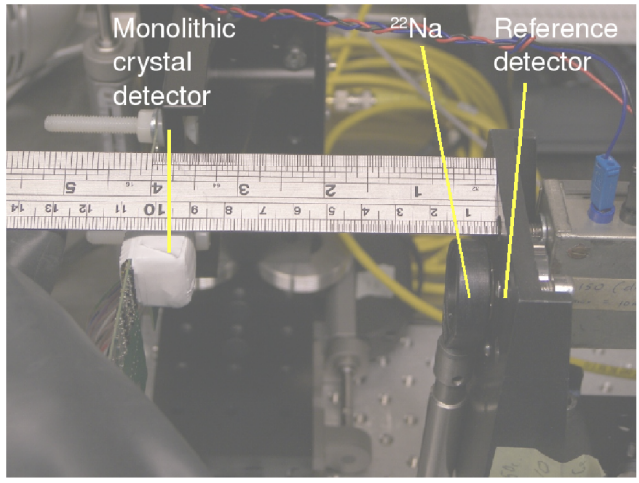

Figure 8.2: Monolithic crystal setup. To ensure uniform illumination of the monolithic crystal, it is placed at a large distance from the ^{22}Na source

in the scintillation crystal (see section 8.1), the detector response had to be calibrated as a function of gamma beam position. To obtain a beam with small spot size on the monolithic crystal, the ^{22}Na source was placed very close to the monolithic crystal (a few mm). The reference detector was placed at a distance of ∼30 mm to the ^{22}Na source at the opposite side. By only taking coincidence events into account, the beam is electronically collimated: due to geometric arguments the positions of annihilation photons have to lie within a cone inside the monolithic crystal, with a spot size of ∼1 mm diameter at the crystal surface facing the SiPM array. Two perpendicular motorized translation stages allowed scanning the monolithic crystal in the plane perpendicular to the beam and obtain a position calibration set. A calibration scan of the front surface (XY-scan) was made. After this, the detector was turned by 90 degrees and a calibration scan of one of the side surfaces (YZ-scan) was made. By combining the calibration information from these two directions, a 3D calibration set could be obtained. This 3D calibration set could then be used to estimate the 3D position-of-interaction of the gamma photons inside the crystal by Maximum Likelihood Estimation (MLE). By performing the systematic calibration procedure, it was not necessary to incorporate any prior knowledge on the scintillation photon distribution pattern from a theoretical or simulation model. The position could be estimated using only the information from the calibration procedure. An initial method for this 3D calibration and estimation can be found in [128]. A more refined method was used for the results in this work and can be found in [64].

The 3D position-of-interaction was estimated for the events in the timing analy-

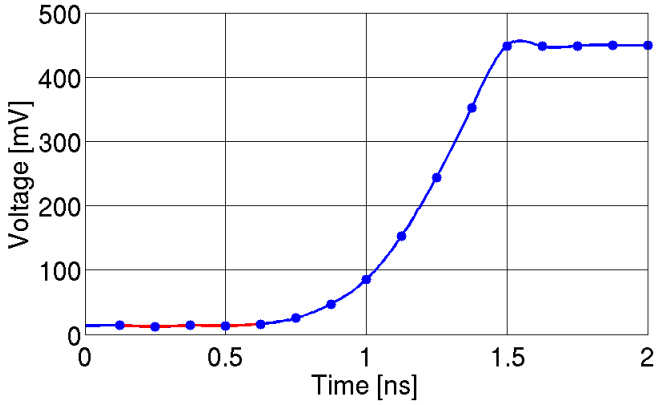

Figure 8.3: Typical pulse shape. Dots: digitizer sampled points; blue line: cubic spline interpolation; red line: 500 ps region used for baseline determination.

sis setup, shown in Fig.8.2. Timing spectra could then be set up as a function of the reconstructed position to investigate the time walk versus position-of-interaction.

To validate the position-of-interaction estimation for these events, the average photon distribution pattern as a function of the reconstructed position was set up. This distribution pattern $\{m_1, m_2, \ldots, m_{16}\}$ was calculated for each event by normalizing the SiPM detected energies e_i by the total detected energy as follows:

$$m_i = e_i / \sum_{i=j}^{16} e_j \tag{8.2}$$

here i is the SiPM index.

Events were sorted into 3D voxels of 2×2×1.5 mm^3 size according to the reconstructed position. For each voxel and each SiPM the m_i distribution was fitted by a Gaussian. The fitted centroid value was recorded and represented the average photon distribution at the SiPM location for the selected gamma position-of-interaction. For monolithic crystals one expects that the DOI correlates with the width of the scintillation distribution pattern at the sensor array.

8.2.3 Time pickoff methods

Fig. 8.3 shows a typical timing signal from the small crystal detector described in section 8.2.1. For all measurements the digitizer voltage range was set at a low value of 500 mV to minimize the digitizer noise level. This range corresponded to ∼12.5% of the pulse amplitude, such that all timing signals were clipping.

Since the lower part of the pulse rising edge corresponds to the earliest detected scintillation photons with associated minimal timing spread, no timing accuracy was lost by applying this procedure. To recover the detector signals from the sampled waveforms, a full cubic spline interpolation was performed. The baseline was determined for each interpolated timing signal by an averaging procedure on the interpolated signal right before the onset of the rising edge using a small time window of 500 ps. The baseline determination procedure is critical for obtaining good timing performance. By selecting a small time window right before the onset of the pulse, low-frequency noise (introduced by SiPM dark count pile-up) is effectively filtered out. High-frequency noise is filtered out by the digitizer 700 MHz anti-aliasing filter (section 8.2.1). Two time pickoff methods were used for the timing analysis.

The first method was the conventional leading edge (LE) method. The time pickoff was performed on the interpolated signal, using a constant trigger level with respect to the baseline.

The second method used a more systematic least square estimator [147], taking several sampled points on the rising edge into account. The rationale behind this procedure is that by basing the time estimation on several sampled points, the noise associated with each sampled point can be averaged out. An average noise-free pulse was set up by aligning multiple cubic spline-interpolated pulses according to the LE time pickoff at optimal trigger level. After subtracting the baseline for each individual pulse, the pulses were summed to form the average reference pulse $P(t_0)$. $P(t_0)$ was least square-fitted to each measured pulse and noise ensembles were subsequently set up by subtracting $P(t_0)$ from each cubic spline-interpolated pulse. The final estimation of the pulse time t_0 is based on the minimization of the least square sum expressed in the following matrix formalism:

$$\chi^2 = (Y - P(t_0))^T V(t_0)^{-1} (Y - P(t_0)) \tag{8.3}$$

where Y is the sampled pulse and $V(t_0)$ the covariance matrix containing the noise variances and covariances calculated from the noise ensembles, effectively representing the weights used in the minimization procedure.

8.3 Results and discussion

8.3.1 Timing performance of small crystal pixel setup

For the small crystal pixels, the two time pickoff methods gave the same timing resolution, indicating that the electronic noise contribution to the timing performance was negligible for the detector signals. Fig. 8.4 shows the obtained timing resolution using the LE time pickoff method at optimal trigger levels. The ^{22}Na

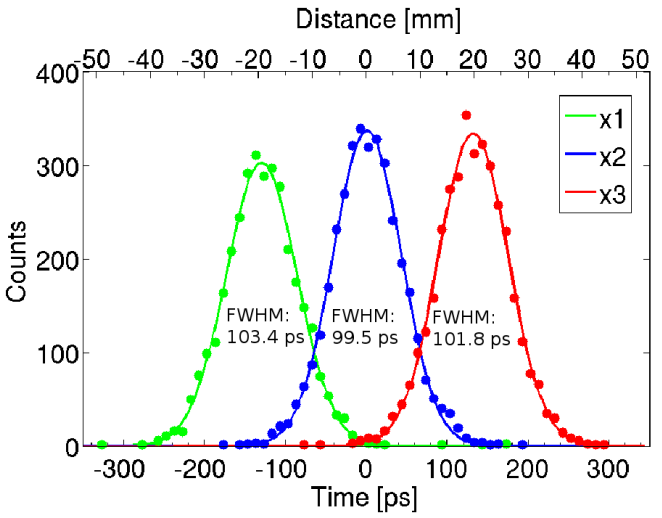

Figure 8.4: Timing spectra for relative source locations x_1 = 20 mm, x_2 = 0 mm and x_3 = -20 mm. Trigger levels were set at 150 mV. FWHM resolutions are 103.4 ± 1.4 ps, 99.5 ± 1.1 ps and 101.8 ± 1.4 ps, for x_1, x_2 and x_3 respectively.

source was placed at 3 different locations, separated by 20 mm. The timing spectrum shifts according to the gamma photon arrival time: $\Delta t = 2\Delta x/c$, without a significant change in timing resolution. An average coincidence timing resolution of 101 ± 2 ps FWHM was obtained, corresponding to a single detector timing resolution of 71 ps FWHM.

8.3.2 Timing performance of monolithic crystal setup

LE time pickoff was performed for the monolithic crystal setup. Fig. 8.5 shows the timing resolution obtained at optimal trigger levels. A coincidence timing resolution of 236.5 ps ± 0.5 ps FWHM was obtained. Subtracting the 71 ps resolution of the reference detector quadratically, this corresponds to a timing resolution for the monolithic crystal detector of 225 ps FWHM. Section 8.2.2 mentioned that the timing channel is effectively an analogue sum of the 16 SiPM energy signals. It thus contains the dark counts from each individual SiPM element and electronic noise from each associated preamplifier. Fig. 8.6 shows typical timing signals of the two detectors. Because the signal slope is smaller for the monolithic crystal detector compared to the reference detector (probably due to a bandwidth limitation in the electronic design, which shapes the timing signal), the increased dark count rate and electronic noise for the SiPM array timing channel have a bigger

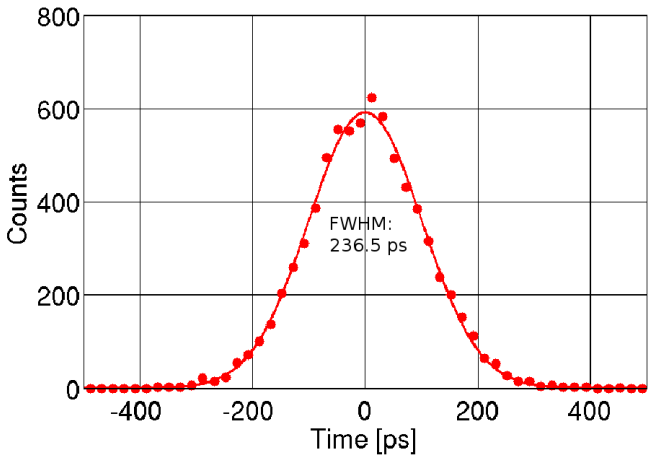

Figure 8.5: Timing spectrum for the monolithic crystal setup. Trigger levels were set at 50 mV for the monolithic crystal detector and 150 mV for the reference detector. FWHM resolution is 236.5 ± 0.5 ps. The centroid has been set at 0.

effect on the timing performance according to eq. 8.1. The timing resolution is currently probably limited by the large amount of dark counts and electronic noise for the SiPM array timing signal.

The 16 channel preamplifier is being redesigned to reduce the shaping of the timing channel. Additionally, alternatives to the current way of generating the timing signal are being looked at (e.g. a timing signal based on less channels; a time trigger for each individual channel).

8.3.3 Validation position-of-interaction estimation

Fig. 8.7 shows the Gaussian fitted centroids of m_i (see section 8.2.2) for each SiPM as a function of the reconstructed position for the timing analysis events. As mentioned in section 8.2.2, no prior knowledge on the scintillation photon distribution pattern was used to estimate the 3D position-of-interaction. When setting up the average patterns as a function of the reconstructed position, the expected behavior does show up: for positions-of-interaction near the photosensor array there is a high local flux of scintillation photons at the nearby SiPM location (resulting in a peaked distribution), while this flux is more uniform over the sensor array when the position is farther away from the sensor array (resulting in a more uniform distribution). This is a qualitative validation that the 3D reconstruction of the position-of-interaction is accurate for the events that were used for the timing analysis. Histogramming the reconstructed XY- and YZ-beam positions for the

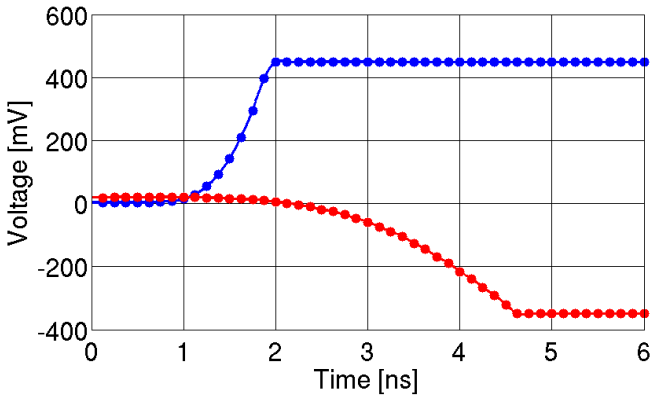

Figure 8.6: Typical timing signals. Blue line: timing signal reference detector. Red line: timing signal monolithic crystal detector.

events in the calibration setup and subsequently fitting them by Gaussians results in a 3D position resolution of ∼2.5 mm FWHM, degrading somewhat towards the crystal side surfaces and crystal surface opposite to the SiPM array.

It shows that, at least for the crystal thickness used in this work, monolithic scintillation crystals are suitable for accurate DOI-reconstruction using only one photosensor array. A block detector composed of crystal segments is not able to do this directly, since it confines the scintillation light in a single crystal segment and thus the correlation between DOI and scintillation photon distribution width at the sensor array is lost.

8.3.4 Time walk versus DOI

Having validated the position-of-interaction estimation in section 8.3.3, it is now possible to evaluate the arrival time versus the reconstructed DOI. Fig. 8.8 shows the result. It appears that the arrival time is fairly constant as a function of DOI.

This is in clear contrast to results reported for segmented crystals in a block detector. Moses and Derenzo reported that for 3×3×30 mm^3 LSO crystals arrival time variations between 100 ps and 200 ps were found for positions-of-interactions within a distance of 10 mm from the PMT, depending on the crystal surface treatment [89]. They attributed the effect to the scintillation light undergoing multiple reflections at quasi-random angles within the crystal, increasing the path length (variation). Shibuya et al. measured the arrival time variation for a four-layer DOI crystal array (8×8×4 crystal array of 2.9×2.9×7.5 mm^3 crystals of which one crystal was LYSO scintillator, the rest fused silica) [61]. By varying the location of the LYSO scintillator in the crystal array, they could measure arrival

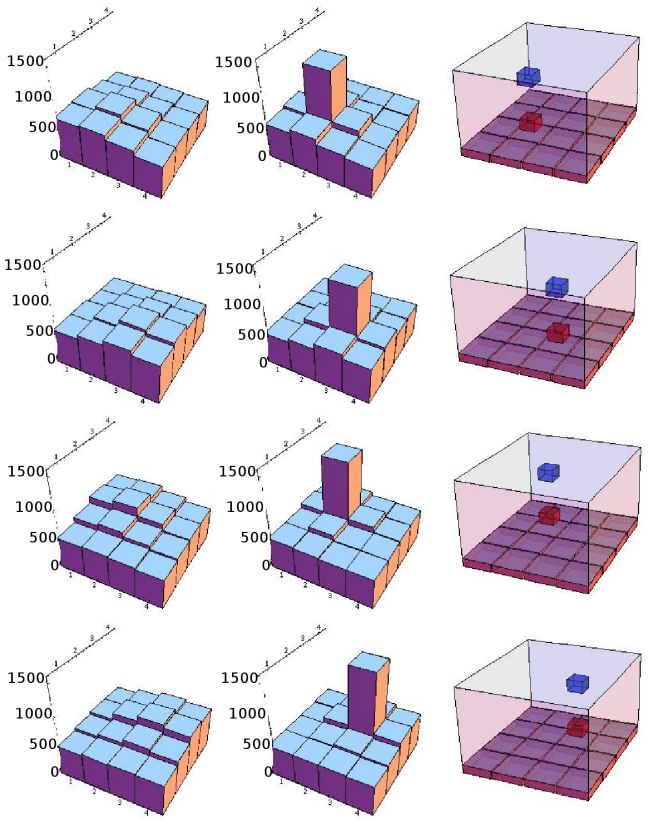

Figure 8.7: Average photon distribution patterns as a function of the reconstructed position, binned in 2×2×1.5 mm^3 voxels. The diagrams in the right column indicate the selected voxels. The blue voxels are at 8 mm distance from the photosensor array; the red voxels at 2 mm distance. The diagrams in the left column indicate the average photon distribution patterns, corresponding to the position-of-interaction region selected by the blue voxels. The diagrams in the center column indicate the patterns, corresponding to the region selected by the red voxels.

time variation versus DOI. They found an enhanced time variation, which they attributed to the complex optical structure of their crystal array.

Since the crystal side surfaces are at a larger distance for monolithic scintillation crystals, the scintillation photons undergo far less surface reflections compared to the segmented crystals. Scintillation photons travelling in the direction towards the sensor might even be largely unaffected by these reflections. This would result in a decrease of the path length (variation) for scintillation photons travelling in

a monolithic crystal, and thus a decrease in arrival time variation. Associated with the decrease in surface reflections is a decrease in surface absorptions (a crystal surface is never 100% reflective). This may lead to a higher light collection efficiency and thus less timing variance induced by the scintillator (the scintillator contribution to the timing resolution is inversely proportional to the square root of the number of primary photoelectrons [97], and thus to the light collection efficiency). These considerations imply that monolithic scintillation crystals are less affected by crystal surface absorptions and arrival time variation induced by the crystal geometry. When using large scintillator crystals for optimal sensitivity, monolithic scintillation crystals might have an intrinsically better timing performance compared to their segmented block crystal counterparts, and might thus in principle be better suitable for TOF-PET. It may well be that there is a larger arrival time variation for thicker (20-30 mm) $LaBr_3$:Ce monolithic scintillation crystals. Moses and Derenzo showed that for the 3×3×30 mm^3 LSO crystals the arrival time variation decreased to a large extent for distances greater than 20 mm from the PMT [89]. They attributed this effect to the proximity of the crystal surface opposite to the PMT: scintillation light emitted towards and away from the PMT merge in time because the path length variation decreases due to the nearby reflective crystal surface, increasing the early scintillation photon flux towards the sensor. This effect might also contribute to the flatness of the DOI arrival time line in Fig. 8.8, as the crystal thickness is only 10 mm.

In case there would be a larger arrival time variation for thicker monolithic scintillation crystals (or for slower crystals, like LYSO), thereby deteriorating the timing resolution, a time walk correction could be applied according to the estimated DOI. As shown before, the monolithic crystal provides DOI reconstruction without the necessity of incorporating complex optical structures, which often deteriorate the timing performance of block detectors.

Measurements with thicker monolithic $LaBr_3$:Ce and LYSO scintillation crystals have been planned.

8.4 Conclusion

We have shown that an excellent coincidence timing resolution of 101 ps FWHM can be achieved for bare 3×3×5 mm^3 $LaBr_3$:Ce crystals coupled to 3×3 mm^2 SiPMs. An initial timing performance characterization has been made for a monolithic $LaBr_3$:Ce crystal coupled to a 4×4 SiPM array. A single detector timing resolution of 225 ps FWHM was achieved. The timing performance of this detector is currently probably limited by the large dark count rate and electronic noise for the combined 16 SiPM signals. For the monolithic crystal the arrival time was fairly constant as a function of gamma position-of-interaction. From geometric

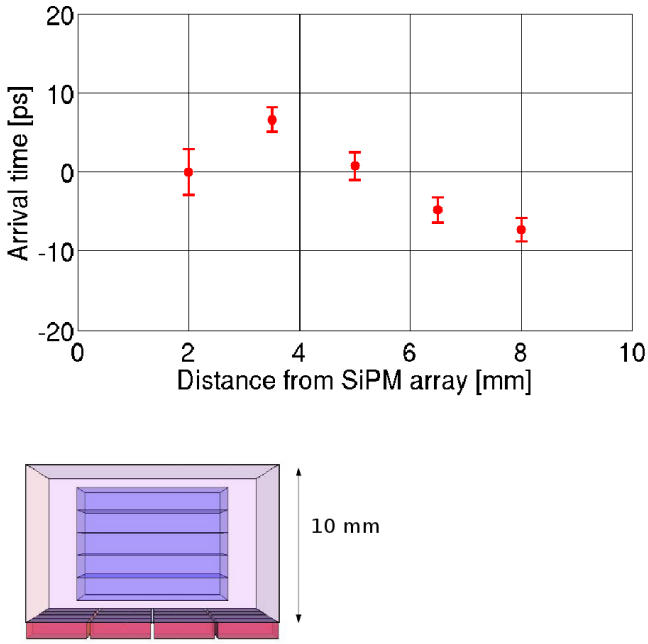

Figure 8.8: Center of coincidence timing distribution as a function of reconstructed distance from the SiPM array for the events in the timing analysis setup (Fig. 8.3). The diagram was generated by sorting the events according to the reconstructed position-of-interaction in 10×10×1.5 mm^3 voxels, indicated in the lower scheme of the detector. Error bars indicate the 1σ confidence bounds.

arguments, monolithic scintillation crystals may intrinsically be less affected by propagation time variation induced by the crystal geometry.

9 Discussion, outlook and valorization

9.1 Discussion

For high-quality PET images, PET detectors require high detection efficiency, high spatial, energy and timing resolution, and should provide full 3D information about the position of interaction. The last point implies that PET detectors should include the capability of determining the depth-of-interaction (DOI). Unfortunately, these performance parameters often impose conflicting design requirements. For example, high detection efficiency requires thick PET detectors. However, the positioning performance generally degrades with increasing thickness, due to increased scattering of the impinging gamma photons within the detector and, for monolithic scintillation crystals, due to an increasing spread of the scintillation light. High detection efficiency and high spatial resolution is an especially important design conflict for detectors that do not provide information about the DOI: As described in section 2.2.3, the parallax effect severely degrades the image spatial resolution in PET scanners when there is no DOI reconstruction ability, and this degradation worsens for thick detectors that have a large DOI spread.

This work concentrated on the analysis of the performance of monolithic scintillation crystals coupled to fast photosensor arrays for TOF-PET. A statistical reconstruction algorithm based on maximum likelihood estimation (MLE) was developed for estimating the position-of-interaction of gamma photons inside monolithic scintillation crystals (see chapter 4). For a $20 \times 20 \times 12$ mm^3 LYSO crystal coupled to a 4×4 MAPMT with 4.2×4.2 mm^2 anodes, a spatial resolution of 2.4 mm FWHM was achieved using this method.

As discussed in section 3.3.3, monolithic scintillation crystals inherently provide information about the DOI. Several authors have shown that the width of the scintillation light distribution at the photosensor array correlates with the DOI, e.g. [69, 148]. For optimal correlation, monolithic crystals are normally covered with absorptive black coatings to minimize the reflection of the scintillation light at the crystal surfaces. Scintillation photons that undergo multiple reflections lose the information about their position of origin and manifest themselves as background light, widening the spatial distribution of the scintillation light at the photosensor plane, and thus affecting the correlation with the DOI. However, the choice to minimize the reflection of the scintillation light at the crystal surfaces lowers the scintillation light collection efficiency and thus worsens the energy and timing resolution of the detector (see section 3.1). From Figs. 4.11 and 8.7, it is apparent

that the DOI correlates with the width of the light distribution, also for monolithic crystals covered with reflective coatings. The distribution patterns in Figs. 4.11 and 8.7 were obtained by histogramming the detector response according to the reconstructed 3D position-of-interaction. During the position reconstruction, no prior assumptions on the distribution patterns were used (see chapter 4), meaning that the observed correlation is a physical effect and not introduced by the position algorithm itself. Monolithic scintillation detectors can thus be optimized for energy and timing resolution with reflective coatings, while the 3D position-of-interaction of the gamma photons can still be reconstructed using a single photosensor array.

The DOI resolution could be estimated by reconstructing the beams entering the crystal from the side, at a defined distance from the photosensor array (Figs. 4.10 and 5.5). DOI resolutions between 2 mm and 5 mm were achieved for LYSO crystals coupled to a MAPMT array in chapters 4 and 5. The variation of the 3D position resolution (thus also DOI) with distance from the photosensor array results from the variation in the spread of the scintillation light, as discussed at the end of section 3.3.1 (specifically Eqs. 3.11 - 3.13). In chapter 5, it was shown that 3D position reconstruction was even possible for thick monolithic crystals with a cubical shape (with a thickness comparable to the transverse extension), coupled to a single photosensor array. Although the spatial resolution degrades with increasing thickness, it might still be at an acceptable level if maximum detection efficiency is required at minimal detector costs (using a single photosensor array to read out the crystal), e.g. for whole-body PET imaging. For monolithic crystals with a cubical shape, the position reconstruction near the crystal edges is however a challenging task, which needs further investigation. Since the majority of the impinging gamma photons interact at small DOI (due to the exponential attenuation law), the positioning performance of thick monolithic crystals should be improved by placing a semiconductor photosensor array on the front side of the crystal (facing the gamma beam), as discussed in chapter 5. Measurements with this readout geometry are being prepared.

Since the light collection efficiency was optimized for the monolithic crystals by using reflective coatings, good energy and timing performance was obtained. The energy resolution of $\sim$11% in chapters 4 and 5 is normal for LYSO. The timing resolution of 320-360 ps FWHM for the LYSO-MAPMT detector in coincidence with a BaF_2 detector (whereby the BaF_2 detector had a single detector timing resolution of $\sim$180 ps FWHM) translates into a single detector timing resolution of 265-312 ps FWHM for the LYSO-MAPMT detector (and a coincidence timing resolution of 374-441 ps FWHM for two such LYSO detectors). These timing resolutions were obtained by digital time pickoff algorithms, triggering on the early part of the rising edge of the timing pulses. Since the emission rate of scintillation photons is highest during the initial moments of the scintillation process, the arrival time variance is lowest for the photons that arrive at the photosensor during

the earliest stage, see [97] for a theoretical derivation. At the same time, the signal slope of the timing pulses is highest at the early part of the rising edge. Triggering on the early part minimizes the electronic noise contribution to the timing resolution. As shown by Eq. 8.1, the signal slope of the timing pulse determines the effect of the electronic noise on the timing resolution.

Chapter 4 presents a method to calibrate and correct for the arrival time variation with the position-of-interaction of the gamma photon. The observation that this arrival time variation with position-of-interaction can be considerable for scintillation crystals, was earlier shown by Moses and Derenzo [89], reporting arrival time variations with excitation depth between 200 and 400 ps for $3 \times 3 \times 30$ mm^3 LSO crystal segments, depending on the crystal surface treatment. Figs. 4.12, 8.8 and in particular 5.3 show that there is also an arrival time variation with position-of-interaction for monolithic crystals, but this variation is much smaller than was reported for the $3 \times 3 \times 30$ mm^3 LSO crystal in [89]. For the $16.2 \times 18 \times 20$ mm^3 LYSO crystal in Fig. 5.3, the arrival time variation with excitation depth was only about 70 ps. This is a very promising result. As discussed in section 8.3.4, it may well be that the scintillation light undergoes far less surface reflections and surface absorptions in monolithic crystals as compared to segmented crystals, due to the larger distance to the crystal side surfaces. This would result in a decrease in the path length (variation) and thus a decrease in arrival time variation. It was already discussed in section 3.3.1 that monolithic crystals may have a better light collection efficiency than segmented crystals, and thus a lower statistical spread in the arrival time of the scintillation photons at the photosensors. The apparently smaller arrival time variation with position-of-interaction for monolithic crystals further indicates that monolithic crystals are better suited for TOF-PET than segmented crystals.

In chapters 4 and 5, the timing resolution for the monolithic crystals could not significantly be improved by applying a position correction to the timing. In chapter 5, it was shown that there was virtually no arrival time variation with excitation depth near the crystal surface opposite to the photosensor plane, where most gamma interactions took place (due to the exponential attenuation law). This was attributed to the reflection of the scintillation light at the crystal surface, boosting the early arrival of scintillation photons at the sensor. It was discussed that the position correction to the timing might be interesting for monolithic crystals read out by a semiconductor photosensor array, facing the gamma beam (this configuration should improve the positioning performance, see discussion earlier in this section). As shown in Fig. 5.3, there is a considerable propagation time variation near the photosensor plane, and this is where most gamma interactions will take place for such a configuration. In this situation, a position correction to the timing might improve the timing resolution.

In chapter 6, the timing resolution of the SiPM sensor was tested. Single

photoelectron timing resolutions $\sigma_{t,spe}$ down to about 100 ps RMS were found for the 1 × 1 mm^2 Hamamatsu SiPM, whereby the timing resolution σ_t for multiple photoelectrons N_{phe} could be described by Poisson statistics ($\sigma_t = \sigma_{t,spe}/\sqrt{N_{phe}}$). In chapter 7, 3 × 3 × 5 mm^3 $LaBr_3$:Ce scintillators were coupled to 3 × 3 mm^2 SiPMs. For 511 keV gamma photons, excellent coincident timing resolutions of ∼100 ps FWHM were obtained, using low-noise and high-bandwidth preamplifiers and digital time pickoff, triggering on the early part of the rising edge of the timing pulses. This world-record timing performance indicates that SiPMs are well-suited for TOF-PET. For monolithic crystals read out by SiPM arrays, the scintillation light is shared over multiple SiPM elements. Each SiPM element introduces dark counts and each associated preamplifier introduces electronic noise. For optimal timing performance, the timing signal from the SiPM array needs to be based on a combination of the signals from the SiPM elements, and will thus contain the noise from multiple SiPM signals (there is no common 'dynode' signal available, as in a MAPMT, see section 3.2). From Eq. 8.1, it is clear that the noise performance needs to be as good as possible for the preamplifier that forms the timing signal from the SiPM array. In chapter 8, a single detector timing resolution of 225 ps FWHM was achieved for a 16.2 × 18 × 10 mm^3 $LaBr_3$:Ce(5%) crystal coupled to a 4 × 4 SiPM array with 3 × 3 mm^2 pixel size, whereby the timing signal was based on an analogue sum of the 16 SiPM output signals. This timing resolution was limited by the large amount of dark counts and electronic noise in the timing signal. It is expected that a preamplifier with an optimized noise performance will improve the timing resolution for this detector.

In this work, a TOF-PET detector concept based on monolithic scintillation crystals and fast photosensor arrays was characterized. It was shown that the 3D position-of-interaction (thus including DOI) could accurately be reconstructed with a single photosensor array coupled to the monolithic crystal. The light collection efficiency of monolithic crystals may be better than for segmented crystals, making them more suitable for TOF-PET. The costs of manufacturing are further much lower than for segmented crystals. With digital time pickoff algorithms, good timing performance was obtained. Due to their compactness and transparency to 511 keV gamma photons, SiPM arrays allow flexible readout geometries of the monolithic crystals. Because of the high gain and low transit time jitter, SiPMs have excellent timing performance and can be used for TOF-PET. They are further compatible with magnetic fields, which makes them possible candidates for PET-MRI integrated systems.

9.2 Outlook and valorization

In the near future, thick monolithic crystals will be used with front and double-sided readout by SiPM arrays, using a redesigned multichannel preamplifier optimized for noise and bandwidth. With this preamplifier, it is expected that single detector timing resolutions below 200 ps FWHM (and thus coincidence timing resolutions below 300 ps FWHM) can be achieved for monolithic $LaBr_3$-SiPM detectors. With this preamplifier, the timing performance of monolithic LYSO-SiPM detectors is also expected to be optimized. The position reconstruction near the crystal edges will be investigated further for these detectors.

The TOF-PET detector concept described in this work is interesting for whole-body PET imaging, whereby the excellent timing resolution enables PET images with a very high signal-to-noise ratio. In addition, the developed position-of-interaction algorithm is capable to accurately measure depth-of-interaction (DOI), making sure that there is no parallax degradation, such that the image resolution is optimized over the entire field-of-view (FOV). The absence of parallax degradation also enables the construction of PET systems with detector rings with a reduced diameter (comparable to the transaxial FOV), thereby reducing detector costs (because less detector material is needed), increasing the system sensitivity (more solid angle coverage) and reducing the position blurring associated with the acollinearity (Eq. 2.1). No crystal segmentation procedure is required for this detector concept, while no detector modifications are necessary to enable DOI measurement, such that the costs for the detector parts are significantly reduced compared to the current PET detector technology in commercial scanners. In addition, field-programmable gate arrays (FPGAs) and application-specific integrated circuits (ASICs) allow advanced signal processing at affordable costs and in reasonable time. Further, when using SiPMs for reading out the scintillation light, simultaneous PET-MRI imaging is possible, since SiPMs are insensitive to magnetic fields. This detector concept has the potential to significantly improve PET's ability to visualize, quantify and characterize disease. This could lead to an earlier diagnosis of cancer, which is essential for an effective cancer therapy.

This detector concept is also interesting for applications involving a small FOV. Dedicated, small detectors for imaging certain organs in close proximity should give superior spatial resolution and signal-to-noise ratio compared to that attainable with whole-body imaging, because of the smaller distance to the detectors. Examples include imagers for the head and neck region, and mammography. Another example is radioguided surgery using intraoperative PET. Here, the PET detectors enable real-time tumor localization and help the surgeon to verify complete resection of the tumor. Since the FOV is much smaller, it is even more important that the DOI of the gamma photons is reconstructed properly in the detectors, as compared to whole-body imaging. Since the detector concept in this work can

be very compact (especially when using SiPM arrays) and is able to accurately reconstruct the DOI, it may also be interesting for these small FOV applications. In addition, because of the excellent timing resolution, these applications may also benefit from the TOF-PET technique.

Bibliography

[1] P. Cassidy and G. Radda, "Molecular imaging perspectives," *J. R. Soc. Interf.*, vol. 2, no. 3, pp. 133–144, 2005.

[2] A. Rahmim and H. Zaidi, "PET versus SPECT: strengths, limitations and challenges," *Nucl. Med. Comm.*, vol. 29, no. 3, pp. 193–207, 2008.

[3] M. MacManus, U. Nestle, K. E. Rosenzweig, I. Carrio, C. Messa, O. Belohlavek, M. Danna, T. Inoue, E. Deniaud-Alexandre, S. Schipani, N. Watanabe, M. Dondi, and B. Jeremic, "Use of PET and PET/CT for Radiation Therapy Planning: IAEA expert report 2006-2007," *Radiotherapy and oncology*, vol. 91, no. 1, pp. 85–94, 2009.

[4] D. Papathanassiou, C. Bruna-Muraille, J.-C. Liehn, T. D. Nguyen, and H. Cure, "Positron Emission Tomography in oncology: Present and future of PET and PET/CT," *Crit. Rev. in Onc. Hem.*, vol. 72, no. 3, pp. 239–254, 2009.

[5] D. Le Guludec, R. Lautamaki, J. Knuuti, J. J. Bax, F. M. Bengel, and European Council Nucl Cardiology, "Present and future of clinical cardiovascular PET imaging in Europe - a position statement by the European Council of Nuclear Cardiology (ECNC)," *Eur. J. Nucl. Med. Mol. Imag.*, vol. 35, no. 9, pp. 1709–1724, 2008.

[6] W. W. Moses, "Time of flight in PET revisited," *IEEE Trans. Nucl. Sci.*, vol. 50, pp. 1325–1330, Oct. 2003.

[7] C. Lois, B. W. Jakoby, M. J. Long, K. F. Hubner, D. W. Barker, M. E. Casey, M. Conti, V. Y. Panin, D. J. Kadrmas, and D. W. Townsend, "An Assessment of the Impact of Incorporating Time-of-Flight Information into Clinical PET/CT Imaging," *J. Nucl. Med.*, vol. 51, no. 2, pp. 237–245, 2010.

[8] J. S. Karp, S. Surti, M. E. Daube-Witherspoon, and G. Muehllehner, "Benefit of time-of-flight in PET: Experimental and clinical results," *J. Nucl. Med.*, vol. 49, no. 3, pp. 462–470, 2008.

[9] S. C. Pevovar, M. H. Weber, and K. G. Lynn, "Ratio of positron annihilation into three photons versus two," in *Physica Status Solidi C - Current Topics in Solid State Physics, Vol 4, No 10*, vol. 4, pp. 3447–3450, 2007.

[10] R. Lecomte, "Novel detector technology for clinical PET," *Eur. J. Nucl. Med. Mol. Imaging*, vol. 36, no. Suppl. 1, pp. 69–85, 2009.

[11] http://ie.lbl.gov/interact/anfl.pdf.

[12] S. R. Cherry, J. A. Sorenson, and M. E. Phelps, *Physics in Nuclear Medicine*. 3rd ed. Saunders, 2003.

[13] J. Humm, A. Rosenfeld, and A. Del Guerra, "From PET detectors to PET scanners," *Eur. J. Nucl. Med. Mol. Imaging*, vol. 30, no. 11, pp. 1574–1597, 2003.

[14] S. R. Cherry, "The 2006 Henry N. Wagner lecture: Of mice and men (and positrons) - Advances in PET imaging technology," *J. Nucl. Med.*, vol. 47, no. 11, pp. 1735–1745, 2006.

[15] V. Panin, F. Kehren, C. Michel, and M. Casey, "Fully 3-D PET reconstruction with system matrix derived from point source measurements," *IEEE Trans. Med. Imaging*, vol. 25, pp. 907–921, JUL 2006.

[16] B. W. Jakoby, Y. Bercier, C. C. Watson, B. Bendriem, and D. W. Townsend, "Performance Characteristics of a New LSO PET/CT Scanner With Extended Axial Field-of-View and PSF Reconstruction," *IEEE Trans. Nucl. Sci.*, vol. 56, pp. 633–639, JUN 2009.

[17] T. K. Lewellen, "The Challenge of Detector Designs for PET," *Am. J. Roentgenol*, vol. 195, no. 2, pp. 301–309, 2010.

[18] G. F. Knoll, *Radiation Detection and Measurement*. Wiley, 3rd edition, 2000.

[19] D. L. Bailey, *Positron emission tomography: basic sciences*. Springer, 2005.

[20] H. Zaidi and K. Koral, "Scatter modelling and compensation in emission tomography," *Eur. J. Nucl. Med. Mol. Imaging*, vol. 31, no. 5, pp. 761–782, 2004.

[21] G. B. Saha, *Basics of PET imaging: physics, chemistry, and regulations*. Springer, 2004.

[22] S. Strother, M. Casey, and E. Hoffman, "Measuring PET scanner sensitivity - relating countrates to image signal-to-noise ratios using noise equivalent counts," *IEEE Trans. Nucl. Sci.*, vol. 37, no. 2, Part 1, pp. 783–788, 1990.

[23] B. J. Pichler, A. Kolb, T. Naegele, and H.-P. Schlemmer, "PET/MRI: Paving the Way for the Next Generation of Clinical Multimodality Imaging Applications," *J. Nucl. Med.*, vol. 51, no. 3, pp. 333–336, 2010.

[24] H.-P. W. Schlemmer, B. J. Pichler, M. Schmand, Z. Burbar, C. Michel, R. Ladebeck, K. Jattke, D. Townsend, C. Nahmias, P. K. Jacob, W.-D. Heiss, and C. D. Claussen, "Simultaneous MR/PET imaging of the human brain: Feasibility study," *Radiology*, vol. 248, no. 3, pp. 1028–1035, 2008.

[25] C. van Eijk, "Inorganic scintillators in medical imaging," *Phys. Med. Biol.*, vol. 47, no. 8, pp. R85–R106, 2002.

[26] Y. P. Shao, "A new timing model for calculating the intrinsic timing resolution of a scintillator detector," *Phys. Med. Biol.*, vol. 52, pp. 1103–1117, Feb. 2007.

[27] M. A. Spurrier, P. Szupryczynski, K. Yang, A. A. Carey, and C. L. Melcher, "Effects of Ca^{2+} co-doping on the scintillation properties of LSO:Ce," *IEEE Trans. Nucl. Sci.*, vol. 55, no. 3, Part 2, pp. 1178–1182, 2008.

[28] A. Lempicki and J. Glodo, "Ce-doped scintillators: LSO and LuAP," *Nucl. Instr. and Meth. A*, vol. 416, no. 2-3, pp. 333 – 344, 1998.

[29] A. Petrosyan, M. Derdzyan, K. Ovanesyan, P. Lecoq, E. Auffray, J. Trummer, M. Kronberger, C. Pedrini, C. Dujardin, and P. Anfre, "Properties of luap:ce scintillator containing intentional impurities," *Nucl. Instr. and Meth. A*, vol. 571, no. 1-2, pp. 325 – 328, 2007.

[30] E. van Loef, P. Dorenbos, C. van Eijk, K. Kramer, and H. Gudel, "High-energy-resolution scintillator: Ce^{3+} activated $LaBr_3$," *Appl. Phys. Letters*, vol. 79, no. 10, pp. 1573–1575, 2001.

[31] D. Renker, "Photosensors," *Nucl. Instr. and Meth. A*, vol. 527, no. 1-2, pp. 15–20, 2004.

[32] *Photomultiplier Tubes: Basics and Applications (Second Edition).* Hamamatsu Photonics, 2006.

[33] *High QE PMT Catalog.* Hamamatsu Photonics, 2007.

[34] *Microchannel Plate - Photomultiplier Tube (MCP-PMTs) R3809U-50 series.* Hamamatsu Photonics. Specification sheet.

[35] D. Renker, "Properties of avalanche photodiodes for applications in high energy physics, astrophysics and medical imaging," *Nucl. Instr. and Meth. A*, vol. 486, no. 1-2, pp. 164–169, 2002.

[36] P. Webb, R. Mcintyre, and J. Conradi, "Properties of avalanche photodiodes," *RCA Rev.*, vol. 35, no. 2, pp. 234–278, 1974.

[37] M. C. Maas, D. R. Schaart, D. J. J. van der Laan, P. Bruyndonckx, C. Lemaitre, F. J. Beekman, and C. W. E. van Eijk, "Monolithic scintillator PET detectors with intrinsic depth-of-interaction correction," *Phys. Med. Biol.*, vol. 54, no. 7, pp. 1893–1908, 2009.

[38] M. C. Maas, D. J. van der Laan, D. R. Schaart, J. Huizenga, J. C. Brouwer, P. Bruyndonckx, S. Leonard, C. Lemaitre, and C. W. E. van Eijk, "Experimental characterization of monolithic-crystal small animal PET detectors read out by APD arrays," *IEEE Trans. Nucl. Sci.*, vol. 53, no. 3, pp. 1071–1077, 2006.

[39] K. Shah, R. Farrell, R. Grazioso, E. Harmon, and E. Karplus, "Position-sensitive avalanche photodiodes for gamma-ray imaging," *IEEE Trans. Nucl. Sci.*, vol. 49, no. 4, Part 1, pp. 1687–1692, 2002.

[40] C. Levin, A. Foudray, P. Olcott, and F. Habte, "Investigation of position sensitive avalanche photodiodes for a new high-resolution PET detector design," *IEEE Trans. Nucl. Sci.*, vol. 51, no. 3, Part 2, pp. 805–810, 2004.

[41] J. Zhang, P. D. Olcott, and C. S. Levin, "A new positioning algorithm for position-sensitive avalanche photodiodes," *IEEE Trans. Nucl. Sci.*, vol. 54, no. 3, Part 1, pp. 433–437, 2007.

[42] T. K. Lewellen, "Recent developments in PET detector technology," *Phys. Med. Biol.*, vol. 53, no. 17, pp. R287–R317, 2008.

[43] D. Renker and E. Lorenz, "Advances in solid state photon detectors," *Journal of Instrumentation*, vol. 4, no. 04, p. P04004, 2009.

[44] C. Degenhardt, G. Prescher, T. Frach, A. Thon, R. de Gruyter, A. Schmitz, and R. Ballizany, "The digital silicon photomultiplier - a novel sensor for the detection of scintillation light," in *2009 IEEE Nucl. Sci. Symp. Conf. Record*, pp. 2383 –2386, 2009.

[45] T. Frach, G. Prescher, C. Degenhardt, R. de Gruyter, A. Schmitz, and R. Ballizany, "The digital silicon photomultiplier - principle of operation and intrinsic detector performance," in *2009 IEEE Nucl. Sci. Symp. Conf. Record*, pp. 1959 –1965, 2009.

[46] M. Casey and R. Nutt, "A multicrystal 2-dimensional BGO detector system for positron emission tomography," *IEEE Trans. Nucl. Sci.*, vol. 33, no. 1, pp. 460–463, 1986.

[47] H. Anger, "Scintillation camera," *Rev. Sci. Instr.*, vol. 29, no. 1, pp. 27–33, 1958.

[48] P. Bruyndonckx, C. Lemaitre, D. Schaart, M. Maas, D. J. van der Laan, M. Krieguer, O. Devroede, and S. Tavernier, "Towards a continuous crystal APD-based PET detector design," *Nucl. Instr. and Meth. A*, vol. 571, no. 1-2, pp. 182–186, 2007.

[49] T. Ling, T. H. Burnett, T. K. Lewellen, and R. S. Miyaoka, "Parametric positioning of a continuous crystal PET detector with depth of interaction decoding," *Phys. Med. Biol.*, vol. 53, no. 7, pp. 1843–1863, 2008.

[50] C. Lerche, A. Ros, J. Monzó, R. Aliaga, N. Ferrando, J. Martínez, V. Herrero, R. Esteve, R. Gadea, R. Colom, J. Toledo, F. Mateo, A. Sebastiá, F. Sánchez, and J. Benlloch, "Maximum likelihood positioning for gamma-ray imaging detectors with depth of interaction measurement," *Nucl. Instr. and Meth. A*, vol. 604, no. 1-2, pp. 359 – 362, 2009.

[51] S. Surti, A. Kuhn, M. E. Werner, A. E. Perkins, J. Kolthammer, and J. S. Karp, "Performance of philips gemini TF PET/CT scanner with special consideration for its time-of-flight imaging capabilities," *J. Nucl. Med.*, vol. 48, no. 3, pp. 471–480, 2007.

[52] J. Joung, R. Miyaoka, S. Kohlmyer, and T. Lewellen, "Implementation of ML based positioning algorithms for scintillation cameras," *IEEE Trans. Nucl. Sci.*, vol. 47, no. 3, pp. 1104–1111, 2000.

[53] C. W. Lerche, *Depth of Interaction Enhanced Gamma-Ray Imaging for Medical Applications*. PhD thesis, 2006.

[54] A. Bolozdynya, C. Ordonez, and W. Chang, "A concept of cylindrical Compton camera for SPECT," in *Nuclear Science Symposium, 1997. IEEE*, vol. 2, pp. 1047 –1051 vol.2, 1997.

[55] Y. H. Chung, Y. Choi, G. Cho, Y. S. Choe, K.-H. Lee, and B.-T. Kim, "Characterization of dual layer phoswich detector performance for small animal PET using Monte Carlo simulation," *Phys. Med. Biol.*, vol. 49, no. 13, p. 2881, 2004.

[56] J. H. Jung, Y. Choi, Y. H. Chung, O. Devroede, M. Krieguer, P. Bruyndonckx, and S. Tavernier, "Optimization of LSO/LuYAP phoswich detector for small animal PET," *Nucl. Instr. and Meth. A*, vol. 571, no. 3, pp. 669 – 675, 2007.

[57] F. Bauer, M. Aykac, L. Eriksson, and M. Schmand, "Depth of Interaction With a 3-Dimensional Checkerboard Arrangement LSO-LSO Block," *IEEE Trans. Nucl. Sci.*, vol. 57, no. 3, Part 1, pp. 971–975, 2010.

[58] Y. Shao, H. Li, and K. Gao, "Initial experimental studies of using solid-state photomultiplier for PET applications," *Nucl. Instr. and Meth. A*, vol. 580, no. 2, pp. 944 – 950, 2007.

[59] Y. Yang, Y. Wu, J. Qi, S. St. James, H. Du, P. A. Dokhale, K. S. Shah, R. Farrell, and S. R. Cherry, "A Prototype PET Scanner with DOI-Encoding Detectors," *J Nucl Med*, vol. 49, no. 7, pp. 1132–1140, 2008.

[60] T. Tsuda, H. Murayama, K. Kitamura, N. Inadama, T. Yamaya, E. Yoshida, F. Nishikido, M. Hamamoto, H. Kawai, and Y. Ono, "Performance evaluation of a subset of a four-layer LSO detector for a small animal DOI PET scanner: jPET-RD," *IEEE Trans. Nucl. Sci.*, vol. 53, no. 1, Part 1, pp. 35–39, 2006.

[61] K. Shibuya, F. Nishikido, T. Tsuda, T. Kobayashi, C. Lam, T. Yamaya, E. Yoshida, N. Inadama, and H. Murayama, "Timing resolution improvement using DOI information in a four-layer scintillation detector for TOF-PET," *Nucl. Instr. and Meth. A*, vol. 593, no. 3, pp. 572–577, 2008.

[62] R. Miyaoka, T. Lewellen, J. Yu, and D. McDaniel, "Design of a depth of interaction (DOI) PET detector module," *IEEE Trans. Nucl. Sci.*, vol. 45, no. 3, Part 2, pp. 1069–1073, 1998.

[63] J. Zhang, A. M. K. Foudray, P. D. Cott, R. Farrell, K. Shah, and C. S. Levin, "Performance characterization of a novel thin position-sensitive avalanche photodiode for 1 mm resolution positron emission tomography," *IEEE Trans. Nucl. Sci.*, vol. 54, no. 3, Part 1, pp. 415–421, 2007.

[64] R. Vinke, H. Löhner, D. Schaart, H. van Dam, S. Seifert, F. Beekman, and P. Dendooven, "Time walk correction for TOF-PET detectors based on a monolithic scintillation crystal coupled to a photosensor array," *Nucl. Instr. and Meth. A*, vol. 621, no. 1-3, pp. 595 – 604, 2010.

[65] J. Joung, R. S. Miyaoka, and T. K. Lewellen, "cMiCE: a high resolution animal PET using continuous LSO with a statistics based positioning scheme," *Nucl. Instr. and Meth. A*, vol. 489, no. 1-3, pp. 584 – 598, 2002.

[66] P. Bruyndonckx, S. Leonard, S. Tavernier, C. Lemaitre, O. Devroede, Y. Wu, and M. Krieguer, "Neural network-based position estimators for PET detectors using monolithic LSO blocks," *IEEE Trans. Nucl. Sci.*, vol. 51, no. 5, Part 2, pp. 2520–2525, 2004.

[67] T. Ling, T. K. Lewellen, and R. S. Miyaoka, "Depth of interaction decoding of a continuous crystal detector module," *Phys. Med. Biol.*, vol. 52, no. 8, pp. 2213–2228, 2007.

[68] S. Y. Moore, W. C. J. Hunter, L. R. Furenlid, and H. H. Barrett, "Maximum-likelihood estimation of 3D event position in monolithic scintillation crystals: Experimental results," in *2007 IEEE Nucl. Sci. Symp. Conf. Record, vols 1-11*, pp. 3691–3694, 2007.

[69] C. W. Lerche, M. Doering, A. Ros, V. Herrero, R. Gadea, R. J. Aliaga, R. Colom, F. Mateo, J. M. Monzo, N. Ferrando, J. F. Toledo, J. D. Martinez, A. Sebastia, F. Sanchez, and J. M. Benlloch, "Depth of interaction detection for gamma-ray imaging," *Nucl. Instr. and Meth. A*, vol. 600, no. 3, pp. 624–634, 2009.

[70] K. Ishii, Y. Kikuchi, S. Matsuyama, Y. Kanai, K. Kotani, T. Ito, H. Yamazaki, Y. Funaki, R. Iwata, M. Itoh, K. Yanai, J. Hatazawa, N. Itoh, N. Tanizaki, D. Amano, M. Yamada, and T. Yamaguchi, "First achievement of less than 1 mm FWHM resolution in practical semiconductor animal PET scanner," *Nucl. Instr. and Meth. A*, vol. 576, no. 2-3, pp. 435 – 440, 2007.

[71] A. Drezet, O. Monnet, F. Mathy, G. Montemont, and L. Verger, "CdZnTe detectors for small field of view positron emission tomographic imaging," *Nucl. Instr. and Meth. A*, vol. 571, no. 1-2, pp. 465–470, 2007.

[72] G. Pratx and C. S. Levin, "Bayesian reconstruction of photon interaction sequences for high-resolution PET detectors," *Phys. Med. Biol.*, vol. 54, no. 17, pp. 5073–5094, 2009.

[73] P. Vaska, A. Bolotnikov, G. Carini, G. Camarda, J. F. Pratte, F. A. Dilmanian, S. J. Park, and R. B. James, "Studies of CZT for PET applications," in *2005 IEEE Nucl. Sci. Symp. Conf. Record, Vols 1-5*, pp. 2799–2802, 2005.

[74] N. Yanagita, Y. Morimoto, T. Ishitsu, A. Suzuki, W. Takeuchi, T. Seino, I. Takahashi, Y. Ueno, K. Amemiya, S. Inoue, M. Suzuki, F. Kozawa, N. Kubo, and N. Tamaki, "Physical performance of a prototype 3D PET scanner using CdTe detectors," in *2007 IEEE Nucl. Sci. Symp. Conf. Record, Vols 1-11*, pp. 2665–2668, 2007.

[75] T. Shiga, Y. Morimoto, N. Kubo, N. Katoh, C. Katoh, W. Takeuchi, R. Usui, K. Hirata, S. Kojima, K. Umegaki, H. Shirato, and N. Tamaki, "A New PET Scanner with Semiconductor Detectors Enables Better Identification of Intratumoral Inhomogeneity," *J Nucl Med*, vol. 50, no. 1, pp. 148–155, 2009.

[76] R. Ott, L. White, N. Evans, and A. Jeavons, "A Study of the Application of MWPC-Based Positron Cameras for Breast Imaging," in *2006 IEEE Nucl. Sci. Symp. Conf. Record*, vol. 5, pp. 2944 –2947, 2006.

[77] J. Missimer, Z. Madi, M. Honer, C. Keller, A. Schubiger, and S.-M. Ametamey, "Performance evaluation of the 16-module quad-HIDAC small animal PET camera," *Phys. Med. Biol.*, vol. 49, no. 10, p. 2069, 2004.

[78] A. Blanco, N. Carolino, C. M. B. A. Correia, L. Fazendeiro, N. C. Ferreira, M. F. Ferreira Marques, R. Ferreira Marques, P. Fonte, C. Gil, and M. P. Macedo, "RPC-PET: A new very high resolution PET technology," *IEEE Trans. Nucl. Sci.*, vol. 53, no. 5, Part 1, pp. 2489–2494, 2006.

[79] A. Jeavons, R. Chandler, and C. Dettmar, "A 3D HIDAC-PET camera with sub-millimetre resolution for imaging small animals," *IEEE Trans. Nucl. Sci.*, vol. 46, pp. 468–473, JUN 1999.

[80] A. Blanco, V. Chepel, R. Ferreira-Marques, P. Fonte, M. Lopes, V. Peskov, and A. Policarpo, "Perspectives for positron emission tomography with RPCs," *Nucl. Instr. and Meth. A*, vol. 508, no. 1-2, pp. 88–93, 2003.

[81] E. Aprile, K. L. Giboni, P. Majewski, K. Ni, and M. Yamashita, "Observation of anticorrelation between scintillation and ionization for MeV gamma rays in liquid xenon," *Phys. Rev. B*, vol. 76, no. 1, 2007.

[82] P. Amaudruz, D. Bryman, L. Kurchaninov, P. Lu, C. Marshall, J. P. Martin, A. Muennich, F. Retiere, and A. Sher, "Simultaneous reconstruction of scintillation light and ionization charge produced by 511 keV photons in liquid xenon: Potential application to PET," *Nucl. Instr. and Meth. A*, vol. 607, no. 3, pp. 668–676, 2009.

[83] D. J. van der Laan, M. C. Maas, H. W. A. M. de Jong, D. R. Schaart, P. Bruyndonckx, C. Lemaitre, and C. W. E. van Eijk, "Simulated performance of a small-animal PET scanner based on monolithic scintillation detectors," *Nucl. Instr. and Meth. A*, vol. 571, no. 1-2, pp. 227–230, 2007.

[84] P. Bruyndonckx, L. Zhi, C. Lemaitre, J. M. Perez, P. Rato, D. Schaart, M. Maas, D. J. Van der Laan, S. Tavernier, and W. Yonggang, "Impact of instrumentation parameters on the performance of neural network based positioning algorithms for monolithic scintillator blocks," in *2007 IEEE Nucl. Sci. Symp. Conf. Record, Vols 1-11*, pp. 4266–4270, 2007.

[85] S. Tavernier, P. Bruyndonckx, S. Leonard, and O. Devroede, "A high-resolution PET detector based on continuous scintillators," *Nucl. Instr. and Meth. A*, vol. 537, no. 1-2, pp. 321 – 325, 2005.

[86] D. R. Schaart, H. T. van Dam, S. Seifert, R. Vinke, P. Dendooven, H. Löhner, and F. J. Beekman, "A novel, SiPM-array-based, monolithic scintillator detector for PET," *Phys. Med. Biol.*, vol. 54, no. 11, pp. 3501–3512, 2009.

[87] Dow Corning Corporation, www.dowcorning.com.

[88] Labsphere Corporation, www.labsphere.com.

[89] W. W. Moses and S. E. Derenzo, "Prospects for time-of-flight PET using LSO scintillator," *IEEE Trans. Nucl. Sci.*, vol. 46, no. 3, pp. 474–478, 1999.

[90] R. Vinke, S. Seifert, D. Schaart, F. Schreuder, M. de Boer, H. van Dam, F. Beekman, H. Löhner, and P. Dendooven, "Optimization of digital time pickoff methods for $LaBr_3$-SiPM TOF-PET detectors," in *2009 IEEE Nucl. Sci. Symp. Conf. Record*, pp. 2962 –2968, 2009.

[91] T. Lewellen, "Time-of-Flight PET," *Seminars in Nucl. Med.*, vol. 28, no. 3, pp. 268–275, 1998.

[92] An overview of the most recent developments can be found in e.g. the Proceedings of the IEEE NSS/MIC conferences (www.nss-mic.org).

[93] G. Collazuol, G. Ambrosi, M. Boscardin, F. Corsi, G. F. Dalla Betta, A. Del Guerra, N. Dinu, M. Galimberti, D. Giulietti, L. A. Gizzi, L. Labate, G. Llosa, S. Marcatili, F. Morsani, C. Piemonte, A. Pozza, L. Zaccarelli, and N. Zorzi, "Single photon timing resolution and detection efficiency of the IRST silicon photo-multipliers," *Nucl. Instr. and Meth. A*, vol. 581, pp. 461–464, Oct. 2007.

[94] M. S. Judenhofer, H. F. Wehrl, D. F. Newport, C. Catana, S. B. Siegel, M. Becker, A. Thielscher, M. Kneilling, M. P. Lichy, M. Eichner, K. Klingel, G. Reischl, S. Widmaier, M. Roecken, R. E. Nutt, H.-J. Machulla, K. Uludag, S. R. Cherry, C. D. Claussen, and B. J. Pichler, "Simultaneous PET-MRI: a new approach for functional and morphological imaging," *Nature Medicine*, vol. 14, no. 4, pp. 459–465, 2008.

[95] L. Bardelli, G. Poggi, M. Bini, G. Pasquali, and N. Taccetti, "Time measurements by means of digital sampling techniques: a study case of 100 ps FWHM time resolution with a 100 MSample/s, 12 bit digitizer," *Nucl. Instr. and Meth. A*, vol. 521, pp. 480–492, Apr. 2004.

[96] T. Wilmshurst, *Signal recovery from noise in electronic instrumentation.* A. Hilger Publ., 1985.

[97] R. F. Post and L. I. Schiff, "Statistical limitations on the resolving time of a scintillation counter," *Phys. Rev.*, vol. 80, no. 6, pp. 1113–1113, 1950.

[98] D. J. Kadrmas, M. E. Casey, M. Conti, B. W. Jakoby, C. Lois, and D. W. Townsend, "Impact of Time-of-Flight on PET Tumor Detection," *J. Nucl. Med.*, vol. 50, no. 8, pp. 1315–1323, 2009.

[99] W. W. Moses, "Recent advances and future advances in time-of-flight PET," *Nucl. Instr. and Meth. A*, vol. 580, no. 2, pp. 919 – 924, 2007.

[100] G. Muehllehner and J. S. Karp, "Positron emission tomography," *Phys. Med. Biol.*, vol. 51, no. 13, pp. R117–R137, 2006.

[101] A. Kuhn, S. Surti, J. Karp, G. Muehllehner, F. Newcomer, and R. VanBerg, "Performance assessment of pixelated $LaBr_3$ detector modules for time-of-flight PET," *IEEE Trans. Nucl. Sci.*, vol. 53, no. 3, Part 2, pp. 1090–1095, 2006.

[102] G. Bizarri and P. Dorenbos, "Charge carrier and exciton dynamics in $LaBr_3$:Ce^{3+} scintillators: Experiment and model," *Phys. Rev. B*, vol. 75, no. 18, 2007.

[103] J. de Haas and P. Dorenbos, "Advances in yield calibration of scintillators," *IEEE Trans. Nucl. Sci.*, vol. 55, no. 3, pp. 1086 –1092, 2008.

[104] W. Drozdowski, P. Dorenbos, A. J. J. Bos, J. T. M. de Haas, S. Kraft, E. Maddox, A. Owens, F. G. A. Quarati, C. Dathy, and V. Ouspenski, "Effect of proton dose, crystal size, and cerium concentration on scintillation yield and energy resolution of $LaBr_3$:Ce," *IEEE Trans. Nucl. Sci.*, vol. 54, no. 3, Part 2, pp. 736–740, 2007.

[105] W. Higgins, J. Glodo, E. Van Loef, M. Klugerman, T. Gupta, L. Cirignano, P. Wong, and K. Shah, "Bridgman growth of $LaBr_3$:Ce and $LaCl_3$:Ce crystals for high-resolution gamma-ray spectrometers," *J. Cryst. Growth*, vol. 287, no. 2, pp. 239–242, 2006.

[106] A. Kuhn, S. Surti, K. S. Shah, and J. S. Karp, "Investigation of $LaBr_3$ detector timing resolution," in *2005 IEEE Nucl. Sci. Symp. Conf. Record, Vols 1-5*, pp. 2022–2026, 2005.

[107] C. C. A. Kyba, J. Glodo, E. V. D. van Loef, J. S. Karp, and K. S. Shah, "Energy and timing response of six prototype scintillators for TOF-PET," *IEEE Trans. Nucl. Sci.*, vol. 55, no. 3, Part 2, pp. 1404–1408, 2008.

[108] J. Glodo, A. Kuhn, W. Higgins, E. van Loef, J. Karp, W. Moses, S. Derenzo, and K. Shah, "$CeBr_3$ for Time-of-Flight PET," in *2006 IEEE Nucl. Sci. Symp. Conf. Record*, vol. 3, pp. 1570 –1573, 2006.

[109] P. Antich, E. Tsyganov, N. Malakhov, and Z. Sadygov, "Avalanche photo diode with local negative feedback sensitive to UV, blue and green light," *Nucl. Instr. and Meth. A*, vol. 389, no. 3, pp. 491–498, 1997.

[110] G. Bondarenko, P. Buzhan, B. Dolgoshein, V. Golovin, E. Guschin, A. Ilyin, V. Kaplin, A. Karakash, R. Klanner, V. Pokachalov, E. Popova, and K. Smirnov, "Limited Geiger-mode microcell silicon photodiode: new results," *Nucl. Instr. and Meth. A*, vol. 442, no. 1-3, pp. 187–192, 2000.

[111] I. Britvitch, I. Johnson, D. Renker, A. Stoykov, and E. Lorenz, "Characterisation of Geiger-mode avalanche photodiodes for medical imaging applications," *Nucl. Instr. and Meth. A*, vol. 571, no. 1-2, pp. 308–311, 2007.

[112] V. Golovin and V. Saveliev, "Novel type of avalanche photodetector with Geiger mode operation," *Nucl. Instr. and Meth. A*, vol. 518, no. 1-2, pp. 560–564, 2004.

[113] D. J. Herbert, S. Moehrs, N. D'Ascenzo, N. Belcari, A. Del Guerra, F. Morsani, and V. Saveliev, "The Silicon Photomultiplier for application to high-resolution Positron Emission Tomography," *Nucl. Instr. and Meth. A*, vol. 573, no. 1-2, pp. 84–87, 2007.

[114] D. P. McElroy, V. Saveliev, A. Reznik, and J. A. Rowlands, "Evaluation of silicon photomultipliers: A promising new detector for MR compatible PET," *Nucl. Instr. and Meth. A*, vol. 571, no. 1-2, pp. 106–109, 2007.

[115] Y. Musienko, E. Auffray, P. Lecoq, S. Reucroft, J. Swain, and J. Trummer, "Study of multi-pixel Geiger-mode avalanche photodiodes as a read-out for PET," *Nucl. Instr. and Meth. A*, vol. 571, no. 1-2, pp. 362–365, 2007.

[116] D. Renker, "New trends on photodetectors," *Nucl. Instr. and Meth. A*, vol. 571, no. 1-2, pp. 1–6, 2007.

[117] K. Yamamoto, K. Yamamura, K. Sato, T. Ota, H. Suzuki, and S. Ohsuka, "Development of Multi-Pixel Photon Counter (MPPC)," in *2006 IEEE Nucl. Sci. Symp. Conf. Record*, vol. 2, pp. 1094 –1097, 2006.

[118] S. Espana, L. M. Fraile, J. L. Herraiz, J. M. Udias, M. Desco, and J. J. Vaquero, "Performance evaluation of SiPM photodetectors for PET imaging in the presence of magnetic fields," *Nucl. Instr. and Meth. A*, vol. 613, no. 2, pp. 308–316, 2010.

[119] A. Kolb, M. S. Judenhofer, E. Lorenz, D. Renker, and B. J. Pichler, "PET block detector readout approaches using G-APDs," in *2008 IEEE Nucl. Sci. Symp. Conf. Record*, 2008.

[120] G. Llosa, N. Belcari, M. G. Bisogni, G. Collazuol, A. Del Guerra, S. Marcatili, P. Barrillon, C. de la Taille, S. Bondil-Blin, N. Dinu, M. Melchiorri, A. Tarolli, and C. Piemonte, "Evaluation of the first Silicon Photomultiplier

matrices for a small animal PET scanner," in *2008 IEEE Nucl. Sci. Symp. Conf. Record*, pp. 3574 –3580, 2008.

[121] F. Nishikido, N. Inadama, K. Shibuya, E. Yoshida, T. Yamaya, I. Oda, K. Kitamura, and H. Murayama, "Four-layer DOI-PET detector with a silicon photomultiplier array," in *2008 IEEE Nucl. Sci. Symp. Conf. Record*, pp. 3923 –3925, 2008.

[122] R. Pestotnik, S. Korpar, H. Chagani, R. Dolenec, P. Krizan, and A. Stanovnik, "Silicon Photo-multipliers as photon detectors for PET," in *2008 IEEE Nucl. Sci. Symp. Conf. Record*, pp. 3123 –3127, 2008.

[123] D. R. Schaart, H. T. van Dam, S. Seifert, R. Vinke, P. Dendooven, H. Löhner, and F. J. Beekman, "SiPM-array based PET detectors with depth-of-interaction correction," in *2008 IEEE Nucl. Sci. Symp. Conf. Record*, pp. 3581 –3585, 2008.

[124] T. Y. Song, H. Wu, S. Komarov, S. B. Siegel, and Y.-C. Tai, "Sub-millimeter resolution pet detector module using multi-pixel photon counter array," in *2008 IEEE Nucl. Sci. Symp. Conf. Record*, pp. 4933 –4937, 2008.

[125] C. Catana, Y. Wu, M. S. Judenhofer, J. Qi, B. J. Pichler, and S. R. Cherry, "Simultaneous acquisition of multislice PET and MR images: Initial results with a MR-compatible PET scanner," *J. Nucl. Med.*, vol. 47, no. 12, pp. 1968–1976, 2006.

[126] Y. Shao, S. Cherry, K. Farahani, R. Slates, R. Silverman, K. Meadors, A. Bowery, S. Siegel, P. Marsden, and P. Garlick, "Development of a PET detector system compatible with MRI/NMR systems," *IEEE Trans. Nucl. Sci.*, vol. 44, no. 3, Part 2, pp. 1167–1171, 1997.

[127] D. W. Townsend, "Multimodality imaging of structure and function," *Phys. Med. Biol.*, vol. 53, no. 4, pp. R1–R39, 2008.

[128] R. Vinke, H. Löhner, D. R. Schaart, H. T. van Dam, S. Seifert, F. J. Beekman, and P. Dendooven, "Optimizing timing resolution for TOF PET detectors based on monolithic scintillation crystals using fast photosensor arrays," in *2008 IEEE Nucl. Sci. Symp. Conf. Record*, pp. 3954–3960, 2008.

[129] M. Gottlich, E. Garutti, V. Kozlov, H.-C. Schultz-Coulon, A. Tadday, and A. Terkulov, "Application of multi-pixel photon counter to positron emission tomography," in *2008 IEEE Nucl. Sci. Symp. Conf. Record*, pp. 3119 –3122, 2008.

[130] K. C. Burr and G.-C. Wang, "Scintillation detection using 3 mm x 3 mm silicon photomultipliers," *2007 IEEE Nucl. Sci. Symp. Conf. Record*, pp. 975–82, 2007.

[131] C. L. Kim, G.-C. Wang, and S. Dolinsky, "Multi-Pixel Photon Counters for TOF PET Detector and Its Challenges," *IEEE Trans. Nucl. Sci.*, vol. 56, no. 5, Part 1, pp. 2580–2585, 2009.

[132] D. R. Schaart, S. Seifert, H. T. van Dam, M. R. de Boer, R. Vinke, P. Dendooven, H. Löhner, and F. J. Beekman, "First experiments with $LaBr_3$:Ce crystals coupled directly to silicon photomultipliers for PET applications," in *2008 IEEE Nucl. Sci. Symp. Conf. Record*, pp. 3991 –3994, 2008.

[133] M. E. Daube-Witherspoon, S. Surti, A. Perkins, C. C. M. Kyba, R. Wiener, M. E. Werner, R. Kulp, and J. S. Karp, "The imaging performance of a $LaBr_3$-based PET scanner," *Phys. Med. Biol.*, vol. 55, no. 1, pp. 45–64, 2009.

[134] Hamamatsu Corporation MPPC (multi-pixel photocounter) S10362 series, S10931 series Cat. No. KAPD1023E03 July 2009 DN (Hamamatsu Photonics K K) http://www.hamamatsu.com.

[135] Y. Du and F. Retiere, "After-pulsing and cross-talk in multi-pixel photon counters," *Nucl. Instr. and Meth. A*, vol. 596, no. 3, pp. 396–401, 2008.

[136] Hamamatsu Corporation Photomultiplier tube R4998 TPMH1261E02 December 1999 (Hamamatsu Photonics K K) http://www.hamamatsu.com.

[137] R. I. Wiener, S. Surti, C. C. M. Kyba, F. M. Newcomer, R. Van Berg, and J. S. Karp, "An investigation of waveform sampling for improved signal processing in TOF PET," in *2008 IEEE Nucl. Sci. Symp. Conf. Record*, pp. 4101–4105, 2008.

[138] J. Glodo, W. W. Moses, W. M. Higgins, E. V. D. van Loef, P. Wong, S. E. Derenzo, M. J. Weber, and K. S. Shah, "Effects of Ce concentration on scintillation properties of $LaBr_3$:Ce," *IEEE Trans. Nucl. Sci.*, vol. 52, no. 5, pp. 1805–1808, 2005.

[139] K. Shah, J. Glodo, M. Klugerman, W. Higgins, T. Gupta, P. Wong, W. Moses, S. Derenzo, M. Weber, and P. Dorenbos, "LuI_3:Ce - A new scintillator for gamma ray spectroscopy," *IEEE Trans. Nucl. Sci.*, vol. 51, no. 5, Part 1, pp. 2302–2305, 2004.

[140] K. Shah, J. Glodo, W. Higgins, E. van Loef, W. Moses, S. Derenzo, and M. Weber, "$CeBr_3$ scintillators for gamma-ray spectroscopy," *IEEE Trans. Nucl. Sci.*, vol. 52, no. 6, Part 2, pp. 3157–3159, 2005.

[141] P. Buzhan, B. Dolgoshein, A. Ilyin, V. Kantserov, V. Kaplin, A. Karakash, A. Pleshko, E. Popova, S. Smirnov, Y. Volkov, L. Filatov, S. Klemin, and F. Kayumov, "The advanced study of silicon photomultiplier," in *Adv. Techn. Part. Phys. Proc.*, pp. 717–728, 2002.

[142] A. Stoykov, Y. Musienko, A. Kuznetsov, S. Reucroft, and J. Swain, "On the limited amplitude resolution of multipixel Geiger-mode APDs," *J. of Instr.*, vol. 2, 2007.

[143] S. Seifert, D. R. Schaart, H. T. van Dam, J. Huizenga, R. Vinke, P. Dendooven, H. Löhner, and F. J. Beekman, "A high bandwidth preamplifier for SiPM-based TOF PET scintillation detectors," in *2008 IEEE Nucl. Sci. Symp. Conf. Record*, pp. 1616 –1619, 2008.

[144] S. Seifert, H. T. van Dam, J. Huizenga, R. Vinke, P. Dendooven, H. Löhner, and D. R. Schaart, "Simulation of Silicon Photomultiplier Signals," *IEEE Trans. Nucl. Sci.*, vol. 56, no. 6, Part 2, pp. 3726–3733, 2009.

[145] R. Vinke, H. Löhner, D. Schaart, H. van Dam, S. Seifert, F. Beekman, and P. Dendooven, "Optimizing the timing resolution of SiPM sensors for use in TOF-PET detectors," *Nucl. Instr. and Meth. A*, vol. 610, no. 1, pp. 188 – 191, 2009.

[146] S. Seifert, R. Vinke, H. van Dam, H. Löhner, P. Dendooven, F. Beekman, and D. Schaart, "Ultra precise timing with SiPM-based TOF PET scintillation detectors," in *2009 IEEE Nucl. Sci. Symp. Conf. Record*, pp. 2329 –2333, 2009.

[147] A. Bousselham and C. Bohm, "Sampling pulses for optimal timing," *IEEE Trans. Nucl. Sci.*, vol. 54, no. 2, pp. 320–326, 2007.

[148] P. Antich, N. Malakhov, R. Parkey, N. Slavin, and E. Tsyganov, "3D position readout from thick scintillators," *Nucl. Instr. and Meth. A*, vol. 480, no. 2-3, pp. 782–787, 2002.

[149] D. R. Schaart, S. Seifert, R. Vinke, H. T. van Dam, P. Dendooven, H. Löhner, and F. J. Beekman, "LaBr3:Ce and SiPMs for time-of-flight PET: achieving 100 ps coincidence resolving time," *Phys. Med. Biol.*, vol. 55, no. 7, p. N179, 2010.

Summary

Introduction

Positron Emission Tomography (PET) is a major diagnostic imaging modality that is used predominantly in determining the presence and severity of cancers, neurological disorders and cardio-vascular diseases. Significant advances in PET detector performance have recently been possible due to the introduction of fast and bright inorganic scintillators for radiation detection and the development of compact, fast and high-gain solid-state photosensors for detecting the scintillation light. In a collaboration project between the Delft University of Technology (TU Delft) and the *Kernfysisch Versneller Instituut* (KVI - University of Groningen), a novel PET detector concept has been investigated that outperforms the current detector technology in commercial PET scanners with respect to several parameters.

PET basics

During a PET scan a radioactively labeled pharmaceutical is administered to a patient. This pharmaceutical consists of a radioactive isotope (radionuclide) which is chemically bound to a biologically active molecule. The substance distributes throughout the patient's body and concentrates in tissues according to their associated biochemistry. Most often the metabolism of cells is probed, indicated by the glucose consumption. During the decay of the radionuclide, a positron is released which quickly annihilates with an electron after a short traversed distance (typically < 1 mm). This produces a pair of gamma photons (γ) of 511 keV in opposite directions (see figure 1). The coincident detection of this pair of gamma photons by a cylindrical ring of radiation detectors defines a line, the line of response (LOR), along which the annihilation took place. From many recorded LORs, an image of the biodistribution of the tracer can be generated using a mathematical reconstruction algorithm. A high metabolic activity appears as a dense area in the image and can indicate the existence of cancerous tissue, while a low metabolic activity in the heart region can indicate scar tissue after a myocardial infarction (heart attack).

The ability of the physician to diagnose disease at an early stage depends crucially on the quality and accuracy of the PET image. The image quality is primarily determined by the PET detector performance.

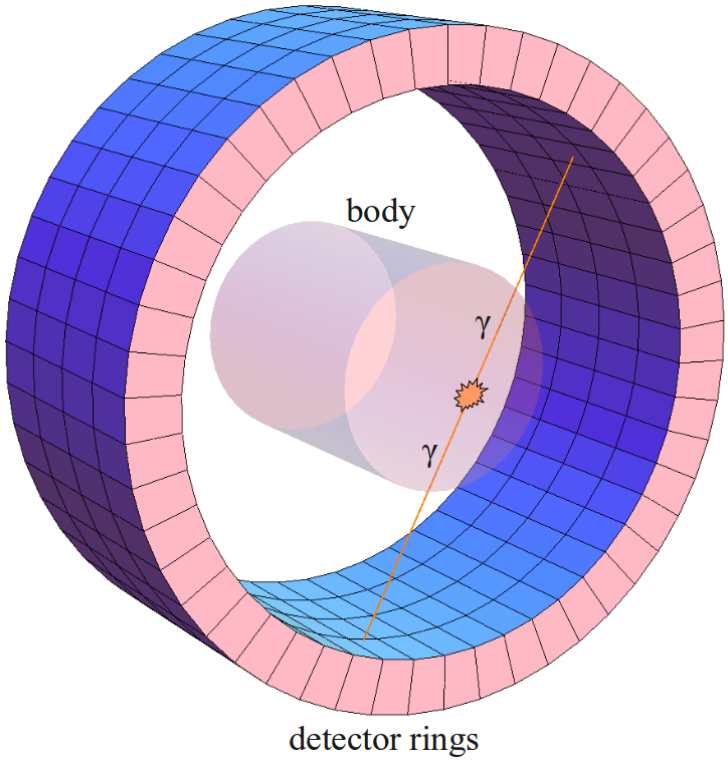

Figure 1: Schematic view of a PET scanner, consisting of radiation detectors in a cylindrical configuration. Opposite detectors can detect pairs of gamma photons from the annihilation process in coincidence.

Detector criteria

The absorbed energy, location and time of the interaction of the gamma photons in the detector have to be determined as accurately as possible.

A significant part of the produced 511 keV gamma photons scatter in the patient's body, whereby a part of the 511 keV energy is absorbed. These tissue-scattered, lower-energy gamma photons produce misplaced LORs (see figure 2), and need to be filtered out by using an energy threshold during the acquisition. To effectively do this, a detector energy resolution of better than about 10 % is needed.

To obtain high image spatial resolution, the interaction position of the gamma photon within the detector needs to be determined as accurately as possible (typically a resolution of a few millimeters is presently achieved). Preferably, the full

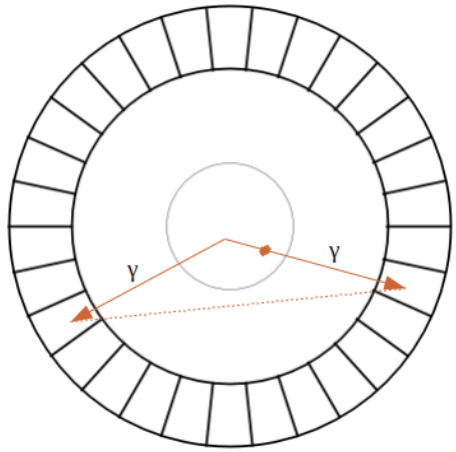

Figure 2: Misplaced line of response due to scattering of a gamma photon in the patient's body.

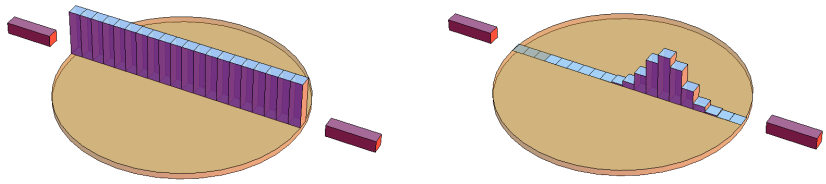

Figure 3: Conventional (left) and time-of-flight (right) reconstruction. In the conventional reconstruction there is no information about the location of the annihilation along the LOR. With time-of-flight reconstruction, the measured difference in arrival time gives a probability distribution of this location.

3D interaction position is reconstructed, thus including the depth of interaction (DOI) of the gamma photon in the detector. When including DOI information during the image reconstruction, one can correct for the so-called parallax effect, which is one of the most important resolution degrading factors in commercial PET scanners, appearing at the edge regions of the examined body [7, 8].

If the detection of a 511 keV gamma photon can be timed with an accuracy well below 1 ns, time-of-flight (TOF) information (the difference of the arrival times of two 511 keV gamma photons from the annihilation process) can be used during image reconstruction (a technique called TOF-PET, see figure 3) to significantly increase the image quality in terms of signal-to-noise ratio (SNR) [6, 12, 13]. To

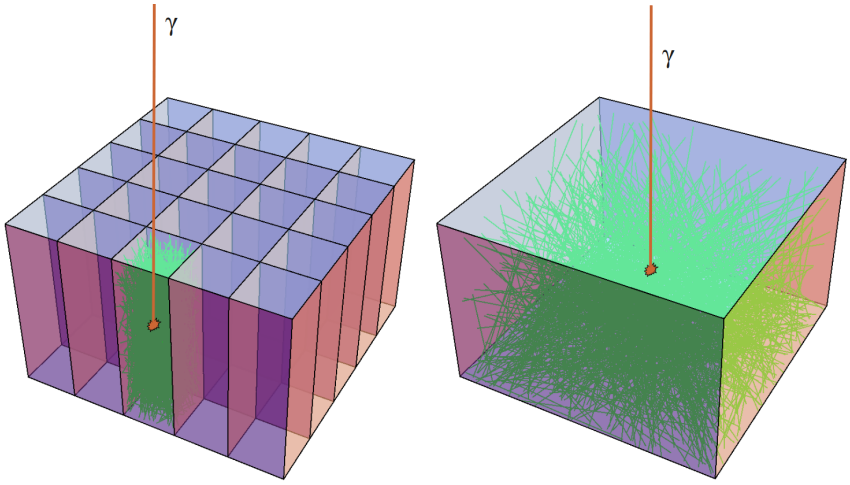

Figure 4: Left: segmented crystal. Right: monolithic crystal.

fully exploit this technique, the timing resolution of the PET detectors needs to be as good as possible. Present clinical TOF-PET scanners have a timing resolution of about 600 ps.

Detector concept with monolithic crystals

Nearly all commercial PET scanners use conventional PET detectors consisting of scintillation crystals subdivided into rectangular columns of relatively small width (few mm), the segmented crystal design, see figure 4. After gamma interaction, scintillation light is produced and read out by an array of photomultiplier tubes (PMTs). The crystal columns are covered with reflective material to channel the scintillation light with low spatial spread towards the PMTs. The position of interaction is determined by identifying in which crystal element the interaction took place.

In a monolithic scintillation detector, a large (a few cm) continuous scintillation crystal is coupled to a photosensor array. The position of interaction is determined from the scintillation light distribution over the photosensor array. Since the crystal is not subdivided into segments, dead spaces between crystal segments are avoided, maximizing the detection efficiency for gamma photons. In addition, optical losses associated with multiple reflections of the scintillation light are reduced. This increases the detector performance with respect to energy and timing resolution, since the variance in these parameters is primarily determined by the statistics of the (limited) number of scintillation photons that are produced.

Furthermore, the scintillation light distribution at the sensor array not only varies with the 2D entrance position of the gamma photon at the crystal surface, but also with the depth of the interaction (DOI). This enables the reconstruction of the full 3D interaction position of the gamma photon (see figure 5). This is not possible for the segmented crystal design, since the scintillation light is channeled towards the photosensor, and information about the DOI is essentially lost. Costly detector modifications (e.g. additional photosensors, complex optical structures) are necessary to enable DOI detection in the segmented crystal design [10], and these modifications may degrade the energy and timing resolution due to reduced light collection. Finally, the monolithic crystal design is significantly lower in cost, since no segmentation has to be applied.

In almost all current PET scanners PMTs are used as light sensors. Despite the sensitivity for extremely low light intensity and fast response, PMTs are bulky light sensors. This restricts the possibilities for flexible readout geometries. Moreover, PMTs can not be operated in a magnetic field, which prevents the development of a combined PET-MRI system for simultaneous imaging. Silicon photomultipliers (SiPMs) are recently introduced compact and fast solid state light sensors with a faster response than PMTs and with a comparable sensitivity for light. Because of their small dimension, the scintillation light can be read out from several crystal sides. Furthermore, SiPMs are insensitive to magnetic fields, such that they can be used for PET-MRI integrated systems.

Reconstruction algorithms

For the determination of the 3D interaction position of the gamma photon in the monolithic crystal, a reconstruction procedure has been developed [64] (chapter 4 in this thesis). For this procedure, the detector response was calibrated by a systematic scan with a collimated gamma beam from a radioactive source with perpendicular incidence on the front and side surface of the crystal. The calibration datasets obtained over both crystal surfaces were then combined, such that a 3D dataset of the detector response was obtained. Using a statistical algorithm, the 3D interaction position of a gamma photon in the crystal could then be calculated with this dataset. In figure 5, the average detector response has been calculated as a function of the reconstructed 3D interaction position for a $16 \times 18 \times 10$ mm^3 monolithic scintillation crystal coupled to an array of SiPM sensors [90]. It is clear that for interaction positions near the array of light sensors a peaked distribution is formed, while this distribution is more uniform for interaction positions at a larger distance. The resolution obtained for the 3D position reconstruction was 2.5 mm FWHM, which is comparable to the highest-resolution detectors presently available.

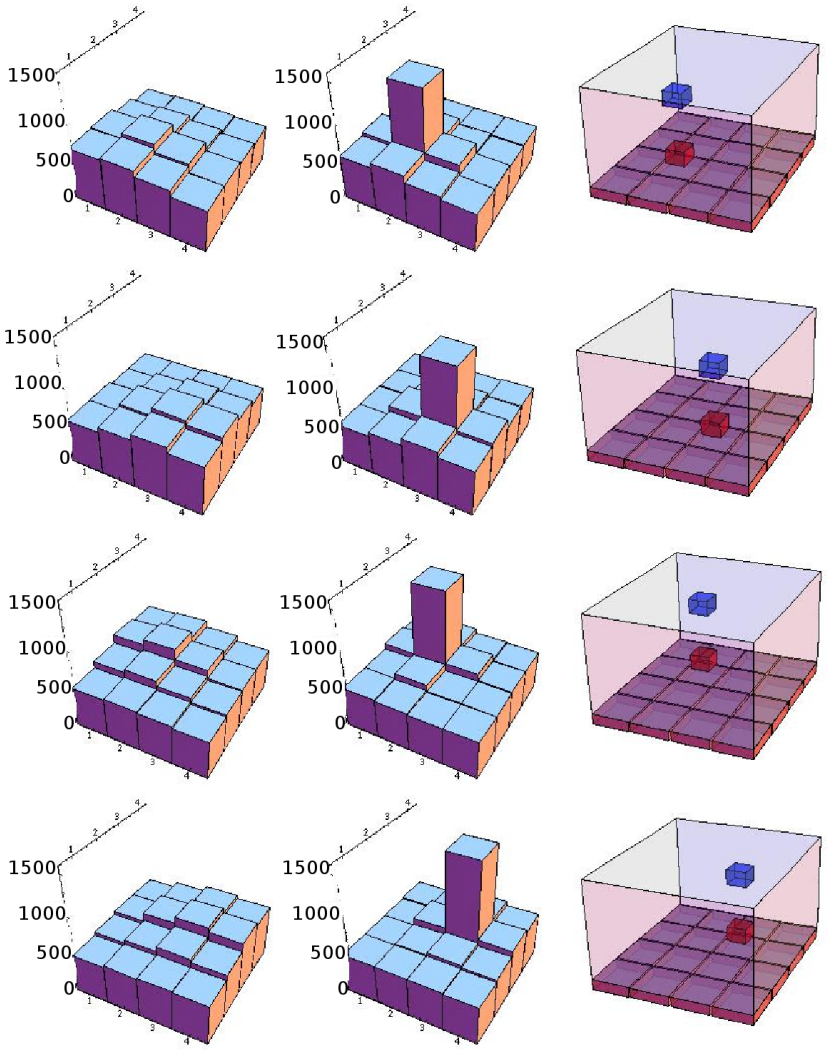

Figure 5: Average photon distribution patterns as a function of the reconstructed position, binned in 2×2×1.5 mm^3 voxels. The diagrams in the right column indicate the selected voxels. The blue voxels are at 8 mm distance from the photosensor array; the red voxels at 2 mm distance. The diagrams in the left column indicate the average photon distribution patterns corresponding to the position-of-interaction region selected by the blue voxels. The diagrams in the center column indicate the patterns corresponding to the region selected by the red voxels.

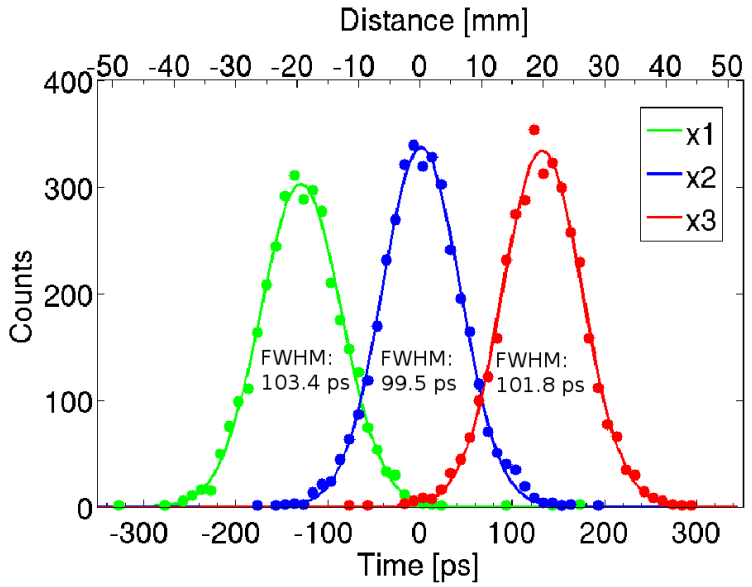

Figure 6: Timing spectra for 3 × 3 × 5 mm^3 $LaBr_3$:Ce crystals coupled to SiPM sensors. The 3 curves were obtained by placing the radioactive source at x_1 = 20 mm, x_2 = 0 mm and x_3 = -20 mm. The timing spectra shift exactly in time as can be calculated from the light speed.

The timing signals of the detectors were fully digitized, such that various algorithms could be tested to determine the arrival time as accurately as possible. For small 3 × 3 × 5 mm^3 $LaBr_3$ scintillation crystals coupled to SiPMs, a world record coincidence timing resolution of 100 ps FWHM was obtained (see figure 6) [90, 149]. For PET-relevant, large monolithic scintillation crystals the obtainable timing resolution deteriorates, among other things because of a systematic variation in time that the scintillation light needs to reach the light sensor. A procedure has been developed to correct for this systematic variation such that the timing resolution is also optimized for large crystals [64].

Conclusion

In this work, a PET detector concept was characterized based on monolithic scintillation crystals, fast photosensor arrays and statistical algorithms that determine the location of the scintillation emission in the crystal. The excellent timing resolution provides a very high signal-to-noise ratio in the PET images (the time-of-flight

PET method). Furthermore, the position reconstruction algorithm enables that the edge regions of the examined body can be imaged well (depth-of-interaction reconstruction). This detector concept has the potential to significantly improve PET's ability to visualize, quantify, and characterize disease. This could lead to an earlier cancer diagnosis, which is essential for a more effective cancer therapy.

Samenvatting

Inleiding

Positron Emissie Tomografie (PET) is een zeer belangrijke medische beeldvormende techniek die voornamelijk gebruikt wordt voor het bepalen van de aanwezigheid en hevigheid van kankergezwellen, neurologische aandoeningen en hart- en vaatziekten. Grote verbeteringen van de PET-detectorprestaties zijn recent mogelijk geworden door de introductie van snelle en fel oplichtende scintillatiekristallen voor stralingsdetectie en de ontwikkeling van compacte en snelle halfgeleider lichtsensoren voor het uitlezen van het scintillatielicht. In een samenwerkingsproject tussen de TU Delft en het Kernfysisch Versneller Instituut (KVI) in Groningen is een PET detectorconcept onderzocht dat de huidige detectortechnologie qua prestatie op verschillende vlakken overtreft.

PET principe

Bij een PET scan wordt een radioactief gemarkeerd farmacon toegediend aan een patiënt. Dit farmacon bestaat uit een radioactief isotoop (radionuclide) dat chemisch verbonden is aan een biologisch actief molecuul. Het farmacon verspreidt zich over het lichaam van de patiënt en hoopt zich op in weefsels met een specifieke biologische functie. De functie die meestal door PET in beeld wordt gebracht is de metabolische activiteit (glucoseverbruik) van de cellen. Hiervoor wordt radioactief gelabeld glucose (fluorodesoxyglucose, FDG) gebruikt. Tijdens het radioactief verval van de radionuclide wordt een positron uitgezonden dat na een korte afgelegde afstand (typisch < 1 mm) annihileert met een elektron. Hierbij worden twee gamma-fotonen (γ) van 511 keV in tegenovergestelde richtingen uitgezonden (zie figuur 1). De gelijktijdige detectie van beide gamma-fotonen door een ring van stralingsdetectoren definieert een lijn, de *line of response* (LOR), waarlangs de annihilatie plaats heeft gevonden. Vanuit een grote verzameling van deze LOR's kan een afbeelding van de distributie van het farmacon in het lichaam worden gegenereerd met een wiskundig reconstructiealgoritme. Een lichaamsregio met een hoge metabolische activiteit correspondeert met een fel gekleurde regio in de afbeelding en kan duiden op de aanwezigheid van een kankergezwel. Een lage metabolische activiteit in de hartregio kan duiden op littekenweefsel na bijvoorbeeld een hartaanval.

Het vermogen van een arts om een ziekte in een vroeg stadium vast te stellen

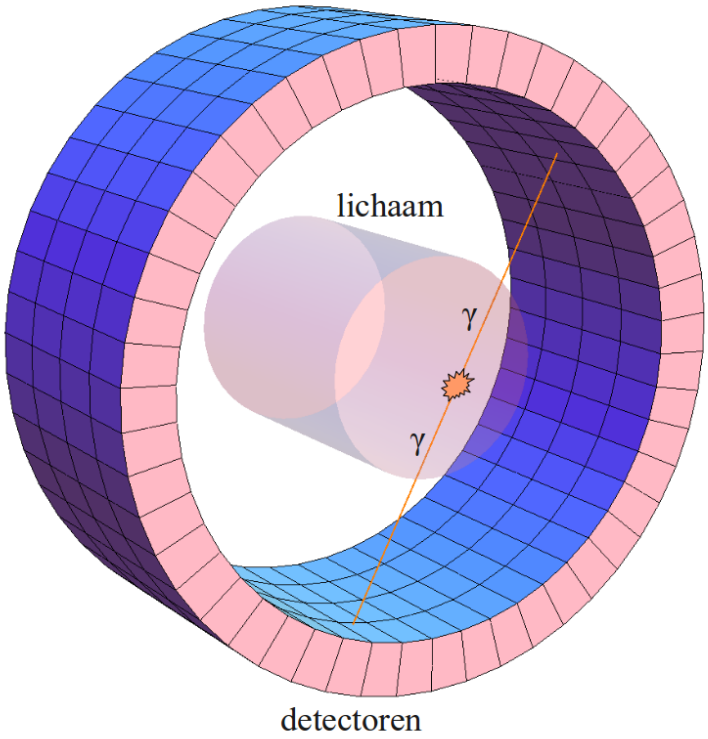

Figuur 1: Schematische weergave van een PET scanner, bestaande uit stralingsdetectoren in een cylindrische configuratie. Tegenover liggende detectoren kunnen paren van gamma-fotonen afkomstig uit het annihilatie-proces gelijktijdig detecteren.

hangt af van de kwaliteit en nauwkeurigheid van de PET afbeelding. Deze factoren worden primair bepaald door de prestatie van de PET detectoren.

Detector criteria

De geabsorbeerde energie, plaats en tijd van de interactie van de gamma-fotonen in de detector dienen zo nauwkeurig mogelijk bepaald te worden.

Een aanzienlijk deel van de geproduceerde 511 keV gamma-fotonen verstrooien in het lichaam van de patiënt, waarbij een gedeelte van de 511 keV energie wordt geabsorbeerd. Deze verstrooide gamma-fotonen van lagere energie produceren verkeerd geplaatste LOR's (zie figuur 2), en dienen te worden uitgefilterd door het hanteren van een energiedrempel tijdens de acquisitie. Om dit effectief uit te

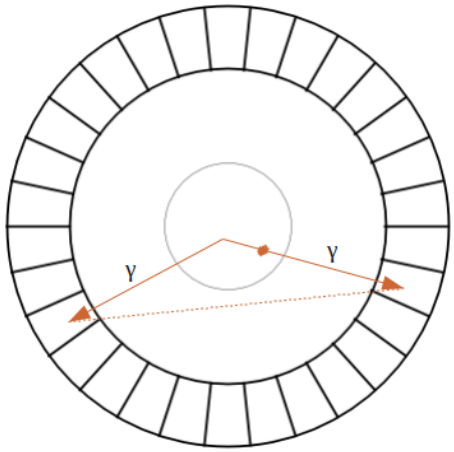

Figuur 2: Verkeerd geplaatste line-of-response door verstrooiing van een gamma-foton in het lichaam van de patiënt.

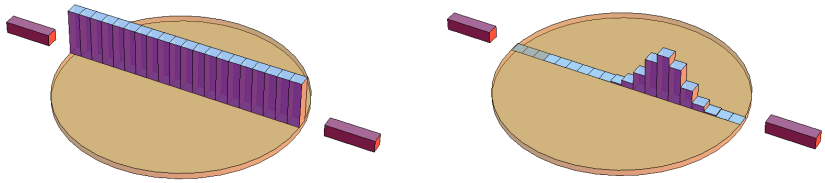

Figuur 3: Conventionele (links) en time-of-flight (rechts) reconstructie. In de conventionele reconstructie is er geen informatie over de plaats van annihilatie langs de LOR. Met time-of-flight reconstructie geeft het gemeten verschil in aankomsttijd een waarschijnlijkheidsverdeling van deze plaats.

voeren is een detectorenergieresolutie van beter dan 10% nodig.

Voor het verkrijgen van een hoge beeldresolutie moet de interactiepositie van het gamma-foton in de detector zo precies mogelijk worden bepaald (een plaatsresolutie van een paar mm wordt tegenwoordig typisch behaald). Bij voorkeur wordt de volledige 3D positie gereconstrueerd, inclusief de interactiediepte van het gamma-foton in de detector (*depth of interaction*, DOI). Wanneer de DOI-informatie tijdens de beeldreconstructie wordt gebruikt, kan er worden gecorrigeerd voor het parallax-effect, één van de belangrijkste degradatiefactoren in commerciële PET scanners die optreedt aan de randzones van het onderzochte lichaam [7, 8].

Als het interactietijdstip van het gamma-foton in de detector kan worden

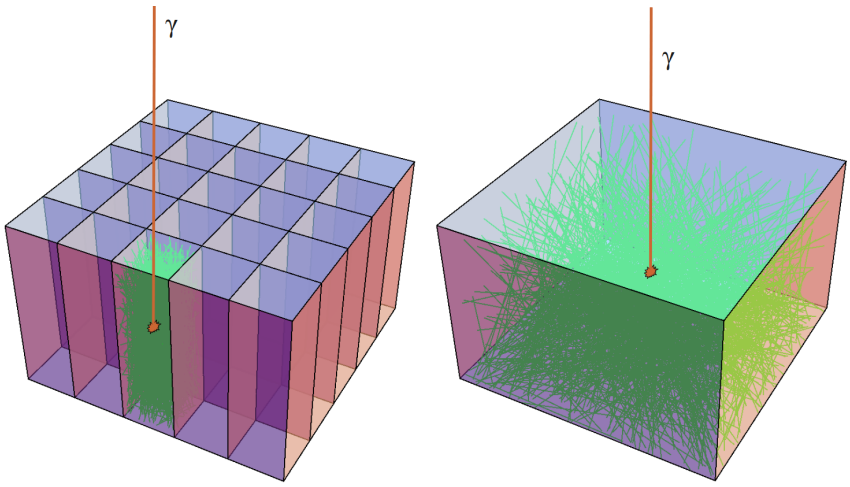

Figuur 4: Links: gesegmenteerd kristal. Rechts: monolithisch kristal.

bepaald met een nauwkeurigheid beter dan 1 ns, kan *time-of-flight* (TOF) informatie (het verschil in aankomsttijd tussen de twee 511 keV gamma-fotonen uit het annihilatie-proces) tijdens de beeldreconstructie worden gebruikt (zie figuur 3). Het is aangetoond dat deze TOF-PET techniek de signaal-ruisverhouding van het gereconstrueerde beeld aanzienlijk verbetert [6, 12, 13]. De tijdsresolutie van de detectoren dient zo goed mogelijk te zijn om optimaal gebruik te maken van deze techniek. Commerciële TOF-PET scanners halen tegenwoordig een tijdsresolutie van ongeveer 600 ps.

Detectorconcept met monolithische kristallen

Bijna alle commerciële PET scanners gebruiken conventionele PET detectoren, bestaande uit scintillatiekristallen onderverdeeld in rechthoekige kolommen van relatief kleine breedte (enkele mm): het gesegmenteerde kristal, zie figuur 4. Na interactie van het gamma-foton wordt het scintillatielicht uitgelezen door een reeks photomultiplier tubes (PMT's). De kristal kolommen zijn bedekt met reflectief materiaal zodat het scintillatielicht met een kleine verspreiding wordt geleid naar de PMT's. De interactiepositie wordt bepaald door het identificeren van het kristalsegment waar de interactie plaats vond.

In een monolithische scintillatiedetector is een groot (enkele cm) continu scintillatiekristal gekoppeld aan een reeks van lichtsensoren. De interactiepositie wordt bepaald aan de hand van de verdeling van het scintillatielicht over de lichtsensoren. Aangezien het kristal niet onderverdeeld is in segmenten, is er geen dode ruimte

binnen het kristal, zodat de efficiëntie voor het detecteren van de gamma-fotonen maximaal is. Verder is het optisch verlies door reflecties van het scintillatielicht binnen het kristal verminderd. Dit verbetert de nauwkeurigheid waarmee de energie en aankomsttijd kan worden vastgesteld, aangezien de variantie in deze parameters primair wordt bepaald door de statistiek van het (beperkt) aantal geproduceerde scintillatiefotonen. Verder varieert de verdeling van het scintillatielicht over de lichtsensoren niet alleen met de 2D positie op het kristaloppervlak waar het gamma-foton binnentrad, maar ook met de interactiediepte (DOI) van het gamma-foton binnen het kristal. Dit betekent dat de volledige 3D interactiepositie kan worden gereconstrueerd (zie figuur 5). Dit is niet mogelijk voor het gesegmenteerde kristal, aangezien het scintillatielicht met een minimale verspreiding wordt geleid naar de lichtsensor, zodat de DOI-informatie verloren gaat. Dure detector-modificaties (bijvoorbeeld extra lichtsensoren, complexe optische structuren) zijn benodigd om DOI-detectie mogelijk te maken in het gesegmenteerde kristal, en deze modificaties kunnen de energie- en tijdsresolutie verslechteren door een verminderde lichtcollectie. Het monolithische kristal is verder aanzienlijk goedkoper te produceren, aangezien er geen segmentatie hoeft te worden toegepast.

In bijna alle huidige PET scanners worden PMT's als lichtsensoren gebruikt. Ondanks de gevoeligheid voor extreem lage lichtintensiteit en snelle respons, zijn PMT's omvangrijke lichtsensoren. Dit beperkt de mogelijkheden van flexibele uitleesgeometrieën. Bovendien kunnen PMT's niet in een magnetisch veld gebruikt worden, hetgeen de ontwikkeling van een gecombineerd PET-MRI systeem voor gelijktijdige beeldvorming verhindert. Silicon photomultipliers (SiPM's) zijn recent uitgevonden compacte en snelle halfgeleider lichtsensoren met een snellere respons dan PMT's en met een vergelijkbare lichtgevoeligheid. Door hun kleine formaat kan het scintillatielicht vanuit meerdere kristalzijdes worden uitgelezen. SiPM's zijn verder ongevoelig voor magnetische velden, zodat deze lichtsensoren gebruikt kunnen worden voor PET-MRI geïntegreerde systemen.

Reconstructiealgoritmes

Voor het bepalen van de 3D interactiepositie van het gamma-foton in het monolithisch kristal is een reconstructieprocedure ontwikkeld [64] (hoofstuk 4 in dit proefschrift). Voor deze procedure werd de respons van de detector gecalibreerd door een systematische scan met een gecollimeerde bundel gamma-fotonen uit een radioactieve bron met loodrechte inval op het voor- en zijvlak van het kristal. De verkregen calibratiedatasets over beide kristalvlakken werden vervolgens gecombineerd zodat een 3D dataset van de detectorrespons werd verkregen. Met een statistisch algoritme kon vervolgens aan de hand van deze dataset de 3D interactiepositie van een gamma-foton in het kristal worden berekend. In figuur 5

is de gemiddelde detectorrespons berekend als functie van de gereconstrueerde 3D interactiepositie voor een $16 \times 18 \times 10$ mm^3 monolithisch scintillatiekristal gekoppeld aan een reeks SiPM sensoren [90]. Het is duidelijk dat voor interactieposities nabij de reeks lichtsensoren er een gepiekte distributie wordt gevormd, terwijl deze distributie meer uniform is voor interactieposities op een grotere afstand. De resolutie waarmee de 3D positie kon worden gereconstrueerd bedroeg 2.5 mm FWHM, hetgeen vergelijkbaar is met de hoogste resolutie detectoren die tegenwoordig beschikbaar zijn.

De tijdssignalen van de detectoren werden volledig gedigitaliseerd, zodat verscheidene algoritmes konden worden uitgetest om het aankomsttijdstip zo nauwkeurig mogelijk te bepalen. Voor kleine $3 \times 3 \times 5$ mm^3 $LaBr_3$:Ce kristallen gekoppeld aan SiPM sensoren werd een wereldrecord tijdsresolutie voor 511 keV fotonen van 100 ps FWHM behaald (zie figuur 6) [90, 149]. Voor PET-relevante, grote monolithische scintillatiekristallen verslechtert de behaalbare tijdsresolutie, onder andere door een systematische variatie in de tijd die het scintillatielicht nodig heeft om de lichtsensor te bereiken. Er is een procedure ontwikkeld om voor deze systematische variatie te corrigeren zodat de tijdsresolutie ook voor grote kristallen geoptimaliseerd blijft [64].

Conclusie

In dit werk is een PET detectorconcept onderzocht dat gebruik maakt van grote, monolithische scintillatiekristallen, snelle lichtsensoren en statistische algoritmes die de plaats van de scintillatie-emissie in het kristal bepalen. De uitstekende tijds-resolutie zorgt voor een zeer hoge signaal-ruisverhouding in de PET plaatjes (de time-of-flight PET methode). Verder laat het ontwikkelde plaatsbepalingsalgoritme toe dat ook de randzones van het onderzochte lichaam goed afgebeeld kunnen worden (depth-of-interaction reconstructie). Dit detectorconcept belooft een significante verbetering in het vermogen van PET om ziekte te visualiseren, kwantificeren en karakteriseren. Dit zou kunnen leiden tot een vroegere kankerdiagnose, hetgeen essentieel is voor een effectievere kankertherapie.

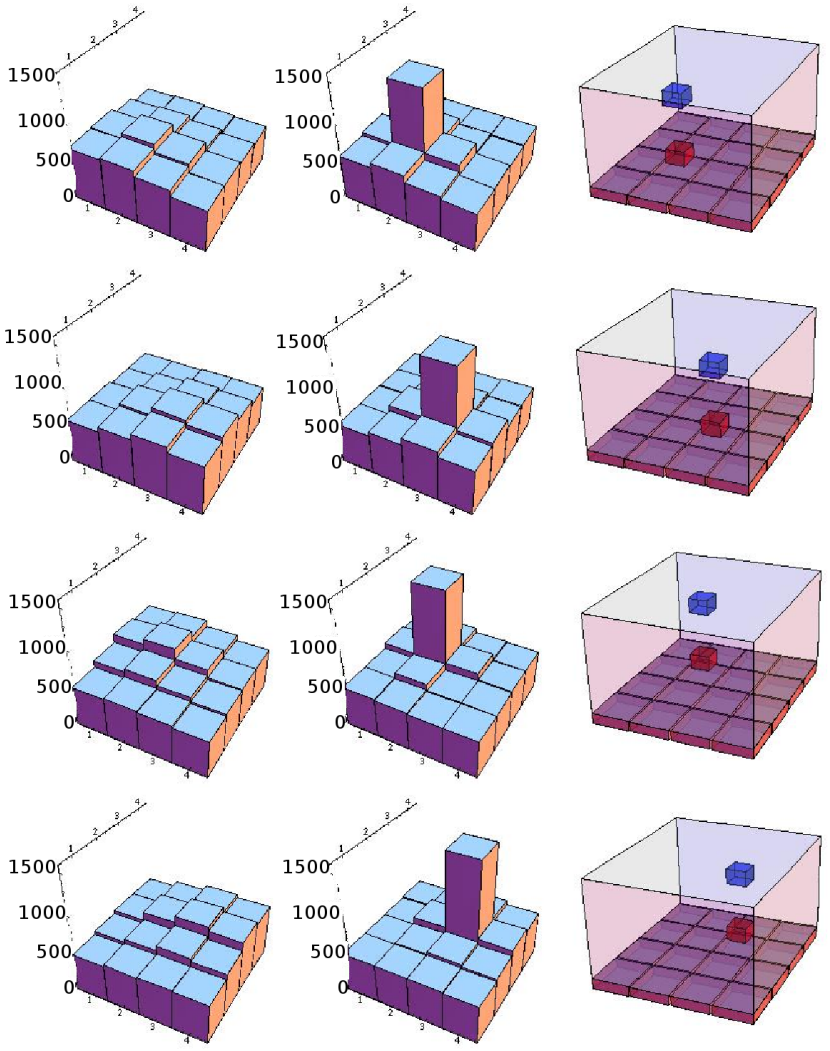

Figuur 5: Gemiddelde detectorrespons als functie van de gereconstrueerde 3D interactiepositie van het gamma-foton in het kristal, ingedeeld in 2 × 2 × 1.5 mm^3 voxels. De diagrammen in de rechter kolom geven de geselecteerde voxels aan. De blauwe voxels bevinden zich op 8 mm afstand van lichtsensoren, de rode voxels op 2 mm afstand. De diagrammen in de linker kolom geven de gemiddelde detectorrespons aan, corresponderende met interactieregio's aangegeven door de blauwe voxels. De diagrammen in de middelste kolom geven de respons aan, corresponderende met de regio's aangegeven door de rode voxels.

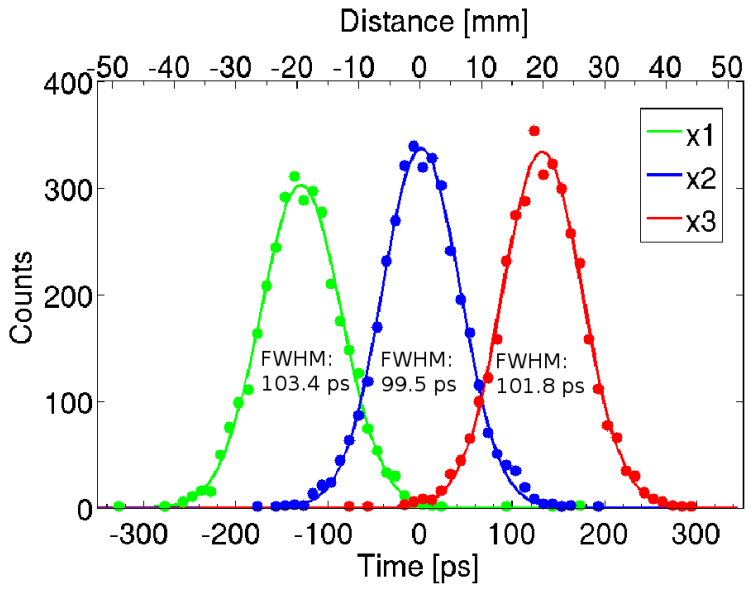

Figuur 6: Tijdsspectra voor 3 × 3 × 5 mm^3 $LaBr_3$:Ce kristallen gekoppeld aan SiPM sensoren. De 3 curves werden verkregen door de radioactieve bron te plaatsen op x_1 = 20 mm, x_2 = 0 mm en x_3 = -20 mm. De tijdsspectra verschuiven exact in tijd zoals met de lichtsnelheid kan worden berekend.

List of Publications

R. Vinke, H.T. van Dam, S. Seifert, F.J. Beekman, H. Löhner, D.R. Schaart, and P. Dendooven, "Thick monolithic scintillation crystals for TOF-PET with depth-of-interaction measurement," *in preparation.*

R. Vinke, H. Löhner, D.R. Schaart, H.T. van Dam, S. Seifert, F.J. Beekman, and P. Dendooven, "Time walk correction for TOF-PET detectors based on a monolithic scintillation crystal coupled to a photosensor array," *Nucl. Instr. Meth. A*, vol. 621, pp. 595-604, 2010.

R. Vinke, H. Löhner, D.R. Schaart, H.T. van Dam, S. Seifert, F.J. Beekman, and P. Dendooven, "Optimizing the timing resolution of SiPM sensors for use in TOF-PET detectors," *Nucl. Instr. and Meth. A*, vol. 610, pp. 188-191, 2009.

D.R. Schaart, S. Seifert, R. Vinke, H.T. van Dam, P. Dendooven, H. Löhner, and F.J. Beekman, "$LaBr_3$:Ce and SiPMs for time-of-flight PET: achieving 100 ps coincidence resolving time," *Phys. Med. Biol.*, vol. 55, pp. N179-N189, 2010.

H.T. van Dam, S. Seifert, R. Vinke, P. Dendooven, H. Löhner, F.J. Beekman, and D.R. Schaart, "A Comprehensive Model of the Response of Silicon Photomultipliers," *IEEE Trans. Nucl. Sci.*, vol. 57, pp. 2254-2266, 2010.

S. Seifert, H.T. van Dam, J. Huizenga, R. Vinke, P. Dendooven, H. Löhner, and D.R. Schaart, "Simulation of Silicon Photomultiplier Signals," *IEEE Trans. Nucl. Sci.*, vol. 56, pp. 3726-3733, 2009.

D.R. Schaart, H.T. van Dam, S. Seifert, R. Vinke, P. Dendooven, H. Löhner, and F.J. Beekman, "A novel, SiPM-array-based, monolithic scintillator detector for PET," *Phys. Med. Biol.*, vol. 54, pp. 3501-3512, 2009.

R. Vinke, H.T. van Dam, S. Seifert, F.J. Beekman, H. Löhner, D.R. Schaart, and P. Dendooven, "Thick monolithic scintillation crystals for TOF-PET with depth-of-interaction measurement," *2010 IEEE Nucl. Sci. Symp. Conf. Record*, NM3-3, 2010.

R. Vinke, S. Seifert, D.R. Schaart, F.P. Schreuder, M.R. de Boer, H.T. van Dam, F.J. Beekman, H. Löhner, and P. Dendooven, "Optimization of Digital Time Pickoff Methods for $LaBr_3$-SiPM TOF PET Detectors," *2009 IEEE Nucl. Sci. Symp. Conf. Record*, pp. 2962-2968, 2009.

R. Vinke, H. Löhner, D.R. Schaart, H.T. van Dam, S. Seifert, F.J. Beekman, and P. Dendooven, "Optimizing timing resolution for TOF-PET detectors based on monolithic scintillation crystals using fast photosensor arrays," *2008 IEEE Nucl. Sci. Symp. Conf. Record*, pp. 3954-3960, 2008.

S. Seifert, R. Vinke, H.T. van Dam, H. Löhner, P. Dendooven, F.J. Beekman, and D.R. Schaart, "Ultra Precise Timing with SiPM-Based TOF PET Scintillation Detectors," *2009 IEEE Nucl. Sci. Symp. Conf. Record*, pp. 2329-2333, 2009.

H.T. van Dam, S. Seifert, R. Vinke, H. Löhner, P. Dendooven, F.J. Beekman, and D.R. Schaart, "Silicon Photomultiplier Response Model," *2009 IEEE Nucl. Sci. Symp. Conf. Record*, pp. 2362-2364, 2009.

D.R. Schaart, S. Seifert, H.T. van Dam, M.R. de Boer, R. Vinke, P. Dendooven, H. Löhner, and F.J. Beekman, "First experiments with $LaBr_3$:Ce crystals coupled directly to silicon photomultipliers for PET applications," *2008 IEEE Nucl. Sci. Symp. Conf. Record*, pp. 3991-3994, 2008.

S. Seifert, D.R. Schaart, H.T. van Dam, J. Huizenga, R. Vinke, P. Dendooven, H. Löhner, and F.J. Beekman, "A high bandwidth preamplifier for SiPM-based TOF PET scintillation detectors," *2008 IEEE Nucl. Sci. Symp. Conf. Record*, pp. 1616-1619, 2008.

D.R. Schaart, H.T. van Dam, S. Seifert, R. Vinke, P. Dendooven, H. Löhner, and F.J. Beekman, "SiPM-array based PET detectors with depth-of-interaction correction," *2008 IEEE Nucl. Sci. Symp. Conf. Record*, pp. 3581-3585, 2008.

Dankwoord

Graag wil ik de vele mensen bedanken die mij direct of indirect geholpen hebben gedurende de tijd van mijn promotieonderzoek.

Ik ben zeer bevoorrecht geweest om de excellente begeleiding van Peter Dendooven te genieten. Ik heb uitermate veel geleerd van zijn uitgebreide kennis op het gebied van kernfysica en stralingsdetectie. Peter, hartelijk dank voor de betrokkenheid en alle hulp tijdens het opzetten van de experimentele setup, interpretatie van resultaten, schrijven van artikelen en het mij wegwijs maken in de wereld van de wetenschap. Ook wil ik graag Herbert Löhner bedanken voor het algemene toezicht op mijn promotieonderzoek en het regelen van alle organisatorische aspecten. Ik waardeer ook alle feedback op de artikelen en het proefschrift, waarbij dankzij jou zelfs de kleinste stijlfouten niet onopgemerkt bleven.

Dennis Schaart, bedankt voor de vele interessante discussies, feedback op de artikelen, het organisatorische werk zodat ik gedurende 2 maanden in Delft heb kunnen bijdragen aan de metingen van hoofdstukken 7 en 8, en de algemene leiding over het SciSiLiA-project. Freek Beekman, bedankt voor de feedback op de artikelen. Ik heb het ook aan jou te danken dat ik aan een tijdelijke woonruimte in Delft kon komen.

I would like to thank Prof. dr. C.W.E. van Eijk, Prof. dr. W. Enghardt and Prof. dr. A.M.J. Paans for their willingness to act as members of my thesis reading committee, as well as for their valuable suggestions and comments.

It has been a great pleasure to work with Stefan Seifert, with whom I have collaborated on the work in chapter 7. We had many interesting discussions during the interpretation of the results. I also greatly appreciate all his work on the experimental setup for the measurements with the monolithic scintillation detector in chapter 8 and all the feedback during the preparation of articles. Herman van Dam, graag wil ik jou ook bedanken voor alle interessante discussies en feedback op de artikelen.

Grote dank gaat uit naar Frans Schreuder voor het design en de bouw van de snelle voorversterkers voor de SiPM's. De 16-kanaals voorversterker die was gebruikt voor de SiPM-array in hoofdstuk 8 kwam van zijn hand, en was essentieel voor het behalen van de goede tijdsmetingen. Dank gaat verder uit naar Hans Vorenholt, die aan het begin van het project de voorversterker heeft gebouwd die is gebruikt in hoofdstuk 6. Ook hebben Jan Huizenga en Stefan Seifert van de TU Delft zeer veel werk verricht bij het design en de bouw van de snelle voorversterkers voor de SiPM's, die onder andere leidden tot het resultaat van hoofdstuk 7. Ik wil Martijn de Boer hartelijk danken voor al zijn betrokkenheid en waardevolle werk

gedurende de voorbereiding en tijdens de metingen in hoofdstuk 8 en verder Marc Korevaar voor de interessante discussies over het bepalen van de aankomsttijd van de scintillatiepulsen met statistische algoritmes.

Hilde van der Meer, Miranda Ruiter en Annet van der Woude, bedankt voor al het administratieve werk.

At KVI, I met many great people who made my stay in Groningen enjoyable, also off duty. Thanks for the unforgettable time: Ali, Ayan, Jordy, Kalpana, Leila, Manisha, Ola, Olena, Olga, Renato, Simona, Sivaji, Sybren, Victor. Special thanks to Qader. I am pleased that you accepted to be my paranymph. Hồng, thanks for being my close friend and your help on many occasions.

I am also grateful to my other colleagues for the great time at KVI: Bodha, Corine, Daniel, Daren, David, Duurt, Elmaddin, Erwin, Frans, Ganesh, Gerco, Gianluca, Gouri, Hans, Harm, Harry, Hilde, Hossein, Ina, Imko, Jacco, Jacob, Joanne, Johan M., Johan S., Jos, Krijn, Lotje, Marc-Jan, Mariët, Marjan, Marlene, Martine, Miranda, Mohammad, Myroslav, Nasser, Oksana, Oliver, Olmo, Oscar, Peter S., Rob, Ronald, Sadia, Soumya, Suresh, Sytze, Vanni, Wilbert. Robert en Alfred, het was me een genoegen met jullie meerdere malen langs het kanaal te rennen.

Verder ben ik mijn dankbaarheid verschuldigd aan mijn kameraden, in het bijzonder Bart, Daan, Djoek, Evert, Henk, Jan-Willem, Marcel, Michiel en Simon. Ik heb dankzij jullie door de jaren heen een geweldige tijd in Groningen beleefd. Ik wens jullie allen het beste toe en hoop jullie nog vaak te spreken en bezoeken.

Tenslotte, mijn familie, bedankt voor jullie onvoorwaardelijke steun.